ABSTRACT

PHILLIPS, MATTHEW RYAN. Predicting and Controlling the Manufacturing and Thermomechanical Microstructural Behavior of Ribbed Carbon-Nanotube-PDMS Systems for Multifunctional Applications (Under the direction of Professor Mohammed A. Zikry.)

The proposed research has been focused on fundamentally understanding and controlling the generation of microstructural surface features, such as ribbed morphologies and instabilities, of carbon-nanotube-polydimethylsiloxane (CNT-PDMS) thin-films, such that the systems can be adapted for extreme environments, such as high pressures, high strain-rates, and large strains. These micro-structured surfaces can be controlled to provide desired behavior, such as superhydrophobia, drag reduction, and anti-biofouling; ribbed CNT-PDMS thin-films are one such material system that can be adapted for multifunctional applications.

The manufacturing of thin-films with structured surfaces by large-scale rolling has distinct advantages over other techniques, such as lithography, including scalability and shortened operating times. It is not yet well understood, however, how the processing conditions and material behavior of CNT-PDMS systems can affect the microstructure at different physical scales. It is also not known how the material properties or ribbing structures affect the thermomechanical behavior in response to dynamic compressive strain-rates, such that damage-resistant thin-films can be attained for heterogeneous morphologies and large-strains. Hence, the objectives of this investigation are to develop predictive models informed by experimental observations and measurements of both the manufacturing process and the dynamic response to high strain-rate loading, as well as to characterize the large-strain behavior and evolving morphology of CNT-PDMS systems.

Therefore, computational models of the symmetric forward-roll coating process were developed to understand, predict, and control the ribbing morphology of CNT-PDMS thin-films. The effects of the rheological properties and the roller gap on the ribbing behavior were investigated and a ribbing instability model was formulated by integrating experimental measurements and computational predictions. The nonlinear implicit dynamic finite-element (FE) model accounted for ribbing instabilities, large displacements, rolling contact and large pressures, and material viscoelasticity. The viscoelastic properties were obtained by dynamic mechanical analysis for different CNT-PDMS compositions. Furthermore, a Morris sensitivity analysis was conducted to understand and identify the dominant characteristics pertaining to the ribbing microstructure. Based on the sensitivity analysis, a critical ribbing aspect ratio was identified for the CNT-PDMS system corresponding to a critical roller gap.

The nonlinear explicit dynamic three-dimensional FE formulation was also used to understand and predict the thermomechanical response of the ribbed thin-films subjected to dynamic in-plane compressive loading. Representative volume element (RVE) FE models of the ribbed thin-films were subjected to strain-rates as high as 10^4 s^{-1}. Latin hypercube sampling of the microstructural parameters, as informed from experimental observations and measurements, were used to obtain microstructurally-based RVEs. An interior-point optimization routine was also employed on a regression model trained from the FE predictions that can be used to design ribbed materials for multifunctional applications. The model predicts that damage can be mitigated in CNT-PDMS systems subjected to dynamic compressive loading conditions by controlling the ribbing microstructural characteristics, such as the film thickness and the ribbing amplitude and wavelength.

PDMS and CNT-PDMS tensile testing specimens were also fabricated to understand the effects of the CNT-PDMS composition on the large-strain mechanical behavior. The global stress-strain behavior of each composition was obtained, and scanning electron microscopy (SEM) characterization of fracture surfaces were obtained to analyze the microstructure and damage modes. Based on these experimental measurements and observations, large-strain hyperelastic and hyper-viscoelastic material models were used to characterize the material behavior. The hyper-viscoelastic material model was shown to provide an accurate material description of the thin-film behavior of the viscoelastic PDMS with high-strength CNTs.

This research integrated fundamental computational and experimental approaches in a framework for designing materials that can be utilized for myriad applications tailored for multifunctional high strain-rate damage tolerance, hydrophobicity, and anti-biofouling.

© Copyright 2024 by Matthew Ryan Phillips

All Rights Reserved

Predicting and Controlling the Manufacturing and Thermomechanical Microstructural Behavior of Ribbed Carbon-Nanotube-PDMS Systems for Multifunctional Applications

by
Matthew Ryan Phillips

A dissertation submitted to the Graduate Faculty of
North Carolina State University
in partial fulfillment of the
requirements for the degree of
Doctor of Philosophy

Aerospace Engineering

Raleigh, North Carolina

2024

APPROVED BY:

Professor Mohammed A. Zikry
Committee Chair

Professor Kara Peters

Professor Jong Ryu

Professor Arvind Saibaba

DEDICATION

To my mother, father, and sister.

BIOGRAPHY

Matthew Ryan Phillips was born in Thornton, Colorado in 1996. He remained near his hometown until graduating from Mountain Range High School in May 2015. Matthew obtained bachelor's degrees in mechanical engineering and in applied and computational mathematics at South Dakota School of Mines and Technology (SDSM&T) in Rapid City, South Dakota. During his undergraduate career, Matthew pursued several research opportunities. He worked at the Composite and Polymer Engineering Laboratory on campus for two years, which introduced him to carbon- and glass-fiber composite materials manufacturing, testing, and development. Matthew continued his undergraduate research career by participating in a Research Experience for Undergraduates at North Carolina State University (NCSU) under the mentorship of Dr. Mohammed Zikry. He then worked with magnetic shape memory alloys at the Laboratory of Engineered Multifunctional Materials and Alloys at SDSM&T as an undergraduate research assistant and later researched aeroacoustics of wind turbines at the National Renewable Energy Laboratory as a Science Undergraduate Laboratory Internship participant.

In August 2020, Matthew continued into graduate studies at NCSU under the mentorship of Dr. Mohammed Zikry. His research focused on modeling the manufacturing and dynamic behavior of carbon-nanotube-polymer thin-film systems. He has also worked as a graduate research and development intern at Sandia National Laboratories where he modeled the mechanical behavior of a photovoltaic module in response to pressure loadings. In addition to completing his M.S. and Ph.D. in aerospace engineering, he has also completed the requirements for a Ph.D. minor in applied mathematics.

The research publications and conference presentations related to this dissertation are listed below.

M. Phillips, P. Zaghari, J. Ryu, M. Zikry (2024) Dynamic Behavior of Ribbed Viscoelastic CNT-PDMS Thin-Films for Multifunctional Applications. *International Mechanical Engineering Congress and Exposition*. *American Society of Mechanical Engineers*, Portland, OR

M. Phillips, P. Zaghari, J. Ryu, M. Zikry (2024) Microstructural behavior of CNT-PDMS thin-films for multifunctional systems, *Composites Part A: Applied Science and Manufacturing*. 187. 108473. https://doi.org/10.1016/j.compositesa.2024.108473.

M. Phillips, M.J. Chen, J. Ryu, M. Zikry (2024) Dynamic Behavior of Ribbed Viscoelastic CNT-PDMS Thin-Films for Multifunctional Applications, *Macromolecular Materials and Engineering*. 2400098. https://doi.org/10.1002/mame.202400098.

M. Phillips, M.J. Chen, J. Ryu, M. Zikry (2023) Dynamic Behavior of Ribbed Viscoelastic PDMS Thin-Films for Multifunctional Applications. *International Mechanical Engineering Congress and Exposition*. *American Society of Mechanical Engineers*, New Orleans, LA

M. Phillips, M.J. Chen, M.D. Islam, J. Ryu, M. Zikry (2023) Predicting and Controlling Ribbing Instabilities of Carbon Nanotube–PDMS Thin-Film Systems for Multifunctional Applications, *Advanced Engineering Materials*. 25. 2300582. https://doi.org/10.1002/adem.202300582.

M.D Islam, H. Perera, S. Chockalingam, **M. Phillips**, M.J. Chen, Y. Liu, S. Khan, Y. Zhu, M. Zikry, J. Ryu (2022) Template-free scalable fabrication of linearly periodic microstructures by controlling ribbing defects phenomenon during forward roll coating, *Manufacturing Letters*. 33. 153–160. https://doi.org/10.1016/j.mfglet.2022.08.001.

M.D. Islam, H. Perera, B. Black, **M. Phillips**, M. Chen, G. Hodges, A. Jackman, Y. Liu, C. Kim, M. Zikry, S. Khan, Y. Zhu, M. Pankow, J. Ryu (2022) Template-Free Scalable Fabrication of Linearly Periodic Microstructures by Controlling Ribbing Defects Phenomenon in Forward Roll Coating for Multifunctional Applications, *Advanced Materials Interfaces*. 9. 2201237. https://doi.org/10.1002/admi.202201237.

M. Phillips, M.J. Chen, M.D. Islam, J. Ryu, M. Zikry (2022) Predicting and Controlling Instabilities of CNT/PDMS Systems for Multifunctional Applications. *International Mechanical Engineering Congress and Exposition*. *American Society of Mechanical Engineers*, Columbus, OH

ACKNOWLEDGMENTS

I would first like to acknowledge my parents, Jerry and Stacie, for their unconditional love and support. You have instilled in me the confidence to follow my dreams, the integrity to do what is right, and the spunk to persevere during uncertain times. Most important, you have inspired me to share with others the warmth and kindness that you have shared with me. Jadyn and Payton, thank you for your encouragement and love. I would also like to acknowledge the Bottum and Trevillyan families for your true and constant friendship. In particular, I would like to thank Joseph Bottum for the many conversations over dinner in South Dakota, for the continued mentorship in graduate school, and for the constant push to add a second string to my bow. Siena, Chance, Derek, C.J., Mike, Wyatt, Nick, Connor, Miguel, Patty, Larry, and Susan, thank you for having made Raleigh feel like home. I cannot thank you all enough for your friendship and generosity.

My advisor and committee chair, Dr. Mohammed Zikry, deserves a special acknowledgement for his many years offering me guidance and support. I would also like to thank my doctoral committee members, Dr. Jong Ryu, Dr. Kara Peters, and Dr. Arvind Saibaba, for providing valuable feedback on my research. My coworkers deserve much thanks for offering community and advice during my time at NCSU, particularly Dr. Mohamed Elbadry and Dr. Ismail Mohamed for mentoring me as an undergraduate student and Dr. Tamir Hasan, Dr. Muh-Jang Chen, and Omar Eldaly for guiding and encouraging me throughout my time in graduate school. Lastly, I would like to extend my sincere gratitude to the U.S. National Science Foundation (Grant 2031558) and the Office of Naval Research (Grant N00014-23-1-2758) for funding this research and my doctoral studies.

I could not have done this without you all.

TABLE OF CONTENTS

LIST OF FIGURES ix

LIST OF TABLES xvi

CHAPTER 1: Introduction 1

1.1 Motivation 1

1.2 Research Objectives 7

1.3 Dissertation Outline 8

CHAPTER 2: Constitutive Formulations and Numerical Methods 9

2.1 Introduction 9

2.2 Thermo-Viscoelasticity and Hyper-Viscoelasticity 9

- 2.2.1 Frequency-domain viscoelasticity 10
- 2.2.2 Time-domain viscoelasticity 11
- 2.2.3 Time-temperature superposition for thermo-rheologically simple materials 11
- 2.2.4 Hyper-viscoelastic material behavior 12

2.3 Finite-Element Element Types and Formulations 14

- 2.3.1 Three-dimensional displacement brick elements 15
- 2.3.2 Three-dimensional thermal-displacement coupled brick elements 15
- 2.3.3 Finite-element implicit time integration 16
- 2.3.4 Finite-element explicit time integration 17

CHAPTER 3: Finite-Element Modeling of 3-D Ribbing Instabilities Manufactured by Twin-Roll Coating Process 19

3.1 Introduction 19

3.2 Viscoelastic Characterization of Uncured PDMS and CNT-PDMS 20

3.3 Characterization of Ribbed Thin-Film Morphology 30

3.4 Finite-Element Model Set-up of Large-Scale Rolling 35

3.5 Large-Scale Rolling Finite-Element Results 37

- 3.5.1 The effects of local stresses on ribbing 38
- 3.5.2 The effects of the roller gap on the ribbing behavior 43

3.6 Ribbing Instability Model Formulation 45

- 3.6.1 Instability of ribbing microstructures 45
- 3.6.2 Method of Morris sensitivity analysis of the ribbing instability 49

3.7 Conclusions 50

CHAPTER 4: Thermomechanical Response of Ribbed Thin-Film Systems to High Strain-Rate Dynamics 53
4.1 Introduction 53
4.2 Thermo-Viscoelastic Characterization of Cured PDMS and CNT-PDMS 53
4.3 Ribbing Microstructure of Representative Volume Element Finite-Element Models 57
4.4 Dynamic Thin-Film Representative Volume Element Models 60
4.5 Finite-Element Modeling Results 63
  4.5.1 The dynamic thermomechanical behavior of ribbed thin-film systems 64
  4.5.2 The Von Mises stress hypersurface visualization for ribbed thin-films 70
4.6 Ribbing Microstructure Optimization and Uncertainty Quantification 72
4.7 Conclusions 77
CHAPTER 5: Large-Strain Behavior of PDMS and CNT-PDMS 79
5.1 Introduction 79
5.2 Large-Strain Uniaxial Mechanical Testing of PDMS and CNT-PDMS 80
  5.2.1 Uniaxial testing procedure for thin polymer-composite samples 80
  5.2.2 Uniaxial testing results for thin PDMS and CNT-PDMS samples 81
5.3 Scanning Electron Microscopy Imaging of PDMS and CNT-PDMS Morphology 84
  5.3.1 Scanning electron microscopy procedure for non-conductive materials 84
  5.3.2 Scanning electron microscopy results for PDMS and CNT-PDMS samples 85
5.4 Characterization of PDMS and CNT-PDMS as Viscoelastic and Hyper-viscoelastic Materials 93
5.5 Conclusions 99
CHAPTER 6: Conclusions and Recommendations 101
REFERENCES 105

LIST OF FIGURES

Figure 3.1. Shear storage (G') and loss ($G"$) moduli recorded as a function of the angular frequency by dynamic mechanical analysis for CNT-PDMS paste with varying CNT weight percent (wt%) content. ..………………………………………………. 21

Figure 3.2. Prony series material model of shear storage and loss moduli for (a) 0 wt% CNT (neat PDMS), (b) 1 wt% CNT, and (c) 3.5 wt% CNT obtained by delayed rejection adaptive metropolis (DRAM) Bayesian routine and by constrained optimization (Con. Opt. Fit) according to Equation (3.1) compared to data obtained by dynamic mechanical analysis. ..…………………………………………… 23

Figure 3.3. Delayed rejection adaptive metropolis (DRAM) Results for (a) uncured PDMS and (b) CNT-PDMS with 3.5 wt% CNT. ……………………………………… 25

Figure 3.4. Time response of the shear modulus for CNT-PDMS paste with 3.5 wt% CNT governed by Equation (2.4) with Prony series time constants (τ_1 = 10^{-2}, τ_1 = 10^{-1}, τ_1 = 10^{0}, τ_1 = 10^{1}), relaxation coefficients (Table 3.3), instantaneous shear modulus (G_0) (Table 3.3), and long-term shear modulus (G_∞) obtained by Equation (2.3). This material model is used to predict the behavior of ribbed CNT-PDMS during large-scale rolling. …………………………..………………… 30

Figure 3.5. (a) The rolling of the CNT-PDMS paste with 3.5 wt% CNT content for rotational speed (ω) and roller gap (h), (b) the cured CNT-PDMS ribbed material adhered to the polyimide sleeve. ……….…………………...………………………... 32

Figure 3.6. Scanning electron microscopy images of CNT-PDMS ribbed microstructure produced by varying the roller gap (h) for (a) specimen A, h = 250 μm, (b) specimen B, h = 300 μm, (c) specimen C, h = 350 μm, (d) specimen D, h = 400 μm, and (e) specimen E, h = 450 μm. ………………………………………………. 33

Figure 3.7. (a) Three-dimensional finite-element model of the two-roll coating process producing ribbed CNT-PDMS material with film, rollers, roller gap (h), rotational speed (ω), friction (μ), and wavelength (λ) identified, (b) cross-section of film in the gap showing five ribbing periods with ribbing amplitude (A) and film thickness (H). …………………………………………………………..……. 36

Figure 3.8. (a) Von Mises stress (σ_{VM}) normalized by the instantaneous elongation modulus (E_0) of finite-element mesh corresponding to specimen A showing stress evolution of ribbed film passing through roller gap and the retention of the ribbing profile downstream of the gap, (b) cross-section of the thin-film between rollers with roller surfaces removed to view the film surface. …...…………………………… 40

Figure 3.9. Von Mises stress (σ_{VM}) normalized by the instantaneous elongation modulus (E_0) of non-ribbed finite-element mesh with similar conditions to specimen A. The stress distribution is uniform through the film width (z-direction) after excluding edge effects. Inset image shows normalized stress distribution in cross-section between the rollers. …………………………………………………………..………. 41

Figure 3.10. Normalized three-dimensional stress components of the ribbed film finite-element mesh corresponding to specimen A. …….……………………………………... 42

Figure 3.11. Von Mises stress (σ_{VM}) normalized by the instantaneous elongation modulus (E_0) of finite-element models corresponding to (a) mesh A, (b) mesh B, (c) mesh C, (d) mesh D, and (e) mesh E within yz cross-section highlighted in (f). ..…. 44

Figure 3.12. (a) Ribbing aspect ratio, a_r, with respect to the prescribed non-dimensional roller gap, R/h, obtained from experiments, (b) average normalized normal stress components, $\bar{\sigma}_{ii}/E_0$, and Von Mises stress, $\bar{\sigma}_{VM}/E_0$, predicted by finite-element models with respect to the non-dimensional roller gap……………………………….. 46

Figure 3.13. Average normalized Von Mises stress ($\bar{\sigma}_{VM}/E_0$) in gap cross-section from finite-element models with respect to ribbing aspect ratio (a_r) and maximum limiting value $(\bar{\sigma}_{VM}/E_0)_{lim}$. ……………………………………………………… 47

Figure 4.1. The viscoelastic material behavior of the normalized time-dependent shear modulus for cured, neat PDMS and CNT-PDMS based on [84] according to the Universal Polymer Model [87] and recharacterized for use in the 3-D finite element models (FEM). The instantaneous shear modulus, G_0, and long-term shear modulus, G_∞, were obtained from [84] for neat PDMS and were obtained by rule of mixtures for CNT-PDMS with 3.5 wt% CNT. The relaxation behavior is described by the 20-term Prony series listed in Table 4.1. ……………………………… 55

Figure 4.2. The Williams-Landel-Ferry time-temperature superposition behavior of PDMS and CNT-PDMS according to Equation (2.5) and based on coefficients from [84]. ………………………………………………………………………….. 57

Figure 4.3. The microstructural parameters of the 16 representative volume element thin-film models were populated by Latin Hypercube Sampling including the eight corners within the bounds enforced by Table 4.2. Each circle shows the ribbing amplitude, ribbing wavelength, and film thickness of each representative volume element model in the parameter space. ………………………………………………… 60

Figure 4.4. A representative volume element thin-film model subjected to a dynamic compressive load (a) parallel to the ribbing direction and (b) transverse to the ribbing direction. Each thin-film model has a prescribed ribbing amplitude (A), ribbing wavelength (λ), and film thickness (H) specified from the 16 microstructural combinations resulting from the Latin Hypercube Sampling routine. The bottom surface was simply supported, a dynamic compressive load was applied to one in-plane face, and symmetry boundary conditions were applied to the remaining in-plane faces. ……………………………………………………... 62

Figure 4.5. The average z-displacement of the line path within the thin-film model with ribbing amplitude of 0.046 mm, ribbing wavelength of 0.444 mm, and film thickness of 0.479 mm subjected to parallel loading (in the z-direction) with a nominal applied strain rate of (a) 10^2 s^{-1}, (b) 10^3 s^{-1}, and (c) 10^4 s^{-1}. …………………... 64

Figure 4.6. The average normal stress in the (a) x-direction, (b) y-direction, and (c) z-direction, and the average shear stress in the (d) xy-direction, (e) yz-direction, and (f) xz-direction, all normalized by the instantaneous elongation modulus of the cured, neat PDMS, E_0, were obtained through the center path of the representative volume element model with a ribbing amplitude of 0.046 mm, ribbing wavelength of 0.444 mm, and film thickness of 0.479 mm subjected to three strain rates in the parallel ribbing direction (the z-direction). …………………………………………….. 66

Figure 4.7. The average Von Mises stress normalized by the instantaneous elongation modulus of the material, E_0, obtained from the line path within the thin-film model with ribbing amplitude of 0.046 mm, ribbing wavelength of 0.444 mm, and film thickness of 0.479 mm subjected to parallel loading. The solid and dashed lines show the behavior of neat PDMS and CNT-PDMS, respectively. The time was normalized by the total time of each model for easier visual comparison. ……….. 67

Figure 4.8. The average temperature of the line path within the thin-film model with ribbing amplitude of 0.046 mm, ribbing wavelength of 0.444 mm, and film thickness of 0.479 mm subjected to parallel loading with a nominal applied strain rate of (a) 10^2 s^{-1}, (b) 10^3 s^{-1}, and (c) 10^4 s^{-1}. …………………………………………… 69

Figure 4.9. The maximum Von Mises stress normalized by the instantaneous elongation modulus, E_0, for (a) neat PDMS and (b) CNT-PDMS obtained from each of the 16 representative volume element thin-film models subjected to a nominal strain rate of 10^3 s^{-1}. The hypersurfaces were constructed by linearly interpolating between the 16 data points obtained from FE. …………………………………………………... 71

Figure 4.10. The maximum Von Mises stress normalized by the instantaneous elongation modulus of the material, E_0, for (a) neat PDMS and (b) CNT-PDMS obtained from of each of the 16 representative volume element thin-film models for all three strain rates. The hypersurfaces were constructed for each nominal applied strain rate by the regression model obtained in Equation (4.1). ……………………….. 74

Figure 4.11. The regression model was optimized to obtain the microstructure yielding the lowest maximum stress (minimax stress) for (a) neat PDMS and (b) CNT-PDMS.

The solid black curve gives the minimax stress of all microstructural combinations for nominal strain rates between 10^0 s^{-1} and 10^4 s^{-1}. The dashed red and blue curves give the minimax stress for a non-ribbed film ($\alpha_r = 0$) and a maximally ribbed film ($\alpha_r = 0.30$), respectively. 76

Figure 5.1. Instron 68SC-05 single column table universal testing machine with CNT-PDMS sample loaded in the clamps (a) before testing and (b) after failure. ...………… 81

Figure 5.2. Non-ribbed PDMS tensile test specimens with CNT loadings, from left to right, of 0 wt%, 1 wt%, 3.5 wt%, and 10 wt% fabricated according to ASTM D638-22 specifications and subjected to uniaxial tension to failure. ………………….. 82

Figure 5.3. Ultimate engineering strain and ultimate engineering strength with respect to CNT weight percent in PDMS obtained from the average of five samples with error bars indicating two standard deviations. ………………………………………… 83

Figure 5.4. Scanning electron microscopy (SEM) micrograph of fracture surface at low magnification for neat PDMS obtained using electron beam of 100 V. The texture of the sample is featureless apart from a surface contaminant shown to demonstrate that the material is focused in the SEM. ………………………………….. 86

Figure 5.5. Scanning electron microscopy micrograph of fracture surface at low magnification for (a) 1 wt% and (b) 3.5 wt% CNT and at higher magnification for (c) 1 wt% and (d) 3.5 wt% CNT obtained using electron beam of 100 V. The texture of the two samples is rough but suggests a brittle-like fracture of the heterogenous material. The lighter regions in (c) and (d) indicate areas of high CNT concentration. ……………………………………………………………….. 87

Figure 5.6. Scanning electron microscopy (SEM) backscatter micrograph of fracture surface for 10 wt% CNT at high magnification obtained using electron beam of 100 V showing CNT pullout. ………………………………………………………... 89

Figure 5.7. Scanning electron microscopy (SEM) micrograph of fracture surface at high magnification for (a) 1 wt%, (b) 3.5 wt% and (c) 10 wt% CNT and at ultra-high magnification for (d) 1 wt%, (e) 3.5 wt% and (f) 10 wt% CNT obtained using electron beam of 100 V. …………………………………………………………... 91

Figure 5.8. Yeoh hyperelastic material model for four material compositions of CNT-PDMS optimized from five uniaxial tension experiments of each composition. ……… 97

Figure 5.9. Yeoh-Prony hyper-viscoelastic material model for four material compositions of CNT-PDMS optimized from five uniaxial tension experiments of each composition. ………………………………………………………...……………….. 98

LIST OF TABLES

Table 3.1. Prony series parameter values for PDMS viscoelastic material model governed by Equations (2.1) and (2.2) determined using constrained optimization (Con. Opt.) and delayed rejection adaptive metropolis (DRAM) schemes. …………………………. 26

Table 3.2. Prony series parameter values for CNT-PDMS with 1 weight percent CNT viscoelastic material model governed by Equations (2.1) and (2.2) determined using constrained optimization (Con. Opt.) and delayed rejection adaptive metropolis (DRAM) schemes. ………………………………………………………………… 27

Table 3.3. Prony series parameter values for CNT-PDMS with 3.5 weight percent CNT viscoelastic material model governed by Equations (2.1) and (2.2) determined using constrained optimization (Con. Opt.) and delayed rejection adaptive metropolis (DRAM) schemes. ………………………………………………………………… 27

Table 3.4. Prony series parameter values for CNT-PDMS with 10 weight percent CNT viscoelastic material model governed by Equations (2.1) and (2.2) determined using constrained optimization (Con. Opt.) and delayed rejection adaptive metropolis (DRAM) schemes. ………………………………………………………………… 28

Table 3.5. Standard deviation of Prony series parameters for 3.5 wt% CNT material model governed by Equations (2.1) and (2.2) found by constrained optimization (Con. Opt.) and delayed rejection adaptive metropolis (DRAM) schemes. ……………………. 29

Table 3.6. Experimental microstructural measurements of post-rolled CNT-PDMS specimens after curing, ribbing wavelength measurements approximated for use in finite-element models. ………………………………………………………………….. 34

Table 4.1. The 20-term Prony series characterization for cured, neat PDMS with time constants, τ_i, and relaxation coefficients, g_i, based on [84] for the Universal Polymer Model (UPM) and recharacterized for use in 3-D finite element models (FEM). ……………………………………………………………………………….. 54

Table 4.2. The bounds of the three ribbing microstructural parameters, the ribbing amplitude (A), ribbing wavelength (λ), and film thickness (H) were obtained from scanning electron microscopy measurements for non-ribbed films (ribbing aspect ratio α_r = 0) and ribbed films with a maximum ribbing aspect ratio of 0.30. Thin-films with microstructures within these bounds represent the range of possible non-ribbed and ribbed thin-film CNT-PDMS systems. ……………………………………… 59

Table 4.3. The coefficients from the regression model obtained by linear least squares to predict the maximum normalized Von Mises stress in ribbed thin-film systems with a given ribbing microstructure and nominal compressive strain-rate. …………………... 73

Table 5.1. Hyperelastic Yeoh material model coefficients of four compositions of CNT-PDMS obtained by constrained optimization routine with root-mean-square-error. …… 94

Table 5.2. Hyper-viscoelastic Yeoh-Prony material model coefficients of four compositions of CNT-PDMS obtained by constrained optimization routine with root-mean-square-error. …………………………………………………………………… 95

CHAPTER 1: Introduction

1.1 Motivation

Bio-inspired thin-film systems can be tailored for multifunctional applications, and the structured topology of the thin-film plays a significant role in surface behavior, such as superhydrophobicity [1–7], anti-icing [2,7], anti-fouling [8,9], self-cleaning [10], optical [8,9], and electrical [8,9,11–14]. Carbon-nanotube-polydimethylsiloxane (CNT-PDMS) thin-film materials manufactured with a ribbed microstructure are one such structured bio-inspired system. The multi-phase, heterogeneous system with a hierarchal shark-skin-like topology exhibits favorable surface behaviors, such as superhydrophobicity, drag reduction, and anti-biofouling [4,6,15–20]. Moreover, these ribbed systems can be manufactured in a cost-effective, high-output manner, by continuous large-scale rolling.

Ribbing structures are periodic surfaces that develop in thin liquid and solid films during large-scale rolling processes. These finger-like periodic structures develop in the meniscus between two separating surfaces when the Capillary number, $Ca = \mu U/\gamma$, exceeds a critical value where μ is the viscosity, U is the characteristic speed, and γ is the surface energy of the material [4,6,21,21–26]. Historically, these structured surfaces have been viewed as defects in the material because large-scale rolling is most often used for producing smooth sheets at industry-level scales. Different experimental and computational approaches have been undertaken to understand the formation and evolution of ribbing in thin-films that occur in large-scale forward-roll coating processes to reduce surface defects, while maintaining desired processing objectives, such as the film thickness and operating time [21,23,27]. Analytical approaches for understanding how ribbing instabilities originate in fluids were developed by [21,27], based on lubrication theory. Computational approaches, such as finite-volume and finite-element (FE) methods, based on the

Navier-Stokes equations have also been used to understand the hydrodynamic nature of ribbing [23,26,28,29]. The ribbing defects were controlled by determining the processing conditions, such as the roller size and speed, and by disrupting the formation of new ribbing instabilities in the meniscus [30].

A framework was developed by [26] to understand the formation, evolution, and spatial persistence of ribbing instabilities in fluid thin-films resulting from the symmetric forward-roll coating process. Four regions were defined: the meniscus, the flow-field transition, the leveling-film, and the leveled-film regions. The meniscus region between the rollers generates the ribbed surface resulting from a large pressure gradient normal to the free surface, which is consistent with experimental [24] and numerical [22,25,28,31] analyses. The pressure gradient decreases in the flow-field transition region away from the meniscus, and surface tension is the dominant driving force; the material flows from the crests of the ribbing instabilities back to the troughs in the leveling-film region. Far away from the meniscus where the pressure gradient is negligible, the film is a smooth and rib-free surface if the surface tension is sufficient. It is desirable to minimize the generation of ribbing defects [30] or to use the framework introduced by [26] to accelerate the decay of ribs that have already been formed for applications that require a smooth fluid or solid thin-film surface.

Although most approaches have viewed material ribbing as defects, and the general approach has been to minimize their generation [21–26,28–32], some applications benefit from structured surfaces that result in such behavior as drag reduction, anti-biofouling, self-cleaning, superhydrophobicity, and anti-icing [4–7,10,33]. For these applications, it is essential not only to control the ribbing microstructure, but also to inhibit the surface tension-driven leveling of the ribbing instabilities by selecting appropriate materials and manufacturing conditions. These goals can be achieved by large-scale rolling.

Structured thin-film system manufactured by large-scale rolling has the potential for continuous manufacturing and cost-effective mass production. Different manufacturing approaches to obtain these surface behaviors have been undertaken, such as plasma [1] or abrading [2] treatments of thin polymer or ceramic sheets, photolithography [12] or roller embossing [3,5], and inducing wrinkling topologies [8,11,13,14,34]. Some of these surface treatments, however, do not produce consistent surfaces, and others require expensive or complex processing and manufacturing approaches. Lithography-free techniques, such as large-scale rolling or wrinkling, do not require time-consuming processing or complex manufacturing approaches to create surface features with high aspect ratios [4,6,8,17]. Wrinkled surfaces, for example, are typically produced by compressing and permanently deforming the thin-film to the desired hierarchal surface structure. These lithography-free techniques can also allow for the control of the wavelength, the amplitude, and the orientation of desired topologies or patterns, and these surface characteristics can be directly linked to material properties and manufacturing conditions [8,11,13,14,34,35].

CNT-PDMS composites are a viable candidate material to achieve controlled and persistent ribbing microstructures and to design damage-resistant thin-films. The viscoelasticity of the uncured PDMS increases the Capillary number, which is directly related to the generation of ribbing structures during large-scale rolling. The CNT inclusions provide strength to retain the periodic structure, such that it can be cured, and the high aspect ratio of the CNTs increases the achievable surface texture necessary for superhydrophobicity and drag reduction surface behaviors.

CNTs have been used as inclusions in polymer films for multifunctional applications, such as highly sensitive strain gauges [36–38], biosensors [38], and energy harvesters [38,39], because of their exceptional strength, electrical conductivity, and thermal conductivity with minimal additional weight [4,6,40–42]. Additional benefits to adding CNT or other carbon-based and nano-sized inclusions in a polymer matrix include increased stiffness and strength [43–47], increased thermal and electrical conductivity [45,47–49], improved thermal stability [50], and flame retardant capabilities [49], which can make these composite systems ideal for flexoelectric, piezoelectric, and other multifunctional applications.

The addition of CNTs to a polymer matrix allows the shear moduli of the uncured material to stabilize in the low-frequency regime and the elastic modulus of the cured composite to increase compared to the neat polymer [4,39,49,51]. Some fillers, such as nanoclays, in contrast, do not sufficiently solidify the material in the low-frequency regime so the ribbed microstructure will not persist once the rollers stop due to surface tension-driven leveling [40]. If this leveling is mitigated by a filler material, then the thermoset material can be cured at an elevated temperature to lock the microstructure and increase the material strength. The composite material has been shown by [38] to have high compressive strengths between 0.7 and 2 MPa for a CNT weight percentage that ranges from 1 to 10 that enable these composites to withstand the extreme pressure from extrusion-based 3-D printing, which is similar to the extreme pressure environment encountered during twin rolling.

Furthermore, an advantage of such high aspect ratio fillers as CNTs is that the properties of the composite film and the ribbing wavelength can be tailored by the alignment of the fillers within the matrix. Ribbing is significantly affected when such viscoelastic polymers as PDMS or such elastic fillers as CNTs are rolled. The aspect ratio of the CNTs allows for small ribbing wavelengths, which provide surface behavior most suitable for such applications as drag reduction, superhydrophobicity, and anti-icing, which depend on the texture of the thin-film [6,7,10,25,31,32,52,53]. Additionally, high viscosity pastes made of high aspect ratio fillers and a polymer matrix retain the ribbing surface defects after the rolling has stopped and the film is cured [4,6,39]. This has also been observed in 3-D printing, where the low surface tension prevents the printed structure from collapsing before curing [38].

The dispersion of CNTs is a fundamental issue, since CNTs tend to bundle or aggregate, which can act as a stress concentration rather than as a strengthening mechanism, thus sufficient mixing is required for improved mechanical strength. Common manufacturing techniques used to disperse CNTs in a matrix include sonication, stirring, and solution mixing [37,38,54]. These techniques generally retain the integrity and size of CNTs but at the expense of relatively slow processing times and little to no control over the CNT alignment. Large-scale rolling in conjunction with a shear mixing stage has the potential to ensure adequate mixing, dispersion, and alignment of CNTs throughout the polymer matrix while maintaining structural integrity. It also provides the possibility of continuous processing.

When cured, PDMS, as with most polymers, exhibits a degree of time- or rate-dependent viscoelastic relaxation that results from the reversible stretching of polymer chains and is capable of achieving large strains [42,55–62]. The addition of CNTs increases the strength of the material by preventing the movement of polymer chain entanglements. Most material characterization and modeling of PDMS and CNT-PDMS has been limited to small-strain viscoelastic behavior using dynamic mechanical analysis or creep tests and Prony series viscoelastic material models [4,15,17,39,60,63,64]. The Prony series representation can be converted between time-dependent and frequency-dependent forms, such that the material model can be obtained from either creep tests (time domain) or dynamic mechanical analysis (frequency domain), and it can then be used to predict the behavior in the other domain [57,65].

When subjected to large strains, additional deformation modes of the polymer chains occur that can result in hyperelastic behavior [63,64,66–71]. Many hyperelastic material models exist in the literature, each of which is tailored for different materials or strain regimes. A recent review [66] found that the Ogden, Yeoh, Carroll, and Shariff hyperelastic material models have a coefficient of determination (R^2) greater than 0.98 when calibrated with uniaxial tension experimental stress-strain curves of elastomers; other commonly used models had lower R^2 values with 0.65 for Neo-Hookean and 0.59 for Mooney Rivlin. Both hyperelastic and viscoelastic contributions can be used to define the material behavior in a single hyper-viscoelastic material model [59,63,64,69–74] to represent the large-strain behavior and the time-dependent relaxation of the polymer.

Each mechanism depends on the CNT weight content, the degree of CNT dispersion throughout the matrix or agglomeration into CNT bundles, and the orientation of the CNTs and CNT bundles in relation to the loading direction. Additionally, thin samples must be characterized to obtain accurate tensile strengths and moduli for thin films [75,76]. Thus, it is necessary to understand how best to represent and understand the global large-strain mechanical behavior of the material while accounting for the rate- or time-dependent effects and the interaction of CNTs in PDMS for various CNT weight fractions.

There is little or no understanding how the structured material responds to extreme conditions that may be encountered while in-use, such as high strain-rate loading conditions. Experimental investigations have been conducted on thin polymer [69,77,78] and metal [45,79–81] films to understand how high strain-rate behavior affects thin-films for such applications as

MEMS devices, among others. Thermo-viscoelastic materials are particularly sensitive to extreme conditions because the temperature dependence and loading history of the material significantly change the system's ability to dissipate energy and inhibit failure modes, such as dynamic fracture. This is apparent in systems, such as rubber-like tires, where cyclic deformation results in heating of these viscoelastic materials [78] thereby softening and altering the energy absorption. Similarly, highly stretchable strain sensors constructed from a PDMS matrix with aligned CNT inclusions exhibits hysteresis during cyclic loading, resulting from the viscoelasticity of the matrix, which aids the device in enduring cycles of high dynamic strains with minimal damage [69]. For these structured thin-films to be functional, there must be a fundamental understanding of the dynamic behavior and damage-resistance when subjected to extreme environments of high strain-rates and high strains.

1.2 Research Objectives

Hence, this study will focus on understanding the manufacturing of tailored ribbed thin-film systems and the behavior of such systems to extreme conditions using computational models informed by experimental observations. A mechanistic-based framework will be introduced to predict the ribbing behavior of thin-film systems manufactured by large-scale rolling. Additionally, a computational modeling approach is developed and discussed that predicts the thermomechanical behavior of ribbed thin-film systems subjected to high strain-rate loading to design damage-resistant thin-films. Lastly, the large-strain behavior and fracture morphology of CNT-PDMS systems will then be characterized to inform the design and manufacturing of ribbed thin-film systems for multifunctional applications.

1.3 Dissertation Outline

This dissertation is organized as follows: **Chapter 2** presents the computational approaches for the material characterization, finite-element modeling, and uncertainty quantification, that are shared by the remaining chapters; **Chapter 3** discusses the results of experimental and modeling efforts to understand and predict the effect of large-scale rolling on the ribbing morphology of CNT-PDMS thin-films; **Chapter 4** discusses the results of computational models that predict the thermomechanical behavior of thin-films to high strain-rate dynamic loading; and **Chapter 5** presents the morphology of thin PDMS and CNT-PDMS tensile specimens after fracture and investigates how best to characterize the large-strain mechanical behavior. Finally, recommendations for future research are given in **Chapter 6**.

CHAPTER 2: Constitutive Formulations and Numerical Methods

Parts of this chapter are published in *Advanced Engineering Materials* [17], *Macromolecular Materials and Engineering* [82], and *Composites Part A: Applied Science and Manufacturing* [83]

2.1 Introduction

Two topics recur throughout this work: viscoelastic and hyper-viscoelastic material models and finite-element modeling. The important formulations and numerical methods for each of these topics are discussed in this chapter.

2.2 Thermo-Viscoelasticity and Hyper-Viscoelasticity

The theory of linear elasticity accounts for the mechanical behavior of common engineering materials in normal operations, which characterizes the stress-strain response in the small-strain regime by two material parameters—a Young's modulus and Poisson ratio. Thermo-viscoelasticity and hyper-viscoelasticity are other such material descriptions for polymers that account for thermal, large-strain, and high strain-rate physics, which are necessary for understanding the response of polymers in extreme environments. The stress-response of viscoelastic materials can be characterized in the frequency-domain (Chapter 2.2.1) or the time-domain (Chapter 2.2.2), and can account for changes in the modulus with respect to temperature (Chapter 2.2.3) by employing the time-temperature superposition principle. The large-strain behavior of a viscoelastic material can be better represented by coupling both hyperelastic and viscoelastic material models into a single hyper-viscoelastic material model (Chapter 2.2.4).

2.2.1 Frequency-domain viscoelasticity

The mechanical behavior of CNT-PDMS and other such CNT-polymer systems can be modeled as a viscoelastic material because the polymer chains exhibit time- or rate-dependent relaxation [4,17,84]. Prony series viscoelastic material models can take several forms and have been used to represent the relaxation behavior as a function of time or frequency [17,42,84–86]. It is often convenient to characterize the viscoelastic behavior of a material in the frequency-domain by using dynamic mechanical analysis (DMA). An n-term Prony series model for the shear storage, $G'(\omega)$, and the loss moduli, $G''(\omega)$, of a material are given as a function of angular frequency (ω),

$$G'(\omega) = G_0 \sum_{i=1}^{n} \frac{g_i \tau_i^2 \omega^2}{1 + \tau_i^2 \omega^2} + G_\infty \, , \tag{2.1}$$

and

$$G''(\omega) = G_0 \sum_{i=1}^{n} \frac{g_i \tau_i \omega}{1 + \tau_i^2 \omega^2} , \tag{2.2}$$

where G_0 is the instantaneous shear modulus, g_i are the relaxation coefficients corresponding to the time constants τ_i, and G_∞ is the long-term shear modulus given by

$$G_\infty = G_0 \left(1 - \sum_{i=1}^{n} g_i \right) . \tag{2.3}$$

A viscoelastic liquid would require $\sum_{i=1}^{n} g_i \approx 1$, such that the material reduces its ability to resist shear deformations over time (i.e., $G_\infty \approx 0$, according to Equation (2.3)). A viscoelastic solid material, however, would retain some ability to resist shear and thus the sum of relaxation coefficients must be less than unity.

2.2.2 Time-domain viscoelasticity

Although materials are often characterized in the frequency domain using DMA, most modeling efforts are conducted in the time-domain. Thus, the time-dependent viscoelasticity model is also important to consider. When formulated in the time-domain, the Prony series representation of the shear modulus, $G(t)$, is

$$G(t) = G_0 \sum_{i=1}^{n} g_i e^{-\frac{t}{\tau_i}} + G_\infty, \tag{2.4}$$

with the same constants and coefficients as found in the frequency domain [85]. The formulation considers a distribution of possible rate-dependent relaxation mechanisms in the time domain, similar to how Equations (2.1) and (2.2) take into account a distribution of frequency-dependent mechanisms. The time-dependent elongation modulus can be obtained from the shear modulus by assuming a constant Poisson ratio.

2.2.3 Time-temperature superposition for thermo-rheologically simple materials

When thermal effects are considered, the softening of a polymer can be accounted for by the time-temperature superposition principle. The Williams-Landel-Ferry (WLF) model accounts for the temperature effects by the log-scale horizontal shift factor, a_T, given by

$$\log a_T = \frac{C_1(T - T_0)}{C_2 + (T - T_0)}, \tag{2.5}$$

where C_1 and C_2 are fitting coefficients and T_0 is a reference temperature, typically given as room temperature or near the glass-transition temperature [85–88]. The shift factor modifies the frequency-dependent shear moduli at a given temperature with respect to the reference temperature by the relation $G'(\omega, T) = G'(a_T\omega, T_0)$ and $G''(\omega, T) = G''(a_T\omega, T_0)$; the time-dependent modulus is modified by $G(t, T) = G(t/a_T, T_0)$ [85]. Similar relations apply to the material elongation modulus.

2.2.4 Hyper-viscoelastic material behavior

Many hyperelastic material models exist in the literature, each of which is tailored for different materials or strain regimes. A recent review [66] found that the Ogden, Yeoh, Carroll, and Shariff hyperelastic material models have a coefficient of determination (R^2) greater than 0.98 when calibrated with uniaxial tension experimental stress-strain curves of elastomers; other commonly used models had lower R^2 values with 0.65 for Neo-Hookean and 0.59 for Mooney Rivlin. The Yeoh hyperelastic material model was used for the present work according to the recommendations of [66], where the uniaxial stress is given by

$$\sigma_{Yeoh} = 2\left(\lambda_1 - \frac{1}{\lambda_1^2}\right)\left(C_{10} + 2C_{20}(I_1 - 3) + 3C_{30}(I_1 - 3)^2\right), \tag{2.6}$$

where λ_1 is the first principal stretch imposed during uniaxial tensile testing and I_1 is the first stretch invariant given by $I_1 = \lambda_1^2 + 2/\lambda_1$[89,90]. The parameters C_{10}, C_{20}, and C_{30} are obtained by optimizing the material model using experimental data.

The viscoelastic stress contributions are represented by Prony series, a generalized Maxwell model consisting of exponential decaying terms, whose n-term time-dependent relaxation modulus, E_R, is given by

$$E_R(t) = E_0 \sum_{i=1}^{n} \left(1 - g_i \exp\left(-\frac{t}{\tau_i}\right)\right), \tag{2.7}$$

where E_0 is the instantaneous elongation modulus and g_i is the relaxation coefficient corresponding to the relaxation time constant τ_i. Each g_i is bounded between 0 (no relaxation) and 1 (full relaxation) and the sum $\sum_{i=1}^{n} g_i$ is also bounded between 0 and 1, as in Equation (2.4).

The total uniaxial stress, σ, for large-strain viscoelasticity is obtained by

$$\sigma(t) = \int_{-\infty}^{t} E_R(t-\tau)\frac{d\epsilon(\tau)}{d\tau}d\tau \tag{2.8}$$

where ϵ is the uniaxial strain. Evaluating the integral, substituting $g_R(t) = E_R(t)/E_0$ from Equation (2.8) as the non-dimensional viscoelastic relaxation, and defining $\sigma_{Yeoh}(\epsilon(t)) = E_0\epsilon(t)$, provides the total stress as a function of time as

$$\sigma(t) = \sigma_{Yeoh}\big(\epsilon(t)\big) - \int_0^t \dot{g}_R(t-\tau)\sigma_{Yeoh}\big(\epsilon(\tau)\big)d\tau. \tag{2.9}$$

By rearranging Equation (2.9), the combined hyperelastic and viscoelastic stress components gives the uniaxial stress at time t as

$$\sigma(t) = \sigma_{Yeoh}(t) - \sigma_{visc}(t), \tag{2.10}$$

where σ_{visc} is the viscoelastic stress dissipation [71–74]. At time $t + \Delta t$, this gives

$$\sigma(t+\Delta t) = \sigma_{Yeoh}(t+\Delta t) - \sigma_{visc}(t+\Delta t) = \sigma_{Yeoh}(t+\Delta t) - \sum_{i=1}^{n} \sigma_{visc}^{i}(t+\Delta t) \tag{2.11}$$

where the contribution from the i-th Prony series term is obtained by approximating the integral in Equation (2.9) as

$$\begin{aligned}\sigma_{visc}^{i}(t+\Delta t) = \exp\left(-\frac{\Delta t}{\tau_i}\right)\sigma_{visc}^{i}(t) + g_i\sigma_{Yeoh}(t)\left(1 - \exp\left(-\frac{\Delta t}{\tau_i}\right)\right) \\ +g_i\frac{\Delta\mathrm{\sigma}_{\mathrm{Yeoh}}}{\Delta t}\left((\Delta t - \tau_i) + \tau_i \exp\left(-\frac{\Delta t}{\tau_i}\right)\right),\end{aligned} \tag{2.12}$$

which was adapted [71].

2.3 Finite-Element Element Types and Formulations

The finite-element (FE) method is suitable for analyzing complex problems that otherwise have no analytical solution. FE analysis can be conducted in one-, two-, or three-dimensional space, depending on the complexity of the geometry, loading conditions, and behavior. Three-dimensional (3-D) FE analysis was used in the present work to account for the 3-D nature of the manufacturing conditions, ribbed microstructure, and high strain-rate behavior, which required the use of three-dimensional brick elements.

Chapter 3 considers only the mechanical solution and neglects temperature effects. Thus, standard 3-D brick elements were used (Chapter 2.3.1). Chapter 4, however, considers both mechanical and thermal effects so 3-D elements were used that couple the thermal and displacement equations (Chapter 2.3.2).

The solution of dynamic systems using FE requires both that the spatial domain be discretized using elements (Chapters 2.3.1 and 2.3.2) and that the temporal domain be discretized into time-steps (Chapter 2.3.3 and 2.3.4). Finite-difference time-integration schemes evaluate the system of equations at each time-step and updates the mechanical field while considering time-dependent changes in the boundary conditions, contact, and material properties. In Chapter 3, an implicit integration FE scheme as discussed in Chapter 2.3.3 is used to investigate the dynamic behavior of the large-scale rolling of thin-films; in Chapter 4, an explicit integration FE scheme as discussed in Chapter 2.3.4 is used to observe the wave propagation of thin-films subjected to high strain-rate loading.

2.3.1 Three-dimensional displacement brick elements

Physical domains can be discretized into continuum elements that consider the mechanical field solutions and account for contact and large deformations. Other effects, such as thermal, electromagnetic, and acoustic, can also be evaluated using continuum elements, however, only the mechanical effects are considered here. These three-dimensional continuum hexahedra (or "brick") elements evaluate six degrees of freedom: three displacement directions and three rotations directions. The nodal displacement solutions are obtained using either first-order (linear) and second-order (parabolic) interpolation. Linear interpolation requires fewer nodes and therefore fewer equations to resolve the mechanical displacement field, however, parabolic interpolation provides higher accuracy. Linear brick elements were used for the study presented in Chapter 3 with a sufficiently large number of elements to improve the accuracy of the solution.

2.3.2 Three-dimensional thermal-displacement coupled brick elements

Some problems involve both mechanical and thermal effects in which the solution of one is dependent on the solution of the other. In such cases, fully-coupled thermal-displacement brick elements are used, as done in Chapter 4. The thermal-displacement elements obtain the solution for both the six degrees of freedom governing the mechanical displacements in addition to the degrees of freedom governing the temperature. As in Chapter 2.3.1, the displacements can be solved using either linear or parabolic interpolation, though the temperature is often obtained using only linear interpolation to ensure the thermal strain is constant throughout each element.

2.3.3 Finite-element implicit time integration

The Hilber-Hughes-Taylor (HHT) implicit time-integration scheme was used in Chapter 3, which is an unconditionally stable method for linear systems and obtains the updated mechanical field at each time-step. Since the solution is unconditionally stable, larger time-steps can be made than when using a conditionally stable approach, such as explicit integration. The HHT scheme is based on the Newmark approximation method, which seeks a solution to the system of equations

$$M\ddot{u} + Ku = F, \tag{2.13}$$

where M is the mass matrix, K is the stiffness matrix, F is the external force vector, and u and $\ddot{u}$ are the nodal displacement and acceleration vectors. The Newmark method updates the displacements (u) in Equation (2.13) at each new time index $(n + 1)$ by

$$u_{n+1} = u_n + \Delta \mathrm{t}\dot{u}_n + \frac{\Delta \mathrm{t}^2}{2}\left((1 - 2\beta)\ddot{u}_n + 2\beta\ddot{u}_{n+1}\right) \tag{2.14}$$

and the velocities $(\dot{u})$ by

$$\dot{u}_{n+1} = \dot{u}_n + \Delta t(1 - \gamma)\ddot{u}_n + \gamma\ddot{u}_{n+1}, \tag{2.15}$$

where u_n is the state at the previous time-step, Δt is the time-step interval, and β and γ are Newmark parameters selected to control the stability and accuracy of the approximation [91]. In the HHT scheme, an additional parameter, α, is introduced, which creates the family of algorithms whose solution is obtained by solving the corresponding eigenvalue problem of the form $X_{n+1} = AX_n$ where X is the state of nodal displacements, velocities, and accelerations, and A is the amplification matrix [92]. The HHT integration scheme is implemented in ABAQUS [85].

2.3.4 Finite-element explicit time integration

A nonlinear explicit dynamic computational scheme was used in Chapter 4, which is a conditionally stable time-integration method, where the displacement and temperature degrees of freedom are coupled. The fully-coupled thermal-stress analysis procedure is useful for such systems as thermo-viscoelastic materials where it is desirable to obtain the mechanical and thermal solutions simultaneously. A first-order explicit forward-difference time integration rule was used to obtain the updated thermal solution for each new time-step (θ_{n+1}), given by

$$\theta_{n+1} = \theta_n + \Delta t \dot{\theta}_n \tag{2.16}$$

where Δt is the time-step interval, θ_n are the nodal temperatures at the current time-step, and $\dot{\theta}_n$ is the rate of change of the nodal temperatures. At each time-step, the matrix inverse of the lumped capacitance matrix (C_n) was used to determine $\dot{\theta}_n$ by

$$\dot{\theta}_n = C_n^{-1}(P_n - F_n) \tag{2.17}$$

where P_n and F_n are the applied nodal source vector and internal flux vector, respectively [85]. The maximum time-increment for which Equation (2.16) is stable is given by $\Delta t = \frac{L_{min}^2}{2\alpha}$ where L_{min} is the smallest element dimension of the finite-element mesh and α is the thermal diffusivity of the material. Adiabatic heat generation resulting from viscoelastic energy dissipation is accounted for by the thermal energy balance, governed by the volume-average heat flux, $r^{in} = \eta\sigma : \dot{\epsilon}^{in}$, where η is an efficiency factor, σ is the nodal stress state, and $\dot{\epsilon}^{in}$ is the nodal inelastic strains resulting from viscoelastic relaxation.

Similarly, the mechanical solution is obtained using an explicit central-difference integration rule. The updated nodal displacements (u_{n+1}) are obtained at each time-step by

$$u_{n+1} = u_n + \Delta t_{n+1} \dot{u}_{n+\frac{1}{2}} \tag{2.18}$$

with the half-step nodal velocities ($\dot{u}_{n+\frac{1}{2}}$) given by

$$\dot{u}_{n+\frac{1}{2}} = \dot{u}_{n-\frac{1}{2}} + \frac{\Delta t_{n+1} + \Delta t_n}{2} \ddot{u}_n \tag{2.19}$$

and the nodal accelerations ($\ddot{u}_n$) determined by

$$\ddot{u}_n = M_n^{-1}(P_n - I_n) \tag{2.20}$$

where M_n is the lumped mass matrix, and P_n and I_n are the applied nodal load vector and internal force vector, respectively [85]. The stable time-increment governed by the mechanical solution is given by $\Delta t = \frac{L_{min}}{c_d}$ where c_d is the current dilatation wave speed, defined by $c_d = \sqrt{\frac{\lambda+2\mu}{\rho}}$ where ρ is the material density and the Lamè's constants (λ and μ) are determined at the current time-step based on the mean and incremental stresses and strains. Since the system of equations are coupled, the most restrictive stable time-step is used and the thermal and mechanical solutions are obtained simultaneously at each time-step.

CHAPTER 3: Finite-Element Modeling of 3-D Ribbing Instabilities Manufactured by Twin-Roll Coating Process

Part of this chapter is published in *Advanced Engineering Materials* [17].

3.1 Introduction

Periodic ribbing structures, though historically viewed as material surface defects, present many opportunities for multifunctional applications if the microstructure is controlled. The manufacturing of thin-films with these structured surfaces by large-scale rolling has distinct advantages over other techniques, such as lithography, due to scalability. However, it is not well understood or quantified how the processing conditions or material properties affect the microstructure at different physical scales. Hence, the objective of this chapter is to develop a finite-element model of the symmetric forward-roll coating process to understand, predict, and control the morphology of carbon nanotube (CNT)-PDMS pastes. Dynamic mechanical analysis was used to obtain the viscoelastic properties of the CNT-PDMS paste for various CNT weight distributions. The CNT-PDMS thin-film system was modeled by a nonlinear implicit dynamic finite-element (FE) method that accounted for ribbing instabilities, large displacements, rolling contact, and material viscoelasticity. The effects of the thin-film rheological properties and the roller gap on the ribbing behavior were predicted by the computational models and a ribbing instability model was formulated to design the CNT-PDMS thin-films for multifunctional applications. Furthermore, a Morris sensitivity analysis was conducted to obtain insights on the dominant predicted characteristics pertaining to the ribbing microstructure.

3.2 Viscoelastic Characterization of Uncured PDMS and CNT-PDMS

Multi-walled CNT inclusions were mixed with PDMS Sylgard 184 (Dow) to create the CNT-PDMS paste for material characterization and large-scale rolling. The CNT inclusions had a diameter between 6 and 9 nm and a length between 100 and 200 μm. CNT-PDMS paste with a CNT content of 0, 1, and 3.5 weight percent (wt%) was used. The CNT inclusions and PDMS matrix for each composition were mixed for ten minutes using a universal planetary mixer to disperse the inclusions throughout the matrix. The hardener from the Sylgard 184 elastomer kit was then added to the mixture in a 10:1 ratio. The CNT-PDMS mixture with the hardener was further mixed using a three-roll high-shear milling machine. The mixture was placed on one end of the rollers and then collected at the other end. The paste was rolled multiple times reducing the roller gaps after each pass. Further information about the paste formulation is detailed in [14].

Dynamic mechanical analysis (DMA) was conducted on each CNT-PDMS paste to determine how CNT inclusions affect rheological properties. The hardener from the elastomer kit was not added for this analysis to prevent the PDMS from curing during the test. A TA Instruments Discovery Hybrid-3 rheometer was used with an 8 mm cross-hatched parallel plate geometry, and the temperature was maintained at 25°C by using a TA Instruments Peltier plate. The specimen was loaded in the tray with a spatula. No pre-shearing was performed since the specimens would eject in shear deformations from the rheometer. An angular frequency sweep between 10^{-1} and 10^{2} radians per second was applied and the material shear storage (G') and loss (G'') moduli were recorded. The test was repeated for a total of three specimens for each CNT wt%.

The shear moduli were obtained with respect to the angular frequency for each CNT content tested (Figure 3.1). Neat PDMS exhibited polymer melt behavior since the loss modulus was several orders of magnitude larger than the storage modulus. CNT-PDMS, however, had a storage modulus that was greater than the loss modulus, which substantiates that the material is a viscoelastic solid [51]. Viscosity measurements by [4] for PDMS with varying CNT content further substantiates that the solid, paste-like behavior can be obtained with as little as 1 wt% CNT.

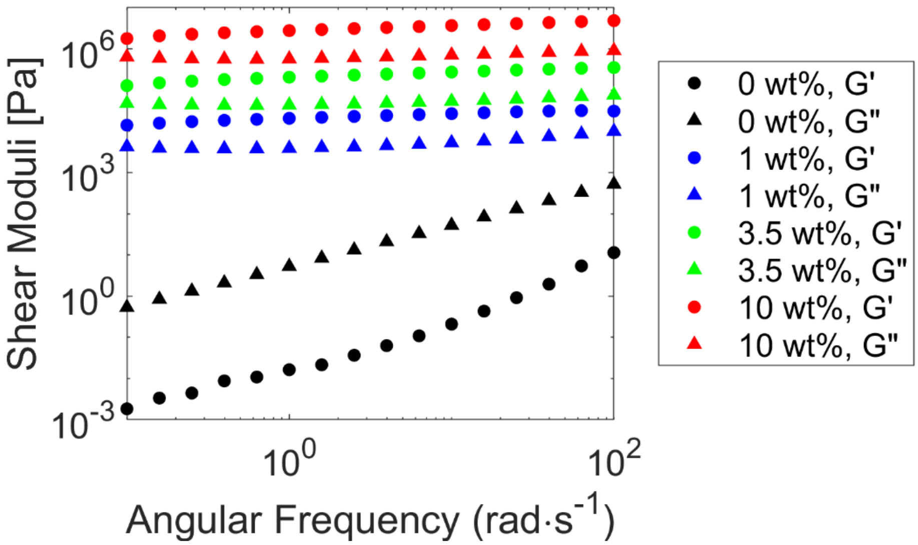

Figure 3.1. Shear storage (G') and loss ($G"$) moduli recorded as a function of the angular frequency by dynamic mechanical analysis for CNT-PDMS paste with varying CNT weight percent (wt%) content.

The moduli master curves (Figure 3.1) were then used to obtain the Prony series viscoelastic material model for the CNT-PDMS pastes by solving a constrained optimization problem. Four Prony time-constants, τ_i, were selected to characterize the materials: τ_1 = 10^{-2} s, τ_1 = 10^{-1} s, τ_1 = 10^{0} s, and τ_1 = 10^{1} s, which are related to the DMA testing parameters. The independent parameters were defined as the set $\boldsymbol{q} = \{G_0,\ g_1,\ g_2,\ g_3,\ g_4\}$, where G_0 is the instantaneous modulus and each g_i is the Prony series relaxation coefficient corresponding to each τ_i. The set of parameters, $\boldsymbol{q}$, was obtained by minimizing the sum-of-square error between the DMA data (G' and G'') and Prony series approximation ($\hat{G}'$ and $\hat{G}''$) given by

$$f(\boldsymbol{q}) = \sum_{j=1}^{m} \left[\left(\hat{G}'(\omega_j; \boldsymbol{q}) - G'(\omega_j) \right)^2 + \left(\hat{G}''(\omega_j; \boldsymbol{q}) - G''(\omega_j) \right)^2 \right], \tag{3.1}$$

where $m = 16$ is the number of frequencies applied by DMA subject to parameter bounds $\sum_{i=1}^{4} g_i \leq 1$, $0 \leq g_i \leq 1$, and $G_{0,min} \leq G_0$, and $G_{0,min}$ is the lower bound of the storage modulus recorded by DMA. The parameter bounds ensure that the material relaxation is bounded between 0 (indicating no relaxation) and 1 (indicating complete relaxation). The optimized instantaneous shear modulus, G_0, is expected to be higher than the value obtained from DMA, $G_{0,min}$, because testing at higher frequencies has been observed to increase the modulus.

A deterministic constrained optimization scheme and delayed rejection adaptive metropolis (DRAM) Bayesian fitting routine were used to solve Equation (3.1). Bayesian credible and prediction intervals of the material models were constructed on the interval between the angular frequency, ω, of 10^{-2} and 10^{3} radians per second, extending one logarithmic decade from the data obtained by DMA. The resulting Prony series viscoelastic material models for the CNT-PDMS systems are shown in Figure 3.2.

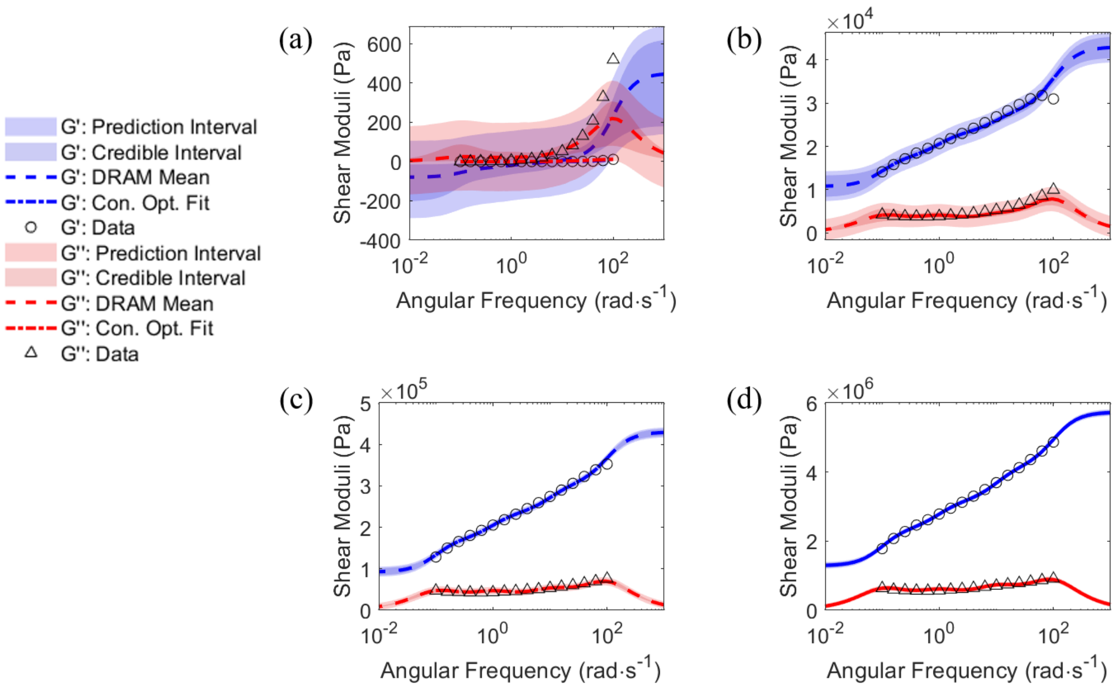

Figure 3.2. Prony series material model of shear storage and loss moduli for (a) 0 wt% CNT (neat PDMS), (b) 1 wt% CNT, and (c) 3.5 wt% CNT obtained by delayed rejection adaptive metropolis (DRAM) Bayesian routine and by constrained optimization (Con. Opt. Fit) according to Equation (3.1) compared to data obtained by dynamic mechanical analysis.

Neat PDMS (Figure 3.2a) cannot be fit reasonably with a viscoelastic material model as demonstrated by the large uncertainty of the moduli, which incorrectly suggests that the material may have a negative modulus. The addition of CNT inclusions (Figure 3.2b-d), however, increases the moduli and the paste can then be characterized as a viscoelastic material using either approach with comparable results and reasonable uncertainty. The prediction intervals outside of the bounds of the frequency sweep indicate that the loss modulus approaches zero and the storage modulus converges to a maximum value for each material as the angular frequency increases. Increasing the range of the frequency sweep conducted during DMA would improve the material models in the outer intervals but was not feasible given the physical limits of the rheometer.

The parameter-estimate history (Figure 3.3) from the DRAM optimization procedure allows for us to further understand the difference in obtaining a physically-realistic material model for PDMS and CNT-PDMS. At each iteration, the Bayesian approach suggests a set of new parameters from a prior distribution, evaluates the model, and decides to accept the updated parameters based on if the model is improved and a probability function. The history of parameters, also called the parameter chains, indicates how much the Bayesian optimization procedure explores the parameter space—narrow parameter distributions suggest the parameter space is not being searched fully, whereas wide distributions suggest the space has been explored and provides greater surety that the design is optimal. 500,000 chain iterations were obtained for each material composition; the last 250,000 iterations were used to construct the parameter probability distributions to allow for chain burn-in.

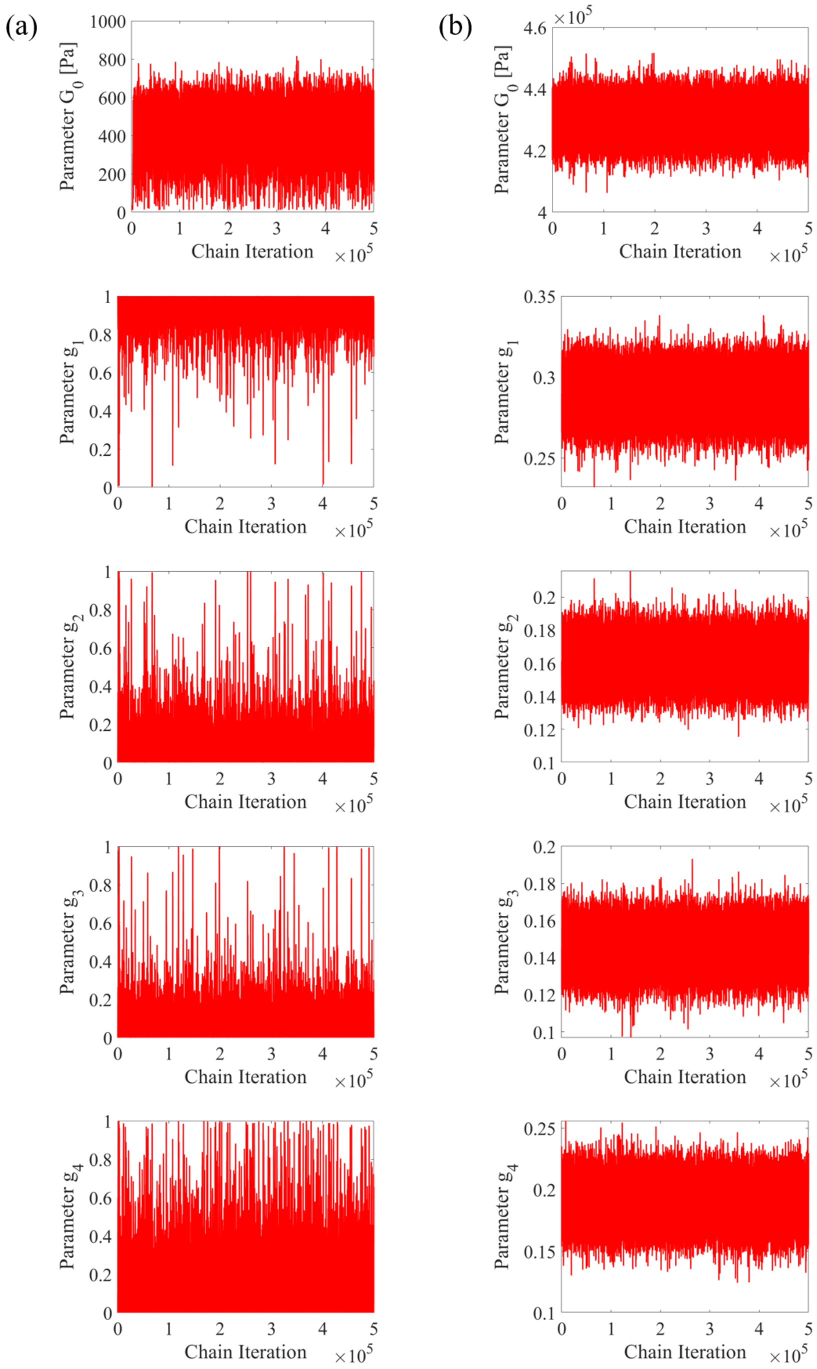

Figure 3.3. Delayed rejection adaptive metropolis (DRAM) Results for (a) uncured PDMS and (b) CNT-PDMS with 3.5 wt% CNT.

The chain iterations for PDMS (Figure 3.3a) explore the full parameter space, given that they span 800 Pa for the instantaneous modulus, G_0, and the entire constrained parameter range of $0 \leq g_i \leq 1$ for each Prony series relaxation coefficient. The rugged profile of the chains for each relaxation coefficient in Figure 3.3a substantiate the inability to properly characterize uncured PDMS as a viscoelastic material because these parameters approach the constraint $g_i \leq 1$ and cannot form a normal posterior distribution centered at a mean value. There is a stark contrast between the chains in Figure 3.3a for PDMS and in Figure 3.3b for CNT-PDMS with 3.5 wt% CNT: the parameter space is explored fully for all five parameters in Figure 3.3b and the chains form normal distributions around a mean value. The parameter estimate for each parameter is the mean value from the last 250,000 chain iterations; the standard deviation is obtained from the normal distribution of the chains.

The material model parameters obtained by DRAM and the constrained optimization are summarized in Table 3.1 for PDMS, Table 3.2 for CNT-PDMS with 1 wt% CNT, Table 3.3 for CNT-PDMS with 3.5 wt% CNT, and Table 3.4 for CNT-PDMS with 10 wt% CNT.

Table 3.1. Prony series parameter values for PDMS viscoelastic material model governed by Equations (2.1) and (2.2) determined using constrained optimization (Con. Opt.) and delayed rejection adaptive metropolis (DRAM) schemes.

Fitting Routine	Instantaneous Modulus, G_0 (kPa)	Relaxation Coefficient, g_1	Relaxation Coefficient, g_2	Relaxation Coefficient, g_3	Relaxation Coefficient, g_4
Con. Opt.	0.5279	1.0000	0.0000	0.0000	0.0000
DRAM	0.4616	0.9983	0.0039	0.0033	0.0036

Table 3.2. Prony series parameter values for CNT-PDMS with 1 weight percent CNT viscoelastic material model governed by Equations (2.1) and (2.2) determined using constrained optimization (Con. Opt.) and delayed rejection adaptive metropolis (DRAM) schemes.

Fitting Routine	Instantaneous Modulus, G_0 (kPa)	Relaxation Coefficient, g_1	Relaxation Coefficient, g_2	Relaxation Coefficient, g_3	Relaxation Coefficient, g_4
Con. Opt.	43.1232	0.3407	0.1175	0.1296	0.1633
DRAM	43.0493	0.3388	0.1177	0.1282	0.1644

Table 3.3. Prony series parameter values for CNT-PDMS with 3.5 weight percent CNT viscoelastic material model governed by Equations (2.1) and (2.2) determined using constrained optimization (Con. Opt.) and delayed rejection adaptive metropolis (DRAM) schemes.

Fitting Routine	Instantaneous Modulus, G_0 (kPa)	Relaxation Coefficient, g_1	Relaxation Coefficient, g_2	Relaxation Coefficient, g_3	Relaxation Coefficient, g_4
Con. Opt.	430.130	0.2897	0.1611	0.1451	0.1895
DRAM	429.629	0.2900	0.1615	0.1454	0.1902

Table 3.4. Prony series parameter values for CNT-PDMS with 10 weight percent CNT viscoelastic material model governed by Equations (2.1) and (2.2) determined using constrained optimization (Con. Opt.) and delayed rejection adaptive metropolis (DRAM) schemes.

Fitting Routine	Instantaneous Modulus, G_0 (kPa)	Relaxation Coefficient, g_1	Relaxation Coefficient, g_2	Relaxation Coefficient, g_3	Relaxation Coefficient, g_4
Con. Opt.	5734.460	0.2731	0.1725	0.1378	0.1917
DRAM	5730.857	0.2731	0.1723	0.1377	0.1915

Since the constrained optimization approach is subject to the possibility of finding a local rather than global minimum, DRAM was used to ensure the parameter space was explored fully. The small discrepancy in the parameter estimates obtained by the Bayesian approach in Tables 3.1 to 3.4 validates the deterministic results and ensures that the solution is a global minimum rather than a local minimum. Without CNTs, the instantaneous shear modulus, G_0, of PDMS is on the order of 0.5 kPa (Table 3.1); adding CNTs increases the modulus by a factor of 10,000 (Table 3.4). Additionally, PDMS relaxes almost instantaneously (within τ_1 = 10^{-2} s), but the addition of CNTs inhibits the polymer chains from fully relaxing and introduces additional relaxation mechanisms that prolong the relaxation behavior of the material.

The parametric rolling study in Chapter 3.3 uses CNT-PDMS with 3.5 wt% CNT. Table 3.3 provides two comparable viscoelastic models for this material obtained by different optimization schemes. To determine which material model should be used, the standard deviations of the parameters from each optimization procedure are listed in Table 3.5.

Table 3.5. Standard deviation of Prony series parameters for 3.5 wt% CNT material model governed by Equations (2.1) and (2.2) found by constrained optimization (Con. Opt.) and delayed rejection adaptive metropolis (DRAM) schemes.

Fitting Routine	σ_{G_0} (kPa)	σ_{g_1}	σ_2	σ_{g_3}	σ_{g_4}
Con. Opt.	4.100	0.0094	0.0086	0.0079	0.0121
DRAM	4.433	0.0102	0.0093	0.0085	0.0130

The standard deviations of the material model parameters obtained by the constrained optimization routine are lower than those obtained by the DRAM scheme. Thus, the Prony series coefficients obtained by the constrained optimization routine (Table 3.3) and the corresponding time constants were used for the 3.5 wt% CNT material model. From Equation (2.3), the long-term shear modulus of the material is G_∞ = 92.306 kPa. The long-term modulus is sufficiently large to resist surface tension-driven flattening that was observed in [4,6,26], so the material is anticipated to retain the ribbed structure after being removed from the roller.

The time-dependent normalized shear relaxation behavior is shown in Figure 3.4. The shear modulus at time t = 0 seconds is the normalized instantaneous modulus (G_0/G_0); the modulus approaches the normalized long-term modulus (G_∞/G_0) as the time approaches infinity. Applying the constant Poisson ratio obtained by the rule of mixtures yields an instantaneous elongation modulus of E_0 = 1.26 MPa and long-term elongation modulus of E_∞ = 266 kPa. In [38], the compressive modulus for CNT-PDMS with 2 wt% CNT loading was 0.979 MPa and was 1.434

MPa with 5 wt%. Interpolating between these values for 3.5 wt% CNT gives a compressive modulus of 1.207 MPa, which gives us confidence that our material model is realistic.

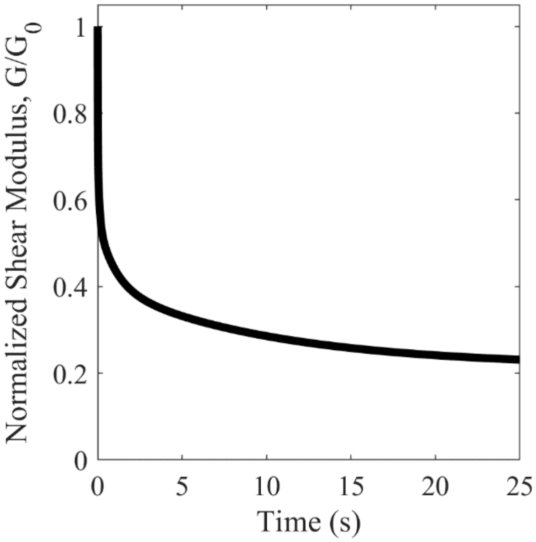

Figure 3.4. Time response of the shear modulus for CNT-PDMS paste with 3.5 wt% CNT governed by Equation (2.4) with Prony series time constants (τ_1 = 10^{-2}, τ_1 = 10^{-1}, τ_1 = 10^{0}, τ_1 = 10^{1}), relaxation coefficients (Table 3.3), instantaneous shear modulus (G_0) (Table 3.3), and long-term shear modulus (G_∞) obtained by Equation (2.3). This material model is used to predict the behavior of ribbed CNT-PDMS during large-scale rolling.

3.3 Characterization of Ribbed Thin-Film Morphology

A two-roll coating machine (Figure 3.5a) was used to fabricate CNT-PDMS specimens with a ribbed microstructure. Each roller had a radius of R = 25.4 mm and could rotate independently of the other roller. A polyimide sleeve was wrapped around one roller so the film could be transferred after rolling. The CNT-PDMS paste formulated by the method described in

Chapter 3.2 was placed between the rollers. The paste adhered to the roller surface and polyimide substrate and spread into a thin film with a ribbed profile after several revolutions. The rollers were stopped, the polyimide sleeve was removed with the film still adhered (Figure 3.5b), and the paste was transferred to the oven where it was cured at 125°C for 25 minutes. The resulting surface morphology was evaluated using a high-resolution FEI Verios 460 L scanning electron microscope (SEM).

The CNT-PDMS paste with 3.5 wt% CNT content was used as a model material to investigate the effect of the roller gap on the ribbing microstructure. The rotational speed of both rollers (ω) was set to 20 RPM. Only the roller gap (h) was varied in this analysis. The roller gap was changed between 250 μm and 450 μm in increments of 50 μm resulting in five specimens. The ribbing microstructure of each specimen was evaluated by SEM imaging and visual inspection to determine the influence of the roller gap on the morphology, namely, the ribbing wavelength (λ) and amplitude (A).

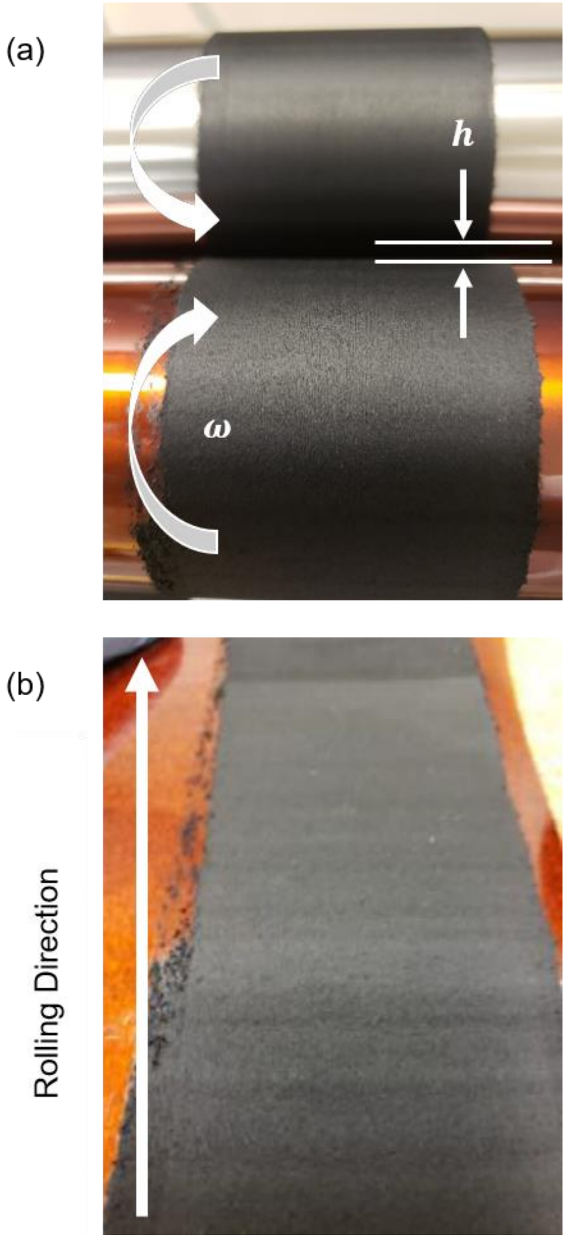

Figure 3.5. (a) The rolling of the CNT-PDMS paste with 3.5 wt% CNT content for rotational speed (ω) and roller gap (h), (b) the cured CNT-PDMS ribbed material adhered to the polyimide sleeve.

It is essential to understand how the CNT-PDMS microstructure evolves due to the symmetric forward-roll coating process. SEM imaging allows for the surface of the post-rolled and cured

CNT-PDMS film to be characterized. Studies by [39] showed that the distribution and orientation of CNTs do not change during the curing process so the microstructure is directly controlled by the rolling procedure. The average ribbing peak-to-peak wavelength was obtained for each of the five specimens. Figure 3.6 shows the microstructure of the CNT-PDMS specimens after being rolled and cured.

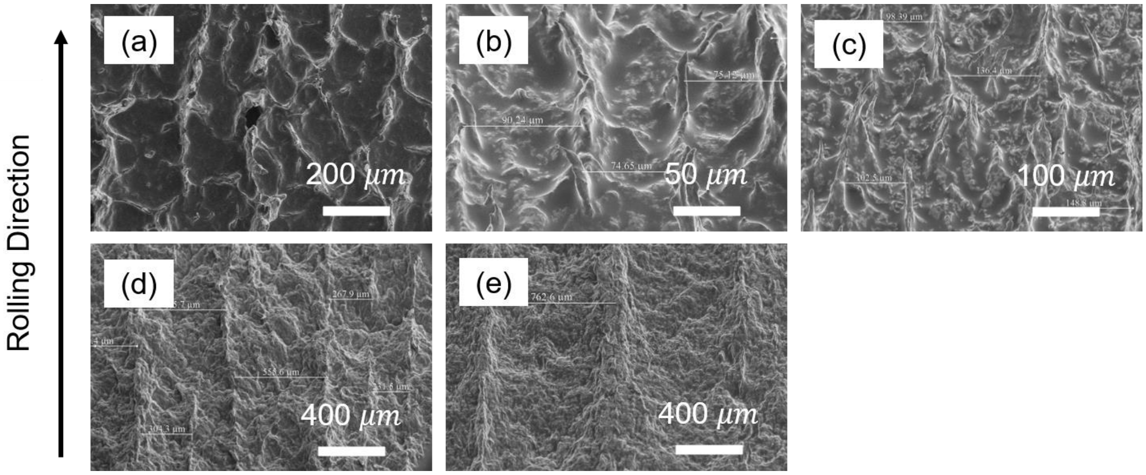

Figure 3.6. Scanning electron microscopy images of CNT-PDMS ribbed microstructure produced by varying the roller gap (h) for (a) specimen A, h = 250 μm, (b) specimen B, h = 300 μm, (c) specimen C, h = 350 μm, (d) specimen D, h = 400 μm, and (e) specimen E, h = 450 μm.

Ribbing was observed in all specimens (Figure 3.6) without shear induced by a roller speed differential as was observed in [6], which suggests that there may be greater independence of the roller speed ratio than initially reported. Similar to experimental observations from [6], individual CNTs appear at the crests of the ribs in Figure 3.6 (most easily seen in Figure 3.6b) resulting from capillary bridging, which also indicates that the proposed manufacturing process does not destroy the CNTs, thereby preserving the mechanical properties of the nanofiller and the final ribbed thin-film material. Since distinct columns are visible in each specimen, the ribbing behavior can be assumed to be sinusoidal with a single peak-to-peak ribbing wavelength (λ) as done in [6,21,23,25,27,29,52,53]. SEM images provided the average ribbing peak-to-peak wavelengths. The visual inspection found the film thickness (H) to be about 1.2 times larger than the gap distance (h) for each specimen. The ribbing amplitude was not measured directly via SEM; it was approximated as half the difference between the film thickness and the prescribed roller gap. Table 3.6 summarizes the microstructure measurements of the CNT-PDMS thin-film specimens. The ribbing wavelength increases with an increasing gap, which is consistent with [6,21,23,52,53] except for the smallest roller gap setting. This increasing trend was also observed for Newtonian and viscoelastic liquids with no fillers [21,23,52,53] and for CNT-PDMS paste with 10 wt% CNT [6]. The magnitudes of the predicted ribbing amplitudes are consistent with experimental observations for similar material systems and operating conditions [6].

Table 3.6. Experimental microstructural measurements of post-rolled CNT-PDMS specimens after curing, ribbing wavelength measurements approximated for use in finite-element models.

Specimen	Roller Gap (μm)	Film Thickness	Ribbing Amplitude (μm)	Ribbing Wavelength (μm)
A	250	300	25	$283 \approx 300$
B	300	360	30	$92 \approx 100$
C	350	420	35	$152 \approx 150$
D	400	480	40	$325 \approx 300$
E	450	540	45	$623 \approx 600$

The ribbing wavelength and amplitude of the five specimens provide characteristic measures of the surface morphologies of the ribbed films. These characteristics lengths are important in predicting and designing the film for such multifunctional applications as drag reduction, superhydrophobicity, and anti-icing [4,6,7]. For example, in [7] the probability of forming ice on a nanoparticle-composite coated plate decreased with decreasing particle size. Finite-element predictions can be used to inform how to best design these structured thin-film systems using the microstructural observations from Table 3.6 and the viscoelastic material model from Chapter 3.2.

3.4 Finite-Element Model Set-up of Large-Scale Rolling

The Prony series viscoelastic material model and the microstructural measurements were used with a nonlinear implicit dynamic computational scheme to investigate the ribbing evolution of CNT-PDMS thin-film systems in ABAQUS [26]. Five FE models were configured to replicate the experimental conditions of the five experimental specimens. A non-ribbed mesh with zero ribbing amplitude was also constructed based on the geometric parameters of the first FE model to serve as a control. Figure 3.7 shows the setup for the first model.

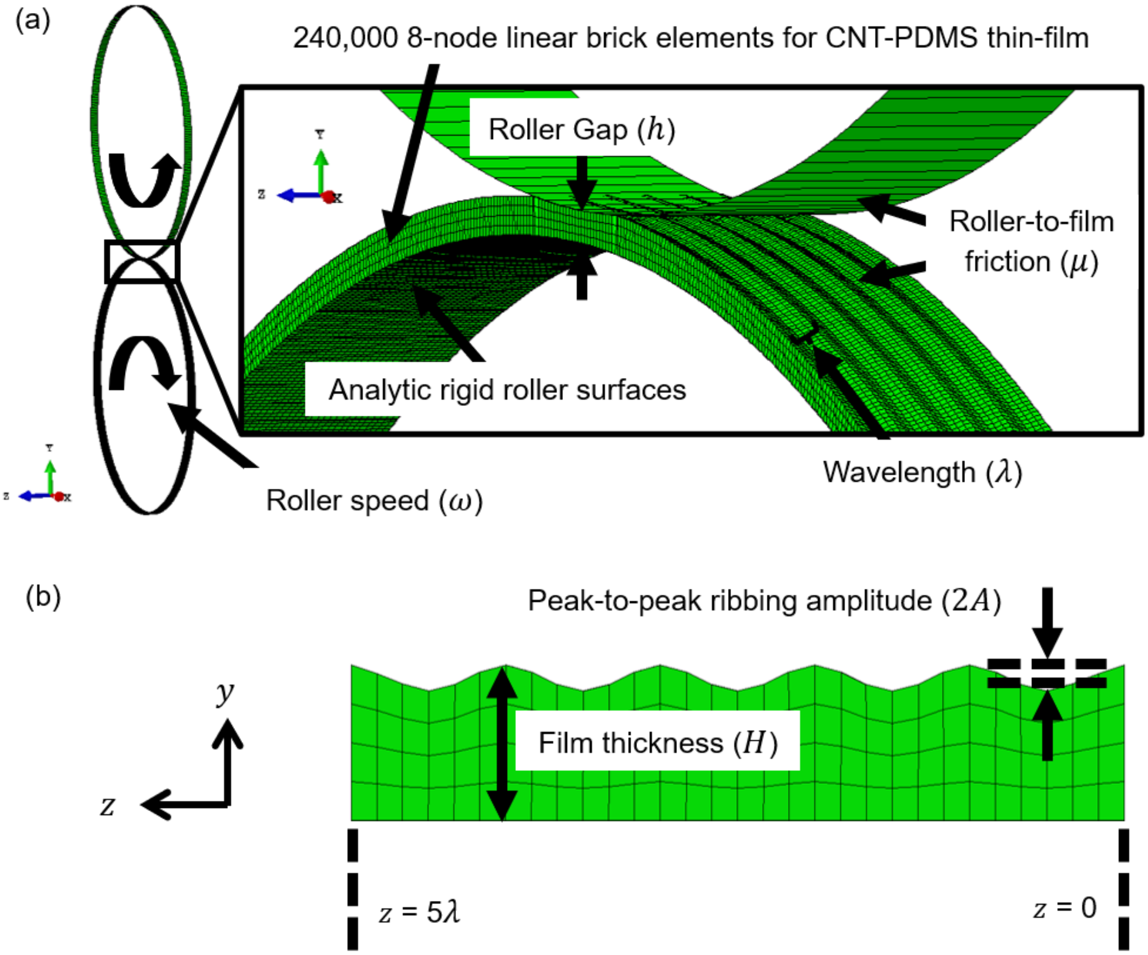
(a)
240,000 8-node linear brick elements for CNT-PDMS thin-film
Roller Gap (h)
Roller-to-film friction (μ)
Analytic rigid roller surfaces
Wavelength (λ)
Roller speed (ω)
(b)
Peak-to-peak ribbing amplitude ($2A$)
y
z
Film thickness (H)
$z = 5\lambda$
$z = 0$

Figure 3.7. (a) Three-dimensional finite-element model of the two-roll coating process producing ribbed CNT-PDMS material with film, rollers, roller gap (h), rotational speed (ω), friction (μ), and wavelength (λ) identified, (b) cross-section of film in the gap showing five ribbing periods with ribbing amplitude (A) and film thickness (H).

The CNT-PDMS paste with the 3.5 wt% CNT content was assumed to have homogeneous, isotropic material properties resulting from the mixing procedure before conducting the rolling process. The elongation moduli and Prony series determined by the procedure from Chapter 3.2 with a Poisson ratio $\nu = 0.44$ is representative of the time-dependent material relaxation according to Equation (2.7). Thermomechanical properties, such as the Williams-Landel-Ferry (WLF) coefficients discussed in Chapter 2.2.3 were not included in the model since thermodynamic effects were neglected for this chapter [88].

The rotational speed (ω) of both rollers was set as 20 RPM to match the speed used in the experiments. Tie constraints connected the bottom surface of the film to the bottom roller to prohibit slip and penetration of the film relative to the roller [31]. A friction coefficient of μ = 0.90 was applied between the top roller and the film surface to account for the rough contact; Lagrange penalty functions were used to resolve the contact. The nonlinear equilibrium equations resulting from large deformations were solved at each time-step with the implicit trapezoidal rule using Newton's method with adaptive time-stepping and five percent numerical damping to improve solution stability due to contact. 240,000 three-dimensional 8-node linear brick elements were used based on a convergence analysis to model the mechanical response of the thin-film; the rollers were treated as analytic rigid surfaces. Five ribbing periods were modeled for each mesh and symmetric boundary conditions were applied to the free faces of the film at z = 0 and z = 5λ (Figure 3.7b). The film geometry of each model was specified with the film thickness, ribbing wavelength, and ribbing amplitude as determined by SEM and visual inspection. The only difference between the five models was the film geometry.

3.5 Large-Scale Rolling Finite-Element Results

The proposed viscoelastic material model and FE computational approach were used to investigate the ribbing behavior of CNT-PDMS thin-film systems with 3.5 wt% CNT content for varying roller gaps. The FE models were based on the experimental operating conditions and microstructural measurements, to investigate the effect of the roller gap and ribbing microstructure on the stress-state of the film. A mesh convergence study found that six elements per wavelength and four through the thickness were sufficient to resolve the film stress during the rolling process. Since the rolling rate (20 RPM $\approx$ 2.1 rad·s^{-1}) was between the bounds of the frequency sweep conducted by DMA the material model can represent the behavior of the film accurately. Based on [4], the complex viscosity of the material is approximately 100 kPa·s at the given rolling rate. The microstructural measurements from experiments and film stresses from FE models were related in a ribbing instability model to predict the film morphology that results from a given non-dimensional roller gap during rolling.

3.5.1 The effects of local stresses on ribbing

Experimental microstructural measurements (Table 3.6) were used for the FE models. The local stress-state of the first mesh corresponding to Specimen A was used to investigate the behavior of the ribbed material (Figure 3.8). The Von Mises stress normalized by the instantaneous elongation modulus of the material suggests that the maximum stress is approximately one-third of the instantaneous modulus at the top surface of the outer-most peaks. Based on the frequency of rotation, the elongation modulus of the film is approximately 650 kPa according to the material model from Chapter 3.2. We expect the normalized stress to be larger for faster rolling speeds because the viscoelastic film would have less time to relax, thereby increasing the modulus. At the cross-section (Figure 3.8b), the ribbing profile has flattened completely between the rollers and the resulting stress exhibits a periodic fluctuation corresponding to the pre-ribbed geometry. The ribbing instabilities are formed in the meniscus of the film, which is consistent with experimental [23,24], analytical [22,27], and computational [26,28] investigations. Downstream of the gap, the restoring forces of the film prevent the ribs from leveling and instead retain their shape after being formed as was observed experimentally [4,6]. This result confirms our hypothesis that the material would have sufficient strength to prevent the instabilities from leveling. Based on [26], the addition of the high aspect ratio elastic filler in the liquid matrix prevents the flow-field transition from occurring on a time-scale long enough that it at least allows for the 25-minute cure cycle to complete.

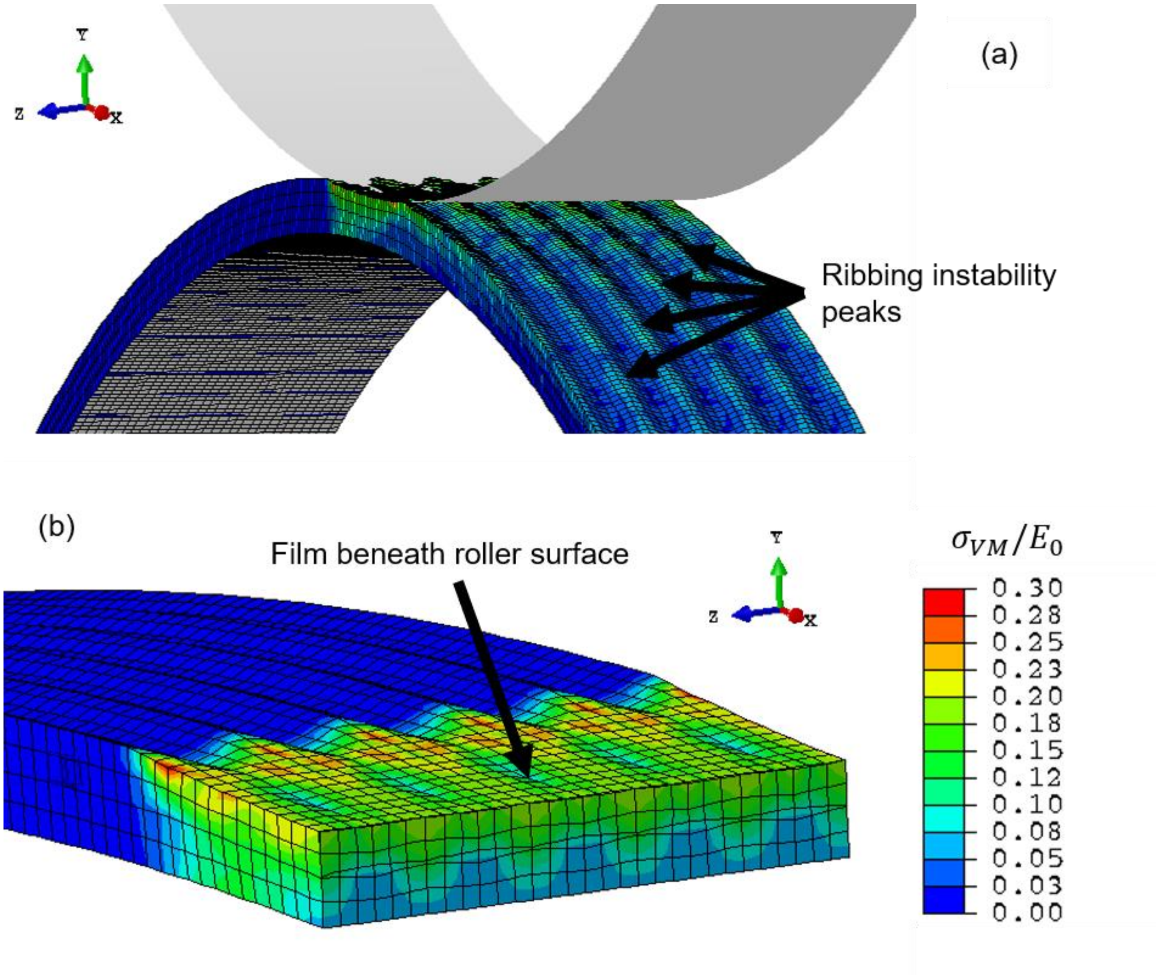
Y
Z
X
(a)
Ribbing instability peaks
(b)
Film beneath roller surface
Y
Z
X
σ_{VM}/E_0
0.30
0.28
0.25
0.23
0.20
0.18
0.15
0.12
0.10
0.08
0.05
0.03
0.00

Figure 3.8. (a) Von Mises stress (σ_{VM}) normalized by the instantaneous elongation modulus (E_0) of finite-element mesh corresponding to specimen A showing stress evolution of ribbed film passing through roller gap and the retention of the ribbing profile downstream of the gap, (b) cross-section of the thin-film between rollers with roller surfaces removed to view the film surface.

To provide a benchmark to better understand the effect of ribbing instabilities on the local stress-state, a non-ribbed mesh was also constructed with the same parameters as the mesh shown in Figure 3.9, except the ribbing amplitude was set to zero for a smooth surface. After excluding the edge regions to omit boundary effects, as shown in the inset of Figure 3.9, the resulting normalized Von Mises stress was a uniform stress field of 0.008 in the roller gap.

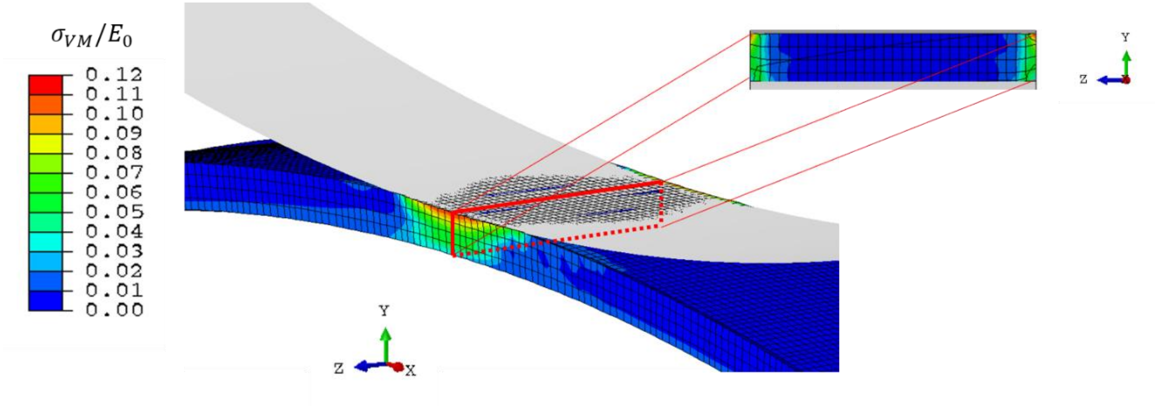

Figure 3.9. Von Mises stress (σ_{VM}) normalized by the instantaneous elongation modulus (E_0) of non-ribbed finite-element mesh with similar conditions to specimen A. The stress distribution is uniform through the film width (z-direction) after excluding edge effects. Inset image shows normalized stress distribution in cross-section between the rollers.

The stress state between the rollers for the non-ribbed mesh (Figure 3.9) is uniform, unlike for the ribbed thin-film (Figure 3.8) because of the structured surface. The only difference between Figures 3.8 and 3.9 is the ribbing morphology; thus, introducing a ribbed surface increases the normalized Von Mises stress by several orders of magnitude.

To further understand the mechanical behavior of the thin-film system, we obtained the six three-dimensional stress components, which are normalized by the instantaneous elongation modulus (Figure 3.10). The x-coordinate corresponds to the rolling direction, the y-coordinate to the film thickness direction, and the z-component to the ribbing wavelength direction.

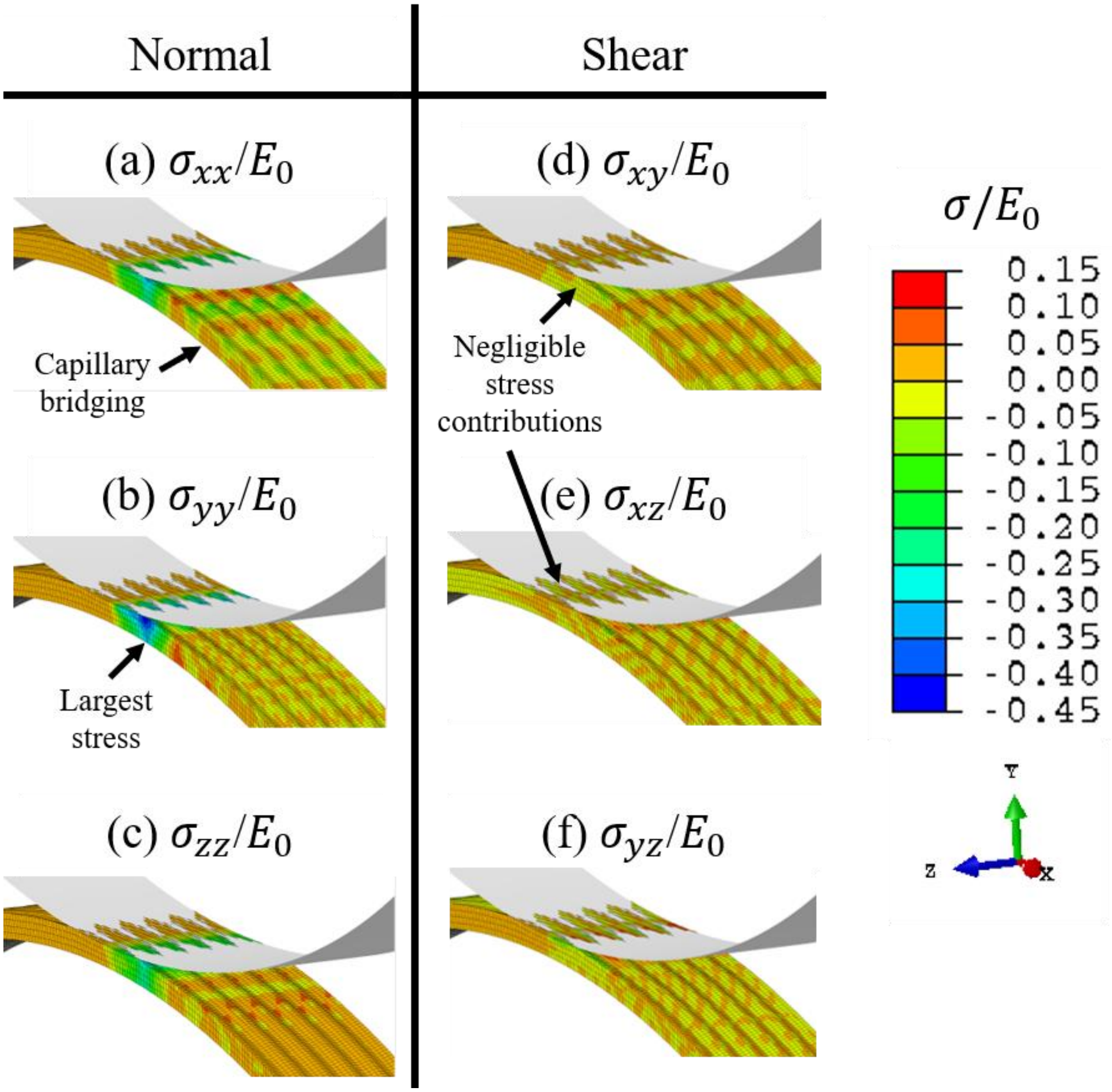
Normal
Shear
(a) σ_{xx}/E_0
Capillary bridging
(b) σ_{yy}/E_0
Largest stress
(c) σ_{zz}/E_0
(d) σ_{xy}/E_0
Negligible stress contributions
(e) σ_{xz}/E_0
(f) σ_{yz}/E_0
σ/E_0
0.15
0.10
0.05
0.00
-0.05
-0.10
-0.15
-0.20
-0.25
-0.30
-0.35
-0.40
-0.45
Y
Z
X

Figure 3.10. Normalized three-dimensional stress components of the ribbed film finite-element mesh corresponding to specimen A.

The normal stress in the x-direction (Figure 3.10a, σ_{xx}/E_0) has the largest magnitude at the crests immediately after passing through the rollers. The stress is negative at this location, which indicates that the ribbing instabilities contract in the rolling direction. The periodicity of the contractions in the rolling direction is related to the capillary bridging wavelength [4,6]. This behavior has been observed in [6] to provide the bristled “shark-skin” like texture of the surface that improved the superhydrophobicity of the film.

The largest stress component of the film is in the thickness direction (Figure 3.10b, σ_{yy}/E_0), which is nearly half the value of the instantaneous elongation modulus. The stress in this direction corresponds to the top roller reducing the thickness of the film as it passes through the roller gap. The magnitude of the normal stress substantiates the large deformations that the ribbed film is subjected to during the rolling process. The dominant shear stress in the first model is in the yz-direction (Figure 3.10f, σ_{yz}/E_0), which relates to the flattening and reformation of the ribbed profile. The remaining two shear stresses are negligible in magnitude compared to the other stress components.

3.5.2 The effects of the roller gap on the ribbing behavior

To understand the effects of the prescribed roller gap on the ribbing microstructure we introduced the non-dimensional roller gap (R/h), which is the ratio of the roller radius to the roller gap [4,25,26,52,53], and the non-dimensional ribbing aspect ratio ($a_r = A/\lambda$) as the ribbing amplitude divided by the ribbing wavelength [9,93]. From Table 3.6, Specimen E and its corresponding FE model have the smallest non-dimensional roller gap (R/h = 56.44) and ribbing aspect ratio (a_r = 0.075); Specimen B and its FE model have a non-dimensional gap of R/h = 84.67 and the largest ribbing aspect ratio (a_r = 0.300). The normalized Von Mises stress in the cross-section of the roller gap of the five FE models are given in Figure 3.11.

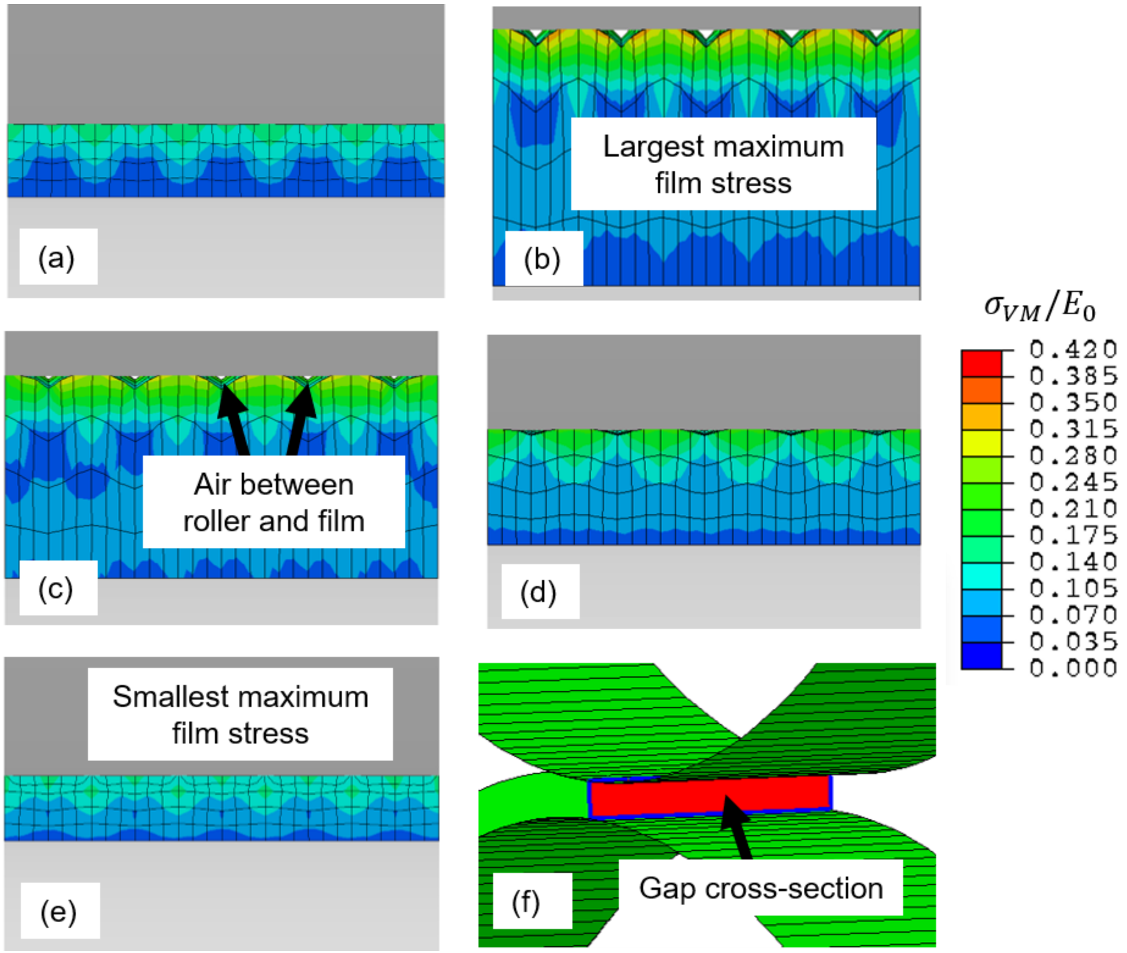

Largest maximum film stress
(a)
(b)
Air between roller and film
(c)
(d)
Smallest maximum film stress
(e)
(f)
Gap cross-section
σ_{VM}/E_0
0.420
0.385
0.350
0.315
0.280
0.245
0.210
0.175
0.140
0.105
0.070
0.035
0.000

Figure 3.11. Von Mises stress (σ_{VM}) normalized by the instantaneous elongation modulus (E_0) of finite-element models corresponding to (a) mesh A, (b) mesh B, (c) mesh C, (d) mesh D, and (e) mesh E within yz cross-section highlighted in (f).

The meshes with a smaller ribbing aspect ratio (Figures 3.11a, 3.11d, and 3.11e) have a lower normalized stress than models with a larger aspect ratio (Figures 3.11b and 3.11c). This was substantiated by investigating the stress-state of a film with a non-dimensional gap equal to that of mesh A but with a ribbing aspect ratio equal to zero (Figure 3.9), which resulted in a maximum normalized Von Mises stress of 0.008 between the rollers. From Figure 3.11, ribbed materials with a larger ribbing aspect ratio do not fully flood the gap between the rollers; rather, air exists between the top surface of the film and the top roller. The increased stiffness provided by the CNTs to the PDMS in combination with the larger ribbing amplitude with respect to the wavelength resists the lateral movement or shearing behavior required for the ribbing peaks to fill the troughs.

3.6 Ribbing Instability Model Formulation

3.6.1 Instability of ribbing microstructures

To further understand how ribbing occurs, we related the microstructures to the rolling conditions, material properties, and local stress-state obtained from the computational modeling. The ribbing aspect ratio measured in experiments and the average normalized stress in the roller gap cross-section obtained from the computational models with respect to the prescribed non-dimensional roller gap are shown in Figure 3.12.

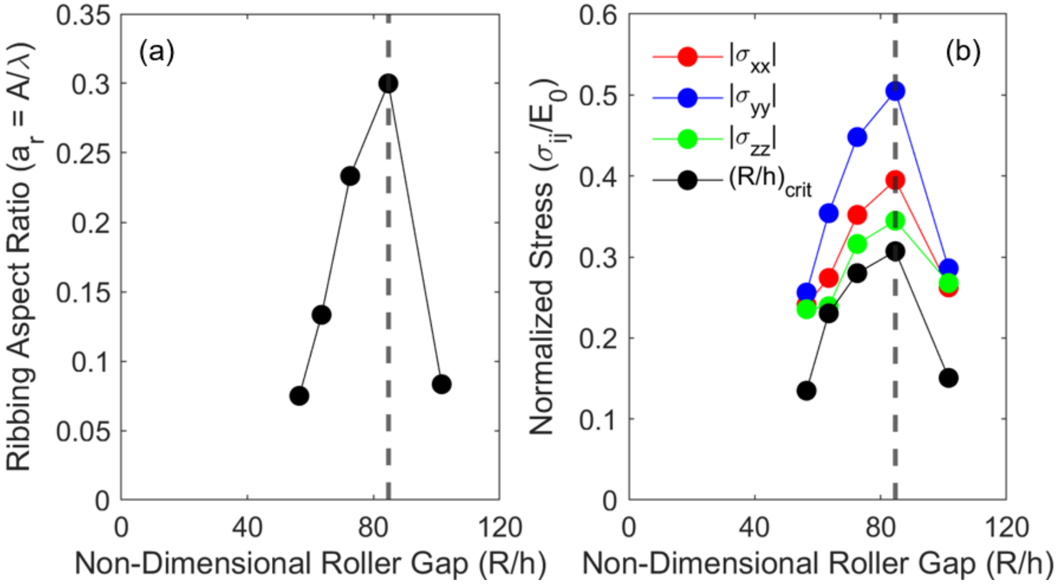

Figure 3.12. (a) Ribbing aspect ratio, a_r, with respect to the prescribed non-dimensional roller gap, R/h, obtained from experiments, (b) average normalized normal stress components, $\bar{\sigma}_{ii}/E_0$, and Von Mises stress, $\bar{\sigma}_{VM}/E_0$, predicted by finite-element models with respect to the non-dimensional roller gap.

There is a critical non-dimensional roller gap ($(R/h)_{crit}$ = 84.67, h_{crit} = 300 μm) observed in Figure 3.12 given by the dashed line for which the ribbing aspect ratio attains a maximum value. The ribbing behavior that occurs at this critical roller gap is given in Figure 3.12b. The ribbing aspect ratio that occurs at the critical non-dimensional roller gap to be the critical aspect ratio is denoted as $a_{r,crit}$, which is 0.300 for the CNT-PDMS system with 3.5 wt% CNT. We postulate then that $(R/h)_{crit}$ and $a_{r,crit}$ are dependent on the PDMS matrix and on the weight percent of the CNT. This hypothesis is consistent with [4,6], which indicate that increasing CNT content in a PDMS matrix led to smaller ribbing wavelengths. The normalized stresses exhibit a similar trend with respect to the non-dimensional roller gap as the ribbing aspect ratio (Figure 3.12b). A maximum for each of the normal stresses and the Von Mises stress was attained at $(R/h)_{crit}$. This similarity provided insight to relate the local stress-state to the aspect ratio.

The ribbing aspect ratio has a significant effect on the resulting film stress. Since the ribbing aspect ratio provides a characteristic nondimensional measure of the surface morphology of the ribbed film, it can be used as a design tool connecting the manufacturing conditions and the resulting film stress to the film texture. The average normalized Von Mises stress was obtained with respect to the ribbing aspect ratio (Figure 3.13). Five of the data points in Figure 3.13 come from the five FE meshes informed by the five experimental specimens; the sixth data point at a_r = 0 represents the non-ribbed FE prediction from Figure 3.9.

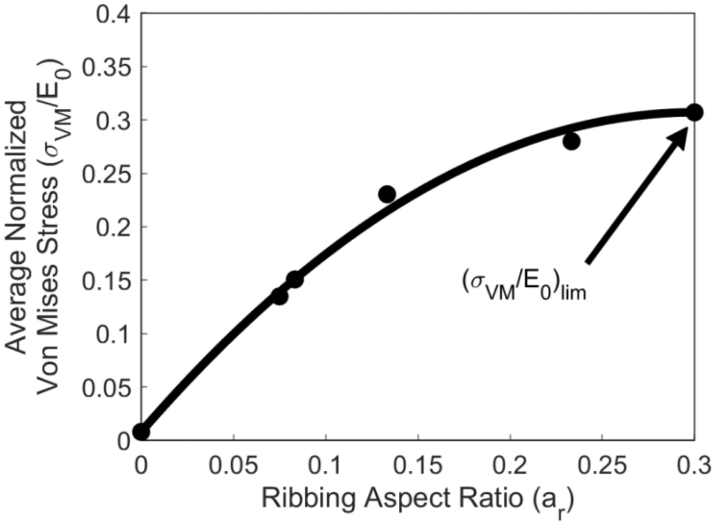

Figure 3.13. Average normalized Von Mises stress ($\bar{\sigma}_{VM}/E_0$) in gap cross-section from finite-element models with respect to ribbing aspect ratio (a_r) and maximum limiting value $(\bar{\sigma}_{VM}/E_0)_{lim}$.

The average normalized stress exhibits a quadratic behavior. Given this behavior a quadratic instability model was postulated as

$$S(a_r) = \theta_1 a_r^2 + \theta_2 a_r + \theta_3, \tag{3.2}$$

where S is the average normalized Von Mises stress as a function of ribbing aspect ratio (a_r) and the set $\{\theta_i\}$ are undetermined coefficients of the model.

The maximum limiting stress of the ribbed material denoted as $(\bar{\sigma}_{VM}/E_0)_{lim}$ is, therefore, attained at the critical aspect ratio ($a_{r,crit}$) and the minimum value ($(\bar{\sigma}_{VM}/E_0)_{min}$) is attained when the aspect ratio is zero. This minimum value was determined by setting the ribbing amplitude of the first model to zero. Thus, $\theta_3 = (\bar{\sigma}_{VM}/E_0)_{min}$ in our instability model. From our first assumption we have $S(a_{r,crit}) = (\bar{\sigma}_{VM}/E_0)_{lim}$ and $S'(a_{r,crit}) = 0$. We then have enough conditions to determine the remaining instability model coefficients, which yields

$$S(a_r) = \Delta(\bar{\sigma}_{VM}/E_0)_{ribbing}\left[-\left(\frac{a_r}{a_{r,crit}}\right)^2 + 2\left(\frac{a_r}{a_{r,crit}}\right)\right] + (\bar{\sigma}_{VM}/E_0)_{min}, \tag{3.3}$$

where $\Delta(\bar{\sigma}_{VM}/E_0)_{ribbing} = (\bar{\sigma}_{VM}/E_0)_{lim} - (\bar{\sigma}_{VM}/E_0)_{min}$.

We then assumed that the developed instability model is only valid for ribbing aspect ratios between zero and $a_{r,crit}$; the ribbed microstructure is unstable for aspect ratios above this critical value due to the CNT inclusions. Thus, Equation (3.3) applies only for $a_r \in [0, a_{r,crit}]$. Recalling that the ribbing amplitude (A) is a function only of the prescribed non-dimensional roller gap (h), as observed in Chapter 3.3, and $a_r = A/\lambda$, our ribbing instability model predicts a unique ribbing wavelength for a given ribbing instability S. The ribbing instability model in Equation (3.3) can be used to design ribbed films for multifunctional applications by determining the required surface morphology, such as a high aspect ratio for anti-icing behavior, and prescribing the roller gap based on the desired film thickness.

3.6.2 Method of Morris sensitivity analysis of the ribbing instability

Since the ribbing instability model given in Equation (3.3) was obtained from limited predictions and data, it is important to establish confidence intervals for the model parameters and to conduct a sensitivity analysis on the response. Evaluating Equation (3.3) for our CNT-PDMS system yields parameter values of θ_1 = -3.323, θ_2 = 1.994, and θ_3 = 0.008 with corresponding standard deviations of σ_{θ_1} = 1.313, σ_{θ_2} = 0.488 and σ_{θ_3} = 0.036. These standard deviations were obtained by least-squares. The ratio of each standard deviation to the parameter values indicates that there is large relative uncertainty in the first (θ_1) and third (θ_3) parameters. Thus, it is important to quantify the influence of each parameter on the total model response.

A Morris sensitivity analysis was conducted to investigate the importance of each θ_i parameter in the ribbing instability model given in Equation (3.3). The method computes the sensitivity measure (y) from a response function taken to be

$$y(\theta) = \int_0^{a_{r,crit}} S(a_r;\boldsymbol{\theta})da_r = \theta_1 \frac{a_{r,crit}^3}{3} + \theta_2 \frac{a_{r,crit}^2}{2} + \theta_3 a_{r,crit}. \tag{3.4}$$

Fifty trajectories were sampled from the parameter space with standard deviations σ_{θ_i} centered at each θ_i: $\theta_1 \in [-6.2422, -0.9903]$, $\theta_2 \in [1.1005, 3.054]$, $\theta_3 \in [-0.0683, 0.0769]$. Finite-difference quotients were computed to obtain the sensitivity results [94].

The Method of Morris provides three critical measures: the relative sensitivity of each parameter on the response (μ_i), the linearity of the parameter (σ_i), and the 95% confidence interval of the sensitivity measure ($\mu_i^{\star}$). We find for Equation (3.3) that $\theta_2 = 2\Delta(\bar{\sigma}_{VM}/E_0)_{ribbing}/a_{r,crit}$ is the most influential parameter and $\theta_3 = (\bar{\sigma}_{VM}/E_0)_{min}$ is the least influential since $\mu_2 = 0.08791$ and $\mu_3 = 0.04356$, respectively. The parameter $\theta_1 = -\ \Delta(\bar{\sigma}_{VM}/E_0)_{ribbing}/a_{r,crit}^2$ had a relative sensitivity of $\mu_1 = 0.4727$ so the magnitude of its effect on the model is between parameters θ_2 and θ_3. All three parameters are linear since $\sigma_i \approx 0$, which is expected since the instability model chosen was linear in the parameters. Since θ_2 is the most influential parameter and has the lowest standard deviation, we can be confident that the ribbing instability model in Equation (3.3) can predict the ribbing microstructure from the manufacturing conditionals accurately. The significance of these findings is that to calibrate the model for new materials the limiting stress and critical aspect ratio are the most important parameters to experimentally determine that affect the rolling instabilities.

3.7 Conclusions

A nonlinear implicit dynamic finite-element (FE) scheme was used with viscoelastic material model that was obtained by dynamic mechanical analysis and validated by two optimization schemes—a deterministic constrained optimization routine and a Bayesian metropolis algorithm—to model the symmetric forward-roll coating of high viscosity CNT-PDMS paste. The rolling conditions and film geometry were incorporated within the three-dimensional FE model to understand the local stress-state as a function of the ribbing microstructure. The computational FE models provided a detailed understanding of the thin-film ribbing microstructure that arises from viscoelasticity and manufacturing conditions, such as the roller gap.

Different CNT contents within the PDMS matrix were investigated to understand how the high-elasticity CNT filler strengthens the liquid matrix, which is related to the ribbing behavior and the rolling resistance due to surface tension-driven flattening before the paste can be cured. Dynamic mechanical analysis measurements indicate that CNT content of at least 1 weight percent (wt%) is required to stabilize the shear storage and loss moduli in the low-frequency regime, thereby ensuring that the material behaved as a solid viscoelastic paste. The rheological properties of the CNT-PDMS paste with 3.5 wt% CNT was characterized as a four-term Prony series; credible and prediction intervals provide high confidence in the material relaxation behavior in the frequency range related to the rolling rate used in the experiments and computational models.

The computational models were based on ribbed films, whose microstructural characteristics were informed by measurements obtained from scanning electron microscopy, to understand the effect of the contact from the rollers on the local stress-state of the film and on the evolution of the ribbing profile. The film thickness was obtained from experiments to be approximately 1.2 times the roller gap distance. A critical roller gap of 300 μm was predicted at which the resulting ribbing wavelength attained a minimum value of 100 μm for the 3.5 wt% CNT paste. A non-dimensional ribbing aspect ratio parameter, which is the ribbing amplitude divided by the wavelength, provided insights into the parabolic relation between the roller gap and the ribbing microstructure. FE predictions also indicated a similar relation between the local stress-state and the roller gap, which indicates that the aspect ratio and stress-state are parabolically related. A ribbing instability model was formulated that can predict the resulting ribbing aspect ratio from the computed stress-state. The method of Morris was employed to investigate the sensitivity of each parameter in the ribbing instability model on the model response. The sensitivity analysis found that the maximum ribbing stress divided by the ribbing aspect ratio is the most influential parameter and is the parameter with the lowest relative standard deviation. Thus, the sensitivity analysis validates the predictive capabilities of the ribbing instability model.

The present analysis underscores how the viscoelastic behavior of the thin-film and the separation distance between the rollers affects and controls the ribbing microstructural behavior. The predictive capabilities of the ribbing instability model can be further improved by investigating the physical origin of the critical ribbing aspect ratio by altering the weight content of the filler material and by operating the rollers at higher speeds.

CHAPTER 4: Thermomechanical Response of Ribbed Thin-Film Systems to High Strain-Rate Dynamics

Part of this chapter is published in *Macromolecular Materials and Engineering* [82]

4.1 Introduction

While in use, thin-films are subjected to a wide range of extreme loadings, including in-plane dynamic loading, out-of-plane dynamic loading, and high temperatures. It is necessary to design thin-films in such a way as to mitigate undesirable responses to these extreme loadings by controlling the material properties and thin-film morphology. A computational framework is needed to predict the relation between the viscoelastic material properties and ribbing morphology on the thermomechanical response for structured thin-films subjected to dynamic loading. The major goal of this investigation, therefore, is to evaluate the response of structured CNT-PDMS thin-film materials subjected to in-plane dynamic compressive loading conditions, and to understand and predict the thermomechanical behavior of these films to high-strain rate extreme conditions. Furthermore, design recommendations are developed to optimize thermomechanical behavior by tailoring the ribbing morphology of thin-films.

4.2 Thermo-Viscoelastic Characterization of Cured PDMS and CNT-PDMS

The material model [84] for cured PDMS was given according to Equation (2.4) with the sum of relaxation coefficients, g_i, equal to unity based on the Universal Polymer Model (UPM) [87]. The relaxation coefficients were rescaled to be less than unity for use in the 3-D FE material model because the long-term shear modulus is obtained by Equation (2.3). These time constants and associated relaxation coefficients for the 20-term Prony series are given in Table 4.1.

Table 4.1. The 20-term Prony series characterization for cured, neat PDMS with time constants, τ_i, and relaxation coefficients, g_i, based on [84] for the Universal Polymer Model (UPM) and recharacterized for use in 3-D finite element models (FEM).

Prony Number	Time Constant	Relaxation Coefficient, g_i	
i	τ_i (s)	UPM	3-D FEM
1	1.00 E-6	0.5061	0.3889
2	3.16 E-6	0.0000	0.0000
3	1.00 E-5	0.1276	0.0981
4	3.16 E-5	0.0755	0.0581
5	1.00 E-4	0.0661	0.0508
6	3.16 E-4	0.0568	0.0437
7	1.00 E-3	0.0420	0.0323
8	3.16 E-3	0.0356	0.0274
9	1.00 E-2	0.0258	0.0198
10	3.16 E-2	0.0190	0.0146
11	1.00 E-1	0.0126	0.0097
12	3.16 E-1	0.0110	0.0084
13	1.00 E+0	0.0040	0.0031
14	3.16 E+0	0.0062	0.0047
15	1.00 E+1	0.0023	0.0017
16	3.16 E+1	0.0029	0.0022
17	1.00 E+2	0.0020	0.0016
18	3.16 E+2	0.0017	0.0013
19	1.00 E+3	0.0009	0.0007
20	3.16 E+3	0.0018	0.0014

The instantaneous shear modulus, G_0, of neat PDMS was 3.62 MPa. The relaxation coefficients were scaled such that the long-term shear modulus, G_∞, was 0.84 MPa [84]. The cured PDMS relaxes to 23% of its initial stiffness within 1000 seconds, after which it has a constant shear modulus. Assuming that the PDMS is nearly incompressible ($\nu \approx 0.5$), the associated elongation modulus was approximately 10 MPa; other literature values for the elongation modulus of PDMS are closer to 1 MPa [39,77]. The material in both cases is representative of a soft polymer, compared to other such polymers as PP (1.38 GPa) [95].

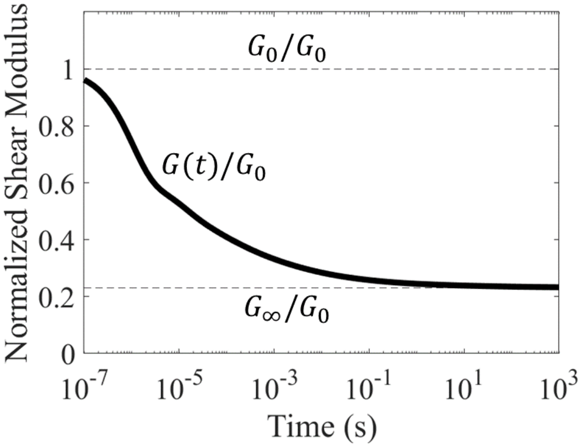

Figure 4.1. The viscoelastic material behavior of the normalized time-dependent shear modulus for cured, neat PDMS and CNT-PDMS based on [84] according to the Universal Polymer Model [87] and recharacterized for use in the 3-D finite element models (FEM). The instantaneous shear modulus, G_0, and long-term shear modulus, G_∞, were obtained from [84] for neat PDMS and were obtained by rule of mixtures for CNT-PDMS with 3.5 weight percent CNT. The relaxation behavior is described by the 20-term Prony series listed in Table 4.1.

The relaxation behavior of the neat PDMS is markedly different from the behavior of uncured PDMS (Chapter 3.2); uncured PDMS behaves closer to a liquid with no ability to resist shear deformations as its shear modulus is six orders of magnitude lower than cured PDMS and relaxes by nearly 100% after a second of relaxation time [17,96]. Thus, cured PDMS will withstand harsh environments and retain the structured shape. The same relaxation behavior can reasonably be used for CNT-PDMS.

The rule of mixtures was used to obtain the modulus of CNT-PDMS where the elongation modulus of CNT was 1 TPa. The resulting instantaneous shear modulus for CNT-PDMS with 3.5 weight percent (wt%) CNT was 12 GPa; the long-term modulus was 2.7 GPa according to the relaxation behavior described in Table 4.1 and Figure 4.1. The rule of mixtures (ROM) can overpredict the modulus for CNT-filled composites because it assumes that the reinforcing material is perfectly dispersed and binds completely to the matrix material [39,95,97–99]. By interpolating experimental measurements of CNT-PDMS with a CNT weight content between 2 wt% and 4 wt%, the approximate elongation modulus of PDMS with 3.5 wt% CNT is 5.7 MPa [45]. The error between the measured and predicted modulus from ROM is of the same order of magnitude as the error observed elsewhere [39]. This overprediction is acceptable because it provides a basis for strengthening the material by the inclusion of CNTs in the PDMS matrix.

The thermo-rheological material properties of both neat PDMS and CNT-PDMS based on Equation (2.5) were C_1 = 20, C_2 = 418.86 K, and T_0 = 298 K (Figure 4.2) [84]. The reported WLF coefficients are validated by [77] (C_1 = 23.9, C_2 = 452.8 K, and T_0 = 298.1 K), which also reports a glass transition temperature of 298.1 K. Since the reference temperature of the WLF time-temperature superposition model is the glass transition temperature of the composite, and since the temperature of the RVEs is predicted to increase in response to dynamic loading, the glassy-torubbery transition in the polymer does not need to be accounted for and the simplified thermo-rheological material model can be used as presented [87,100]. The same thermal conductivity was used for PDMS and CNT-PDMS, despite reports of the conductivity increasing slightly with increasing CNT loading [45,48].

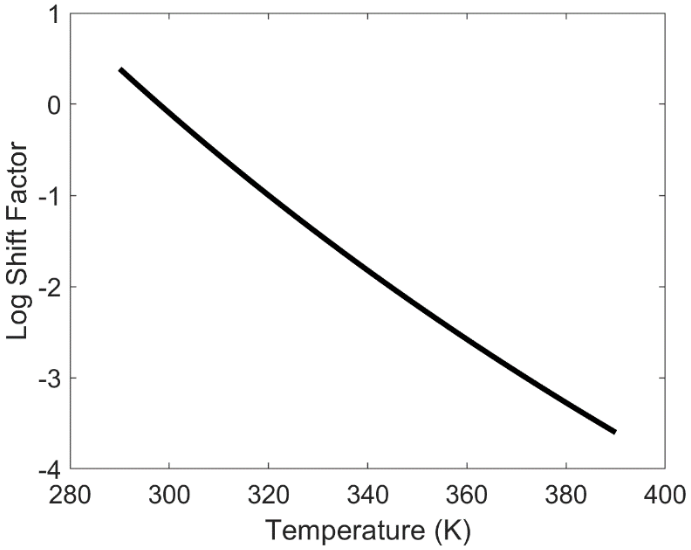

Figure 4.2. The Williams-Landel-Ferry time-temperature superposition behavior of PDMS and CNT-PDMS according to Equation (2.5) and based on coefficients from [84].

4.3 Ribbing Microstructure of Representative Volume Element Finite-Element Models

A parametric large-scale rolling study was conducted in Chapter 3.3 using PDMS with 3.5 wt% CNT to determine the effect that the roller gap has on the resulting ribbing microstructure. By adding CNT inclusions to the PDMS matrix, the viscosity of the material increased such that it retained the ribbing structure after rolling and allowed for the thermoset material to be cured. The addition of CNTs also decreased the achievable wavelength compared to neat PDMS. SEM measurements (Figure 3.6) provide detailed microstructural characteristics after the PDMS was cured.

A non-dimensional ribbing microstructural parameter, the ribbing aspect ratio (α_r), was introduced in Chapter 3.5.2 to characterize the asperity of the ribbing structure, defined as the ribbing amplitude divided by the ribbing wavelength ($\alpha_r = A/\lambda$). The feature aspect ratio is also used to characterize other such systems as wrinkled thin-films and structured topographical surfaces [8,101]. Based on Chapter 3.6, α_r can be used to understand and predict the film stress that accumulates during the rolling process. Similarly, a second non-dimensional microstructural parameter can be introduced that describes the ratio of the film thickness to the ribbing wavelength, called the ribbing length ratio ($\alpha_l = H/\lambda$).

The morphology of ribbed thin-films was obtained by SEM images from Chapter 3.3 for PDMS with 3.5 wt% CNT resulting from a parametric large-scale rolling study. The ribbing amplitude was between 0.025 mm and 0.045 mm; the ribbing wavelength was found to be between 0.09 mm and 0.62 mm; and, the thickness was between 0.30 mm to 0.54 mm. According to Chapter 3.6, the ribbing aspect ratio varies between zero (non-ribbed film) and 0.30 (maximally ribbed film). These high aspect ratio topographies are difficult to achieve [4,6,8]. Some lithography techniques can obtain a minimum wavelength of only 0.150 mm [12]; and other techniques such as the multi-step imprinting compression method in [101] was able to obtain a minimum wavelength on the order of 0.100 mm with alumina powder in a PVA matrix, but the maximum aspect ratio (defined as $\alpha_r = A/\lambda$) was 0.20. It is possible that the small particle size of the CNT, compared to other such fillers as alumina powder, combined with its high strength enables the creation of high aspect ratio structured surfaces.

A Latin Hypercube Sampling method was used to populate the microstructure of the 16 RVE models. To ensure that the randomly sampled microstructures stay within the range of acceptable ribbing aspect ratios, the microstructural bounds were adjusted slightly from the observed measurements, given in Table 4.2, which still capture the overall morphology of ribbing CNT-PDMS thin-films.

Table 4.2. The bounds of the three ribbing microstructural parameters, the ribbing amplitude (A), ribbing wavelength (λ), and film thickness (H) were obtained from scanning electron microscopy measurements for non-ribbed films (ribbing aspect ratio α_r = 0) and ribbed films with a maximum ribbing aspect ratio of 0.30. Thin-films with microstructures within these bounds represent the range of possible non-ribbed and ribbed thin-film CNT-PDMS systems.

Microstructure Parameter	Lower Bound	Upper Bound
Ribbing Amplitude (mm)	0.0000	0.0500
Ribbing Wavelength (mm)	0.1667	0.7000
Film Thickness (mm)	0.2000	0.6000

The combination of microstructural parameters for each of the 16 RVE thin-film models are displayed as a hypercube in Figure 4.3. Eight samples were obtained from the extreme values of Table 4.2; the remaining eight RVEs were sampled according to the Latin Hypercube scheme.

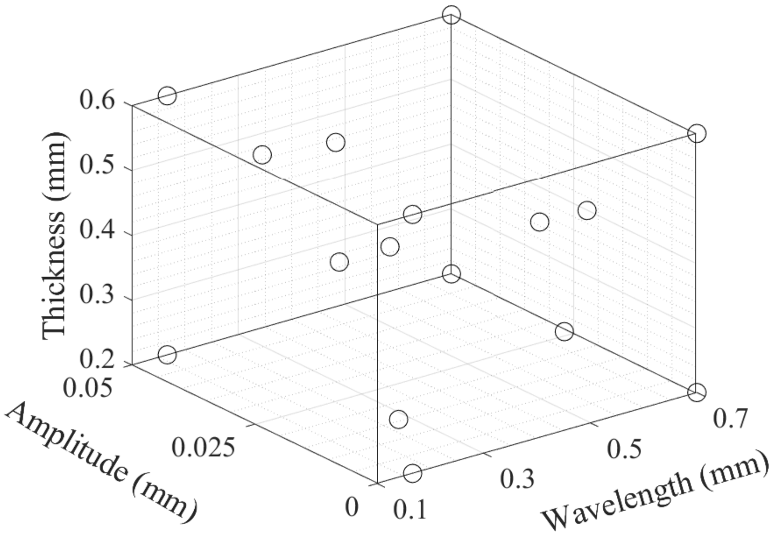

Figure 4.3. The microstructural parameters of the 16 representative volume element thin-film models were populated by Latin Hypercube Sampling including the eight corners within the bounds enforced by Table 4.2. Each circle shows the ribbing amplitude, ribbing wavelength, and film thickness of each representative volume element model in the parameter space.

4.4 Dynamic Thin-Film Representative Volume Element Models

The Prony series viscoelastic material model and the ribbing microstructural measurements were used with a nonlinear explicit dynamic computational scheme to investigate the dynamic behavior of CNT-PDMS thin-film systems subjected to in-plane compressive loading. A fully coupled thermal-stress explicit analysis was conducted to evaluate the dynamic response and account for the thermo-rheological behavior of the material and the inelastic heat generation that will result from viscoelastic energy dissipation. The mechanical solution is obtained using an explicit central-difference integration scheme with a lumped mass matrix; the heat dissipation equations are solved using a first-order explicit forward-difference time integration rule with a lumped capacitance matrix. The stable time increment for the mechanical response is $\Delta t \approx \frac{L_{min}}{c_d}$

where L_{min} is the smallest element dimension and c_d is the current dilatation wave speed defined by $c_d = \sqrt{\frac{\lambda+2\mu}{\rho}}$ where the Lame's constants are determined at the current time-step based on the mean and incremental stresses and strains. Similarly, the stable time increment for the thermal response is $\Delta t \approx \frac{L_{min}^2}{2\alpha}$ where $\alpha = \frac{k}{\rho c}$ and ρ is the density, k is the thermal conductivity, and c is the specific heat [85].

The CNT-PDMS material was assumed to have homogeneous, isotropic material properties resulting from the mixing procedure. The material was assumed to exhibit similar mechanical relaxation behavior as neat PDMS. The Prony series relaxation behavior was obtained from [84] for neat PDMS; the instantaneous modulus was obtained by rule of mixtures and a constant Poisson ratio, ν, of 0.48 was used. The WLF coefficients, C_1, C_2, and T_0, were also obtained from [84] to describe the time-temperature superposition according to Equation (2.5), with a density of ρ = 989.5 kg·m^3, thermal conductivity of 0.15 W·(m·K)$^{-1}$, and specific heat of 1460 J·(kg·K)$^{-1}$.

Three microstructural parameters were used to gain further fundamental understanding of how the microstructure evolved due to the three-dimensional dynamic loading conditions. These were the ribbing amplitude, ribbing wavelength, and film thickness. To understand the relation between the microstructure and the thermomechanical response to dynamic loading, a population of 16 RVE thin-film models with varying ribbing microstructures informed by experimental observations was introduced. The dynamic response of each RVE subjected to in-plane compressive loading for both neat PDMS and CNT-PDMS material properties were investigated to also understand how the addition of CNT inclusions in the PDMS matrix influences the thermomechanical behavior.

2,400 three-dimensional 8-node linear brick elements with full integration were used based on a convergence analysis to model the thermomechanical response of the thin-film. Five sinusoidal ribbing periods as a function of the film width were modeled for each RVE with the same mesh structure: four elements per wavelength and six elements tall. Each RVE was subjected to an in-plane dynamic compressive load in the direction of the ribbing structure (parallel load) and in the other in-plane direction (transverse load). Symmetry boundary conditions were applied to the remaining in-plane faces. The bottom surface was simply supported and the top surface was free. An initial temperature of 298 K was prescribed on all nodes. The mesh and prescribed boundary conditions of one RVE is shown in Figure 4.4.

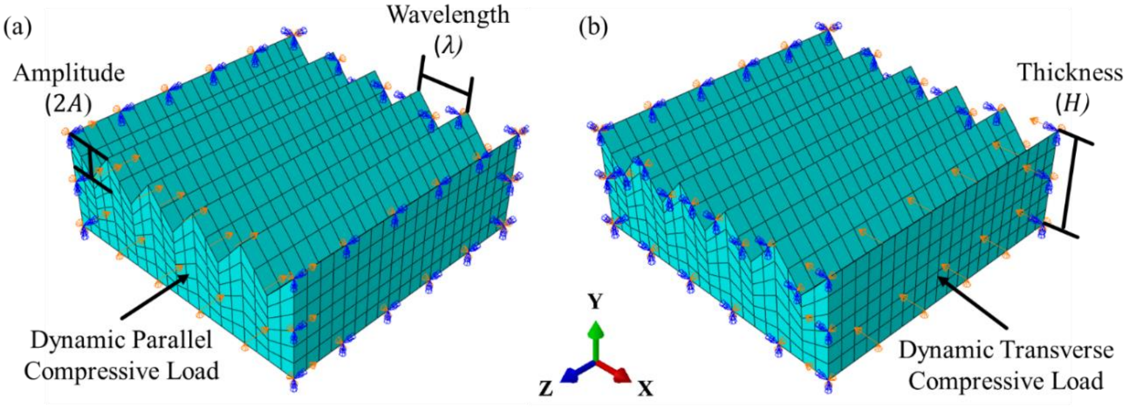

Figure 4.4. A representative volume element thin-film model subjected to a dynamic compressive load (a) parallel to the ribbing direction and (b) transverse to the ribbing direction. Each thin-film model has a prescribed ribbing amplitude (A), ribbing wavelength (λ), and film thickness (H) specified from the 16 microstructural combinations resulting from the Latin Hypercube Sampling routine. The bottom surface was simply supported, a dynamic compressive load was applied to one in-plane face, and symmetry boundary conditions were applied to the remaining in-plane faces.

Based on the material properties and mesh characteristics, the approximate stable time step for the mechanical and thermal solutions were obtained. For example, the stable time increment for neat PDMS is 10^{-7} seconds for the purely mechanical load and 10^{-3} seconds for the purely thermal load. Three strain rates were modeled for each of the loading directions: 10^{2} s^{-1}, 10^{3} s^{-1}, and 10^{4} s^{-1}. The stable time-step was 10^{-7} s for 10^{2} s^{-1}, 10^{-8} s for 10^{3} s^{-1}, and 10^{-9} for 10^{4} s^{-1}. The ramp times were $5 \cdot 10^{-4}$, $5 \cdot 10^{-5}$, and $5 \cdot 10^{-6}$ s. The total time that the dynamic behavior of each RVE was ten times the ramp time.

4.5 Finite-Element Modeling Results

The proposed ribbing microstructure and FE computational approach were used to investigate the dynamic response of ribbed homogeneous PDMS and heterogeneous CNT-PDMS thin-films to compressive loads at various strain rates. The material model of the cured and neat PDMS and CNT-PDMS was obtained from [84] and adapted for use in the 3-D FE models. The population of 16 RVEs was used to predict the thermomechanical behavioral differences resulting from the microstructure, material properties, and nominal strain rates. Hypersurfaces of the thermomechanical response were developed to visualize the effect that the ribbing microstructure had for each nominal strain rate. A validated regression model of the characteristic response was also obtained from the hypersurfaces to predict and optimize the microstructure for design purposes when subjected to extreme high strain-rate conditions.

4.5.1 The dynamic thermomechanical behavior of ribbed thin-film systems

To isolate the effect that strain rates and material composition have on the thermomechanical response of the thin-film, the second RVE thin-film model (H = 0.479 mm, A = 0.046 mm, λ = 0.444 mm) subjected to a compressive strain in the parallel direction at three nominal strain rates was evaluated. The displacement in the loading direction of the second RVE for both neat PDMS and CNT-PDMS material properties was obtained in Figure 4.5.

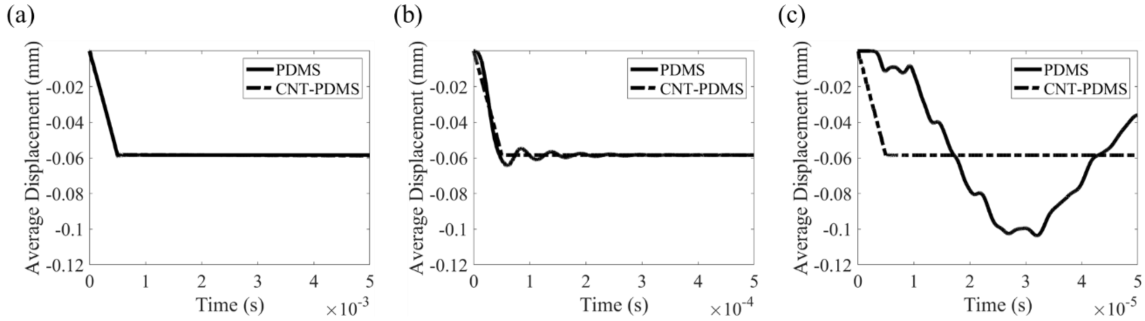

Figure 4.5. The average z-displacement of the line path within the thin-film model with ribbing amplitude of 0.046 mm, ribbing wavelength of 0.444 mm, and film thickness of 0.479 mm subjected to parallel loading (in the z-direction) with a nominal applied strain rate of (a) 10^2 s^{-1}, (b) 10^3 s^{-1}, and (c) 10^4 s^{-1}.

The film subjected to the slowest nominal strain rate (10^2 s^{-1}) linearly approaches a constant displacement with negligible vibrations through the film. In the second case, the RVE is loaded at a nominal strain rate of 10^3 s^{-1}: the neat PDMS thin-film overshoots the steady-state displacement from Figure 4.5a before reflecting and attenuating from the viscoelastic dissipation; the CNT-PDMS thin-film exhibits the same behavior as in Figure 4.5a. Lastly, the PDMS film subjected to a nominal strain of 10^4 s^{-1} overshot the steady-state displacement by nearly two times before reflection. The observed time in Figure 4.5c was not long enough for the wave to reflect and show the viscoelastic relaxation, which would occur at the same rate as that in Figure 4.5b. The oscillatory behavior of the neat PDMS film subjected to a dynamic mechanical load resembles that of [102], which showed a similar dynamic displacement response in thermo-viscoelastic materials when subjected to thermal shock, another extreme environment.

Based on the displacements in Figure 4.5 resulting from a parallel in-plane dynamic load, increasing the modulus of the ribbed thin-film stabilizes the film. This is apparent when considering the elastic wave speed ($c = \sqrt{E/\rho}$) of the two materials, which provides an approximate measure of the stress transmission speed through the viscoelastic medium. Using the instantaneous elongation modulus, the elastic wave speed of neat PDMS and CNT-PDMS is approximately c_{PDMS} = 100 $m \cdot s^{-1}$ and $c_{CNT-PDMS}$ = 6000 $m \cdot s^{-1}$. Increasing the modulus, as in the case for CNT-PDMS, allows for stress waves to propagate through the thin-film at each time-step rather than accumulating. The wave speed in neat PDMS, however, is an order of magnitude lower than that of CNT-PDMS, so the thin-film subjected to the higher strain rates have a more complex dynamic response from the intersecting stress waves. Based on the difference between the moduli obtained from ROM and experimentally from Chapter 4.2, the modulus of CNT-PDMS is about three orders of magnitude larger than the experimental values. Adjusting for this would lower the wave speed to approximately $c_{CNT-PDMS}$ = 200 $m \cdot s^{-1}$, so minimal dynamic effects would still be seen for the highest nominal strain rate.

Each of the six stress components were also obtained from line paths through the center of the mesh in the second RVE thin-film model for neat PDMS to better understand the dynamic nature of the reflecting viscoelastic wave propagation (Figure 4.6). The time in Figure 4.6 was normalized by the total model time for easier visual comparison between the three nominal strain rates.

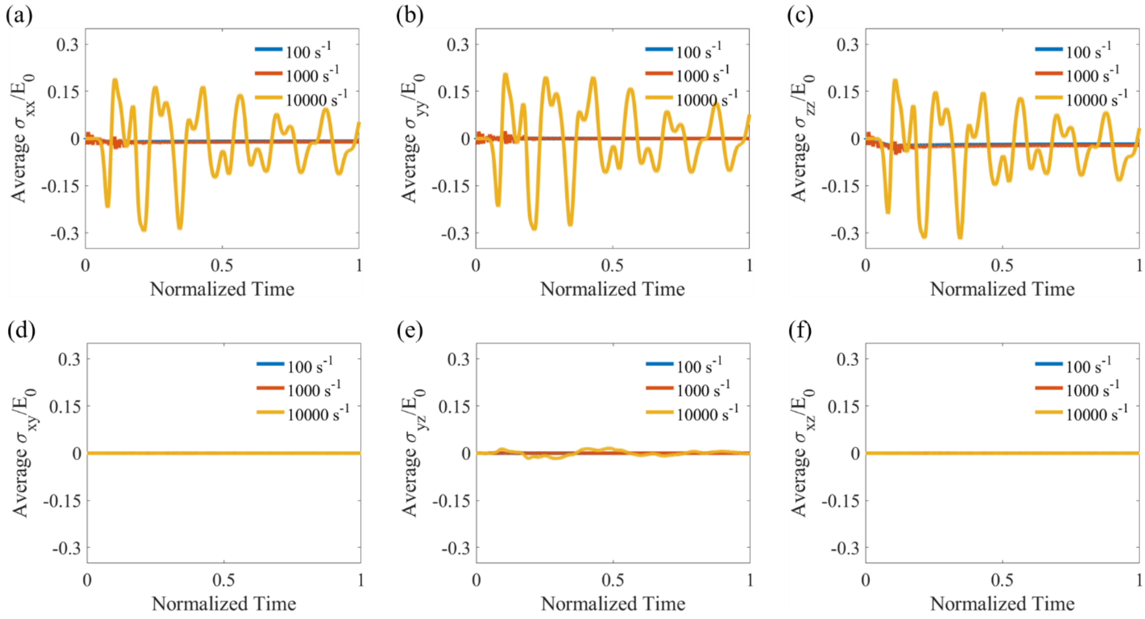

Figure 4.6. The average normal stress in the (a) x-direction, (b) y-direction, and (c) z-direction, and the average shear stress in the (d) xy-direction, (e) yz-direction, and (f) xz-direction, all normalized by the instantaneous elongation modulus of the cured, neat PDMS, E_0, were obtained through the center path of the representative volume element model with a ribbing amplitude of 0.046 mm, ribbing wavelength of 0.444 mm, and film thickness of 0.479 mm subjected to three strain rates in the parallel ribbing direction (the z-direction).

As with the displacements, increasing the strain rate increases the stress response and results in viscoelastic waves. Since the compressive loading is in the direction parallel to the ribbing profile (the z-direction), the stresses in Figure 4.6c are slightly larger than in Figures 4.6a and 4.6b. The three normal stresses (Figures 4.6a–4.6c) are significantly larger than the shear stresses (Figures 4.6d–4.6f). Thus, the response is governed entirely by the normal stresses. The large magnitude of the normal stresses when subjected to only 5% nominal strain at a 10^4 s^{-1} nominal strain rate is an extreme condition. Since the strain remains below 5%, it is unlikely that additional instability modes arise, as with linearly periodic wrinkled thin-film systems [8,11,34].

To have a better characteristic measure of the thin-film response, the Von Mises stress normalized by the elongation modulus of the materials were obtained (Figure 4.7). The time was normalized by the total time.

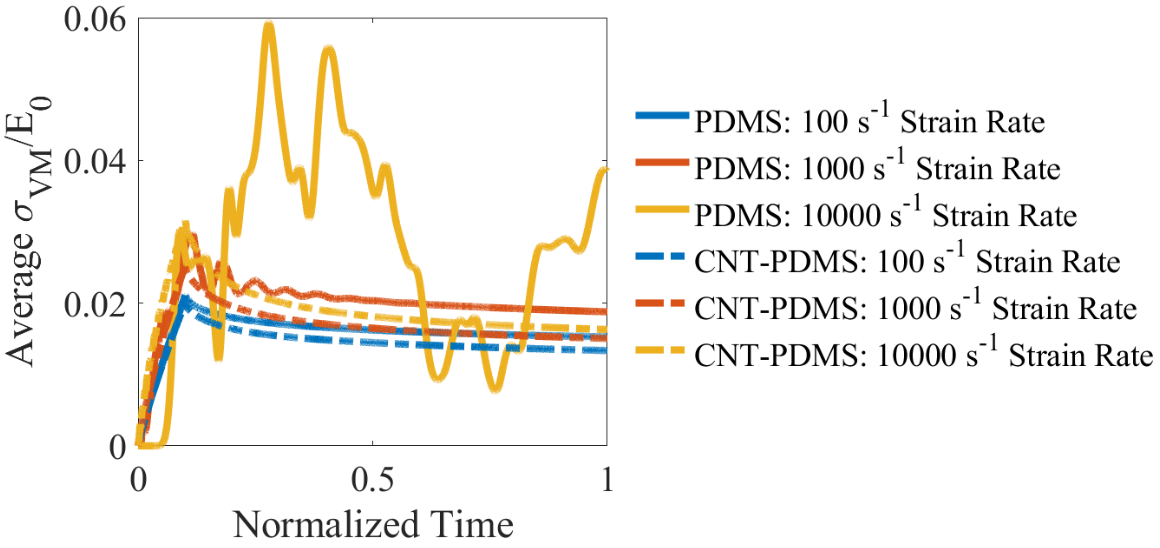

Figure 4.7. The average Von Mises stress normalized by the instantaneous elongation modulus of the material, E_0, obtained from the line path within the thin-film model with ribbing amplitude of 0.046 mm, ribbing wavelength of 0.444 mm, and film thickness of 0.479 mm subjected to parallel loading. The solid and dashed lines show the behavior of neat PDMS and CNT-PDMS, respectively. The time was normalized by the total time of each model for easier visual comparison.

The behavior of the neat PDMS thin-film model subjected to the three nominal strain rates is given by the solid lines in Figure 4.7. At a nominal strain of 10^2 s^{-1}, stress relaxation occurs immediately upon deformation and continues for the whole duration. After the RVE is loaded to the target nominal strain, the material relaxes smoothly in proportion to the long-term viscoelastic behavior. The RVE in the 10^3 s^{-1} case experiences a slight overshoot in the average stress through the line path. Much like the displacements, the stress waves reflect several times as the viscoelastic material behavior dampens the response. Finally, the time delay between the displacements applied on the positive z-face and the response in the interior line path for the 10^4 s^{-1} strain case shows the time that it takes for the viscoelastic stress waves to travel through the RVE. The interacting 3-D stress wave reflections combine to triple the stress from the 10^2 s^{-1} nominal strain rate case. The modeled time of $5 \cdot 10^{-5}$ seconds was not long enough to observe the stress wave relaxation based on the Prony series time constants and associated relaxation coefficients (Table 4.1).

Since the modulus of the thin-film structure increased by the addition of CNT inclusions, the average normalized stress response of the CNT-PDMS given by the dashed lines in Figure 4.7 is characteristic of a typical viscoelastic relaxation curve. Since the viscoelastic material model is rate dependent, the faster loading rate allows for less relaxation to occur than the slower rate; thus, the maximum stress in the CNT-PDMS thin-films increases with respect to increasing strain rate whereas an elastic material model would be insensitive to changes in the rate of loading.

Lastly, the thermal effects of the second RVE subjected to various strain rates for the two materials was obtained (Figure 4.8). The initial temperature of the thin-film was 298 K; inelastic heat generation due to viscoelastic energy dissipation was the only mechanism by which the temperature of the thin-film could increase.

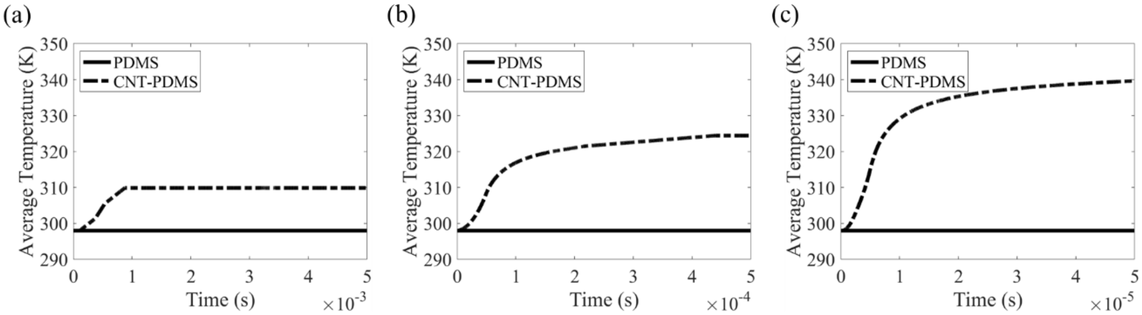

Figure 4.8. The average temperature of the line path within the thin-film model with ribbing amplitude of 0.046 mm, ribbing wavelength of 0.444 mm, and film thickness of 0.479 mm subjected to parallel loading with a nominal applied strain rate of (a) 10^2 s^{-1}, (b) 10^3 s^{-1}, and (c) 10^4 s^{-1}.

The heat generation is a function of both the material modulus and the applied strain rates. It is evident in Figure 4.8 that the modulus of neat PDMS was too low for any temperature increase to occur. In Figure 4.8a, the CNT-PDMS temperature increases by 12 K during the loading phase for the 10^2 s^{-1} nominal strain rate, after which the temperature remains constant. As the nominal strain rate increases, so does the increase in temperature. The 10^3 s^{-1} and 10^4 s^{-1} nominal strain rate cases also increase in temperature after the initial loading ramp due to the viscoelastic relaxation. The predicted temperature increase is much higher than it would be if a more experimentally-based (rather than ROM-based) modulus were used. Hence, the temperature predictions give an upper bound of the temperature increase during extreme high strain-rate loading.

4.5.2 The Von Mises stress hypersurface visualization for ribbed thin-films

To better understand and predict the relationship between the microstructure and the thermomechanical response, we developed hypersurfaces of the response behavior with respect to the ribbing microstructure at each nominal strain rate. The thermal responses for the remaining 15 microstructures were similar to Figure 4.8, and the temperature increase was not large enough to warrant concern. Instead, we focused on the mechanical response by constructing hypersurfaces of the Von Mises stress. Since we wanted to understand the behavior for extreme conditions, we obtained the maximum normalized Von Mises stress. The hypersurfaces of both PDMS and CNT-PDMS thin-films are shown in Figure 4.9 for a nominal strain rate of 10^3 s^{-1}. Since there are three microstructural parameters that characterize the thin-film RVE—i.e., the ribbing wavelength, ribbing amplitude, and film thickness—at least two 3-D surfaces are needed to fully visualize and understand the relation between the microstructure and the resulting thermomechanical response to the dynamic loading. Instead, the two non-dimensional ribbing microstructural parameters were used: the ribbing aspect and length ratios ($\alpha_r = A/\lambda$ and $\alpha_l = H/\lambda$).

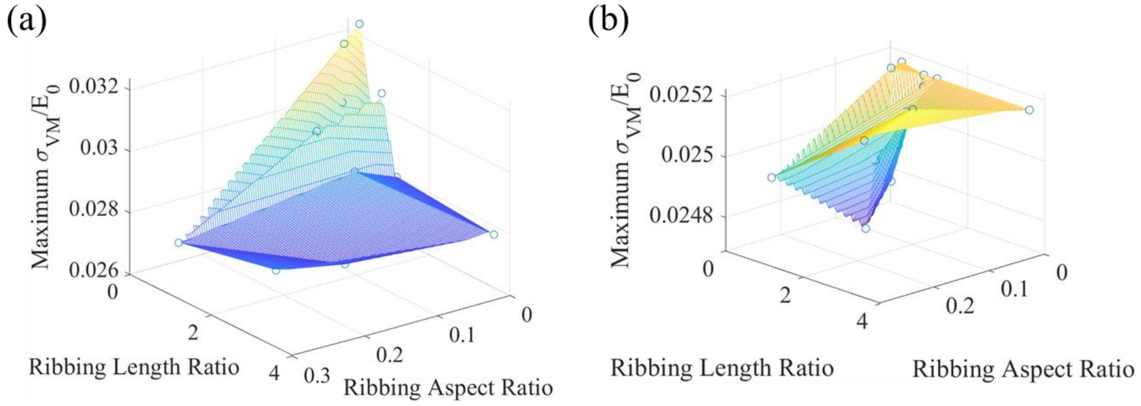

Figure 4.9. The maximum Von Mises stress normalized by the instantaneous elongation modulus, E_0, for (a) neat PDMS and (b) CNT-PDMS obtained from each of the 16 representative volume element thin-film models subjected to a nominal strain rate of 10^3 s^{-1}. The hypersurfaces were constructed by linearly interpolating between the 16 data points obtained from FE.

In Figure 4.9a, the stress in the neat PDMS thin-films attained the maximum value at small ribbing aspect ratios and length ratios (i.e. large wavelengths, small amplitudes, thin films). There is a large region in Figure 4.9a where the film stress was a minimum, which occurred at larger ribbing aspect and length ratios. It is in this region that thin-films should be designed to prevent damage when subjected to high strain rate dynamic events. CNT-PDMS thin-films subjected to a 10^3 s^{-1} nominal strain rate (Figure 4.9b) also show a decrease in the maximum normalized stress as a function of the ribbing aspect ratio. The maximum stress for all microstructural combinations was lower for CNT-PDMS thin-films than for neat PDMS thin-films, likely due to the reduced dynamic effects.

4.6 Ribbing Microstructure Optimization and Uncertainty Quantification

After determining the relation between the non-dimensional microstructural parameters and the thin-film response, we wanted to understand how thin-film systems can withstand high strain-rate events. A polynomial regression model was chosen to characterize the response of the thin-film with non-dimensional microstructural parameters α_l and α_r subjected to a given nominal strain rate, $\dot{\epsilon}_0$, as

$$\begin{aligned} \frac{\sigma_{VM}(\alpha_r, \alpha_l, \dot{\epsilon}_0; \boldsymbol{\theta})}{E_0} &= \theta_1 + \theta_2\alpha_r + \theta_3\alpha_l + \theta_4\alpha_r^2 + \theta_5\alpha_r\alpha_l + \theta_6\alpha_l^2 \\ &+\theta_7\dot{\epsilon}_0 + \theta_8\alpha_r\dot{\epsilon}_0 + \theta_9\alpha_l\dot{\epsilon}_0 + \theta_{10}\dot{\epsilon}_0^2 \, , \end{aligned} \tag{4.1}$$

where θ_i is the i-th regression coefficient. The regression model was trained with 75% of the RVE results from all three strain rates to predict the maximum normalized Von Mises stress for a given ribbing microstructure and nominal strain rate. The remaining 25% was withheld for model testing to ensure it was not overfit. The L2-norm residual of the training data of the regression model was 0.03390 for neat PDMS and 0.00080 for CNT-PDMS; the respective residuals of the testing data were 0.02011 and 0.00087. Table 4.3 shows the coefficients of the ten-term regression model for each thin-film material.

Table 4.3. The coefficients from the regression model obtained by linear least squares to predict the maximum normalized Von Mises stress in ribbed thin-film systems with a given ribbing microstructure and nominal compressive strain-rate.

i	θ_i	
	PDMS	CNT-PDMS
1	3.42E-2	1.94E-2
2	2.55E-3	-2.00E-3
3	-2.07E-2	6.87E-5
4	-2.39E-2	6.14E-6
5	6.18E-3	6.13E-3
6	4.72E-3	1.30E-4
7	1.01E-5	-5.68E-6
8	-3.39E-6	-1.13E-8
9	-7.60E-7	-7.01E-9
10	4.90E-10	-4.91E-10

The regression model provided another method to understand how to control the topography of structured surfaces compared to the empirical relations for wrinkling given by [8,35]. The coefficients from Table 4.3 indicate that all three parameters—the non-dimensional microstructural parameters and the nominal strain rate—will have a significant effect on the maximum normalized Von Mises Stress for neat PDMS thin-films. The regression coefficients for CNT-PDMS, however, are lower for all parameters except the $\dot{\epsilon}^2$-term, which suggests that the mechanical response of the higher modulus material is more dependent on the nominal strain rate than the ribbing morphology. The hypersurface of the thin-film response from a dynamic compressive load at a specified nominal strain rate can be visualized with respect to the microstructure. Figure 4.10 shows the reconstructed surfaces and the RVE predictions for both materials at the three tested strain rates: 10^2 s^{-1}, 10^3 s^{-1}, and 10^4 s^{-1}.

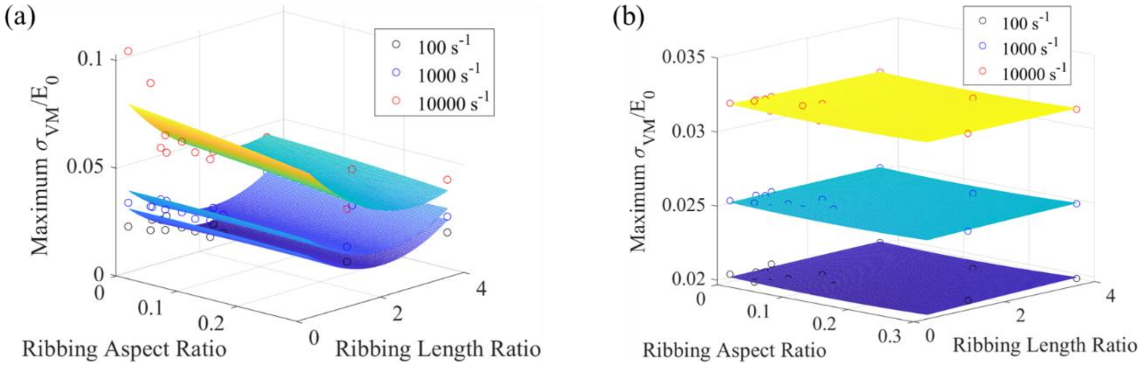

Figure 4.10. The maximum Von Mises stress normalized by the instantaneous elongation modulus of the material, E_0, for (a) neat PDMS and (b) CNT-PDMS obtained from of each of the 16 representative volume element thin-film models for all three strain rates. The hypersurfaces were constructed for each nominal applied strain rate by the regression model obtained in Equation (4.1).

The three response surfaces for neat PDMS in Figure 4.10a were consistent with the RVE predictions where increasing the nominal strain rate increases the predicted stress in the thin-film. They also show that there is a more significant increase in the normalized Von Mises stress for thin-films with small ribbing aspect and length ratios. The sensitivity to film thickness is also consistent with experimental observations [80,81] and computational predictions [13] pertaining to the high strain rate response of materials exhibiting inelastic behavior. At the higher strain rates, the thin-film was closer to the material's strength. Hence, based on our modeling predictions, thick

PDMS thin-films with large ribbing amplitudes and small ribbing wavelengths are ideal for damage prevention in high strain rate dynamic events.

The response surface for CNT-PDMS (Figure 4.10b) shows almost no variation in the mechanical response with respect to the microstructure; rather, the response is governed almost entirely by the applied nominal strain rate as indicated by the regression model coefficients from Table 4.3. The magnitude of the maximum normalized Von Mises stress of neat PDMS (Figure 4.10a) predicted by RVE models is three times larger than that of PDMS with 3.5 wt% CNT (Figure 4.10b). Since the predicted stress of the CNT-PDMS thin-film RVE models is independent of the microstructure, the mechanical behavior of such CNT-PDMS thin films as those fabricated and measured to obtain the microstructural parameter bounds (Table 4.2) are also expected to be independent of the microstructure. Thus, the manufacturing of ribbed CNT-PDMS thin-films can be tailored to exhibit favorable surface behaviors due to high strain-rate behavior.

Since the regression model is representative of the behavior of the hypersurfaces created by the population of RVEs sampled by the Latin Hypercube method, it can be used to optimize the microstructure and predict the thin-film response to dynamic loading for various compressive loadings. A constrained interior-point optimization routine was used and evaluated for nominal strain rates between 10^0 and 10^4 s^{-1}. For each strain rate, the minimax normalized Von Mises stress was obtained with the corresponding microstructure (Figure 4.11). The optimization procedure was twice repeated for each material with a constant ribbing aspect ratio of 0 (non-ribbed film) and of 0.30 (maximally ribbed film) to understand how the two film types behave.

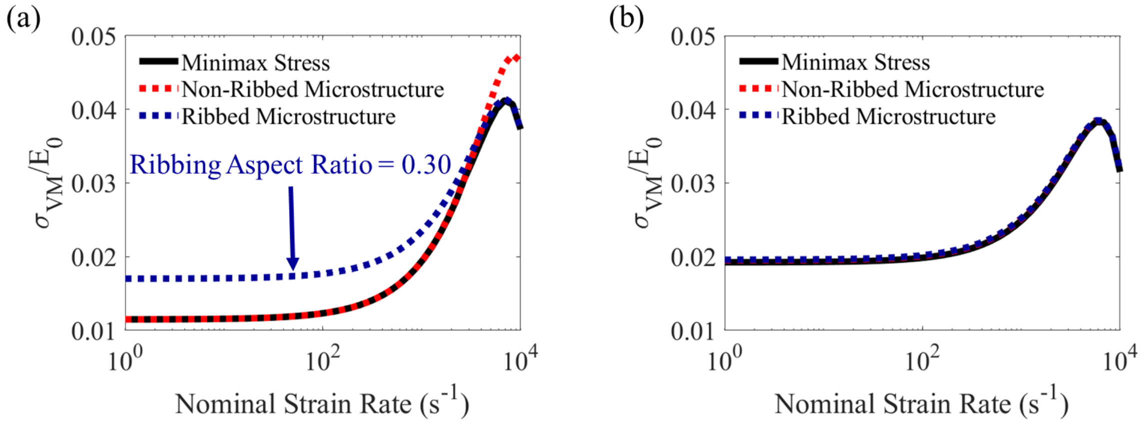

Figure 4.11. The regression model was optimized to obtain the microstructure yielding the lowest maximum stress (minimax stress) for (a) neat PDMS and (b) CNT-PDMS. The solid black curve gives the minimax stress of all microstructural combinations for nominal strain rates between 10^0 s^{-1} and 10^4 s^{-1}. The dashed red and blue curves give the minimax stress for a non-ribbed film ($\alpha_r = 0$) and a maximally ribbed film ($\alpha_r = 0.30$), respectively.

Below strain rates of 10^2 s^{-1}, the response of the neat PDMS thin-film approaches quasi-static behavior, based on the regression model predictions in Figure 4.11a. In this regime, ribbed thin-films have a maximum stress 1.5 times larger than a non-ribbed film. Above the quasi-static strain rate, the maximum stress in the ribbed and non-ribbed films increased. After a nominal strain rate of 1200 s^{-1} (Figure 4.11a), a neat PDMS ribbed film outperforms the non-ribbed film and attained the minimax value. Higher strain rate regimes are critical for design considerations because the predicted stress increased as the strain rate increases [79,81]. Given that the nominal strain was only 5% in these RVE models, all the thin-films are still far from failure since they are in the linear viscoelastic regime; but for larger nominal strains, as the predictions indicate, failure would be most likely to occur in a non-ribbed film than in a ribbed film.

In contrast, the behavior of CNT-PDMS is insensitive to changes in microstructure. Based on the minimax stress of CNT-PDMS and PDMS systems (solid black line in Figures 4.11a and 4.11b), there is little difference in the optimal performance of neat PDMS and CNT-PDMS. The advantage that CNT-PDMS has over neat PDMS is that this minimax value is attainable for any ribbing microstructure, while it is only achieved for specific microstructures in PDMS. Thus, the design of ribbed CNT-PDMS thin-films can be focused on maximizing other favorable surface behaviors, such as drag reduction, superhydrophobicity, and antifouling.

4.7 Conclusions

A nonlinear explicit dynamic FE scheme was used with a viscoelastic material model subjected to compressive high strain rates and inelastic heat generation to understand and predict the thermomechanical response of ribbed thin-film structures manufactured by large-scale rolling. The shear and elongation moduli of the CNT-PDMS were determined by the rule of mixtures. The dynamic response of neat PDMS was also modeled, based on a Prony series representation, to understand how the high strength CNT inclusions affect the thermomechanical response. The RVE models of the ribbed thin-films were subjected to dynamic nominal strain rates in both the transverse and parallel ribbing directions, with strain rates as high as 10^4 s^{-1}. Latin Hypercube Sampling of the microstructural parameters, as informed from experimental observations and measurements, provided physically realistic microstructurally-based RVEs.

For the CNT-PDMS ribbed thin-films, the thermomechanical response is directly related to the effects of the nominal strain rate. At the lower strain rate of 10^2 s^{-1}, the temperature of the CNT-PDMS thin-films increases by only 12 K. At the higher strain rate of 10^4 s^{-1}, the temperature increased by approximately 40 K. For the mechanical behavior, as the nominal strain rate increases from 10^2 s^{-1} to 10^4 s^{-1}, the maximum values of the Von Mises stress almost increases by a factor of two. The CNT-PDMS thin-film structures rapidly attained steady-state behavior after the initial viscoelastic relaxation. The mechanical response of neat PDMS, in contrast, is highly dependent on both the ribbing microstructure and the nominal strain rate. There was a transition region at a nominal applied strain rate of 1200 s^{-1} where the wave speed of the material is lower than the nominal loading velocity due to wave interactions resulting in a significant increase in stress. The non-ribbed films have lower maximum stresses for nominal strain rates lower than 1200 s^{-1}, but highly ribbed films are advantageous for strain rates higher than 1200 s^{-1} because they impede the interacting stress waves. There is no significant temperature increase in neat PDMS thin-films for the modeled strain rates because the modulus is too low for sufficient heat to be generated, regardless of the ribbing microstructure. By strengthening the material with CNTs, there were reductions in stress wave interactions due to the different material constituents, which lowers the resulting film stress but increases the film temperature for all ribbing morphologies.

An interior-point optimization routine was based on a regression model trained from the FE predictions to design ribbed materials for multifunctional applications. The model validates that CNT inclusions can be used to mitigate damage in thin-film materials subjected to dynamic compressive loadings by resulting in lower stresses. The ribbing morphology can, therefore, be used to understand and control surface behavior, such as superhydrophobicity, drag reduction, or antifouling, without compromising the desired mechanical behavior of the film.

CHAPTER 5: Large-Strain Behavior of PDMS and CNT-PDMS

Part of this chapter is published in *Composites Part A: Applied Science and Manufacturing* [83]

5.1 Introduction

It is necessary to know the large-strain behavior of thin PDMS and CNT-PDMS materials to better design damage-resistant structured thin-film systems. The challenge, however, is to understand how best to represent and characterize the global large-strain mechanical behavior of the material while accounting for the rate- or time-dependent effects and the interaction of CNTs in PDMS for various CNT weight fractions. Various CNT-PDMS compositions were characterized experimentally to relate the heterogeneous morphology to the large-strain behavior and understand how the multi-phase material behavior can be physically represented. Uniaxial mechanical testing was conducted until failure for thin non-ribbed PDMS and CNT-PDMS samples with CNT loadings between 1 weight percent (wt%) and 10 wt%. Scanning electron microscopy (SEM) images of the resulting fracture surfaces were obtained to relate the agglomeration, distribution, and alignment of CNTs in PDMS to the ultimate strain, ultimate strength, and global stress-strain behavior. The SEM results also provide insights into how the PDMS and CNT phases interact, and how it is affected by the different weight percentages of the CNT distributions. Finally, a Yeoh hyperelastic and a Yeoh-Prony hyper-viscoelastic material model was optimized from the uniaxial testing data for each CNT-PDMS composition to determine how best to model the multi-phase, heterogeneous material.

5.2 Large-Strain Uniaxial Mechanical Testing of PDMS and CNT-PDMS

5.2.1 Uniaxial testing procedure for thin polymer-composite samples

Uniaxial tensile testing was conducted on PDMS and CNT-PDMS samples according to ASTM D638-22. Four CNT loadings were tested: neat PDMS, 1 wt% CNT, 3.5 wt% CNT, and 10 wt% CNT. The samples were prepared by mixing the Sylgard 184 silicone elastomer with a 10:1 hardener mixing ratio and the specified weight percent of Nanophite medium-walled CNTs with diameters between 7-12 nm and lengths that varied between 100-200 μm. in a universal planetary mixer to ensure adequate mixing. A three-roll milling machine was also used to disperse CNTs in the PDMS. Aluminum molds were manufactured with dimensions following the ASTM D638-22 Type IV standard: each specimen had a nominal gauge length of 25 mm, gauge width of 6 mm, and thickness of 1.5 mm. The uncured, mixed CNT-PDMS paste was then poured into the molds. For the pure PDMS specimens, the material was first degassed in a vacuum chamber for 30 minutes and was allowed to cure without the top plate of the mold to avoid bubble generation. For the remaining CNT-PDMS specimens, the mold was closed, and the material was allowed to cure for 60 minutes at 125°C. Five specimens were made for each CNT loading for a total of twenty specimens.

An Instron 68SC-05 single column table universal testing machine was used to conduct the uniaxial tensile testing of the thin polymer samples (Figure 5.1). Each specimen was clamped by standard serrated grips to prevent slippage during testing and then subjected to an increasing tension load at a constant loading rate of 5 mm/min until failure (Figure 5.1b). The corresponding nominal strain-rate of the uniaxial testing is 0.0033 s^{-1} based on the sample dimensions. The engineering strain and stress were obtained for each sample.

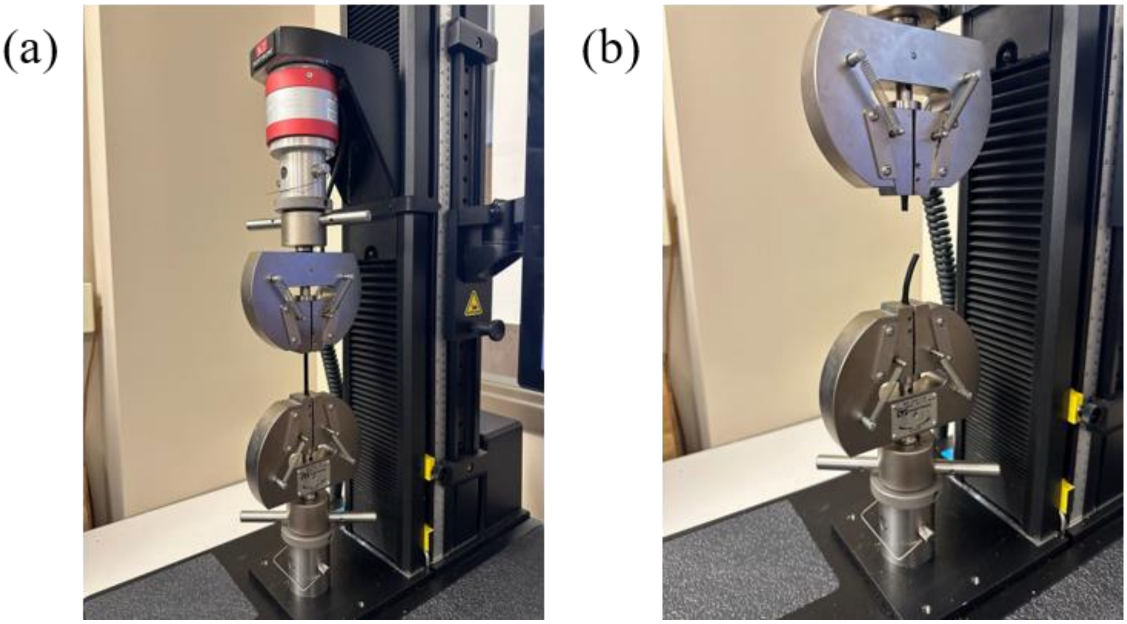

Figure 5.1. Instron 68SC-05 single column table universal testing machine with CNT-PDMS sample loaded in the clamps (a) before testing and (b) after failure.

5.2.2 Uniaxial testing results for thin PDMS and CNT-PDMS samples

Uniaxial tensile testing specimens of each material composition were fabricated to understand how increasing the CNT content affects the mechanical behavior of non-ribbed CNT-PDMS thin-film systems. Each specimen was tested in uniaxial tension to obtain the global stress-strain behavior to failure. Figure 5.2 shows one sample of each composition after testing.

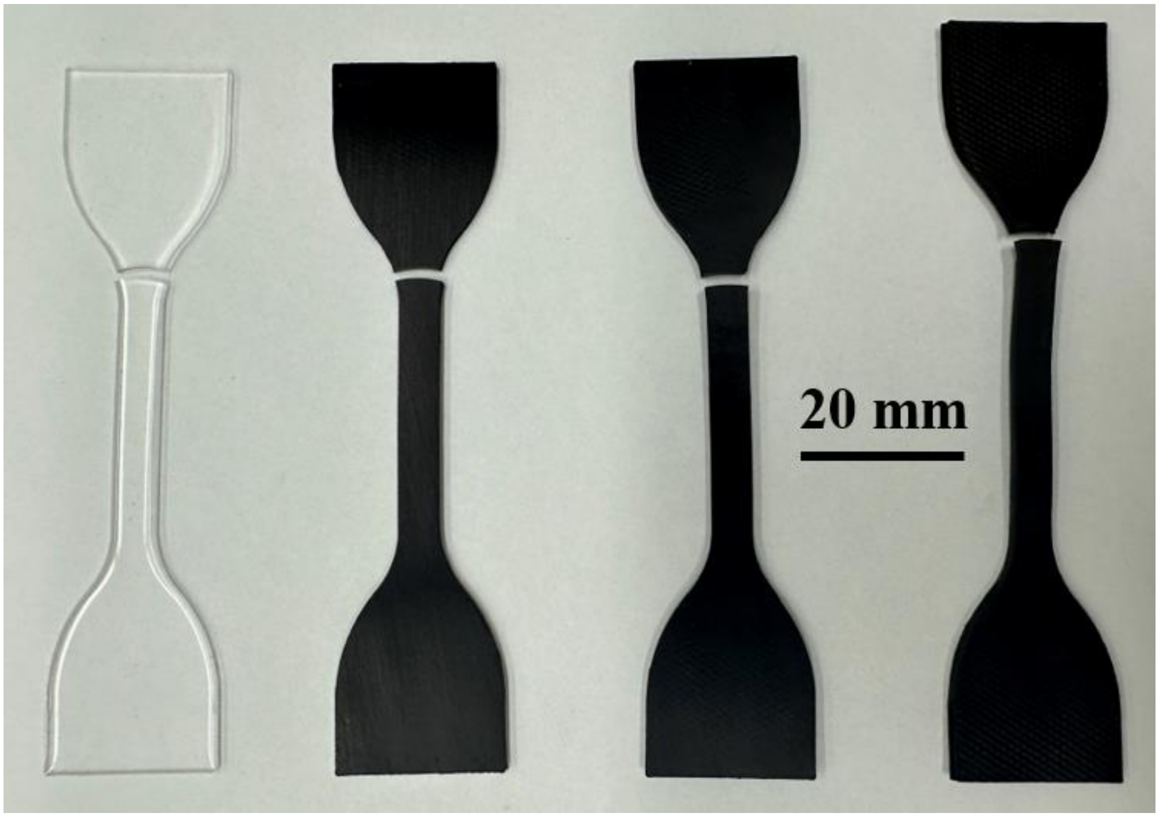

Figure 5.2. Non-ribbed PDMS tensile test specimens with CNT loadings, from left to right, of 0 wt%, 1 wt%, 3.5 wt%, and 10 wt% fabricated according to ASTM D638-22 specifications and subjected to uniaxial tension to failure.

The fractured samples shown in Figure 5.2 are representative of the uniaxial tension behavior for their respective material compositions. The neat PDMS (0 wt% CNT) sample, shown on the left, recovered much of its original shape after fracture, as evidenced by negligible necking through the gauge length. The 1 wt% and 3.5 wt% CNT samples also lack a necking region. The 10 wt% sample, however, shows considerable deformation within the gage length since it is no longer straight, compared to the other samples in Figure 5.2. The 10 wt% sample was also elongated compared to the other samples, which suggests it had undergone more plastic deformation during testing. Each tab shows small circular imprints from the grips, which validates that the grip-strength was high enough to prevent the specimens from slipping when subjected to a uniaxial tension load.

The average ultimate engineering strain and strength were obtained from the five specimens of each material with the corresponding standard deviations (Figure 5.3). By accurately characterizing the material strength, failure criteria for ribbed thin-film systems can be obtained to improve the design of new material systems, such as ribbed CNT-PDMS systems.

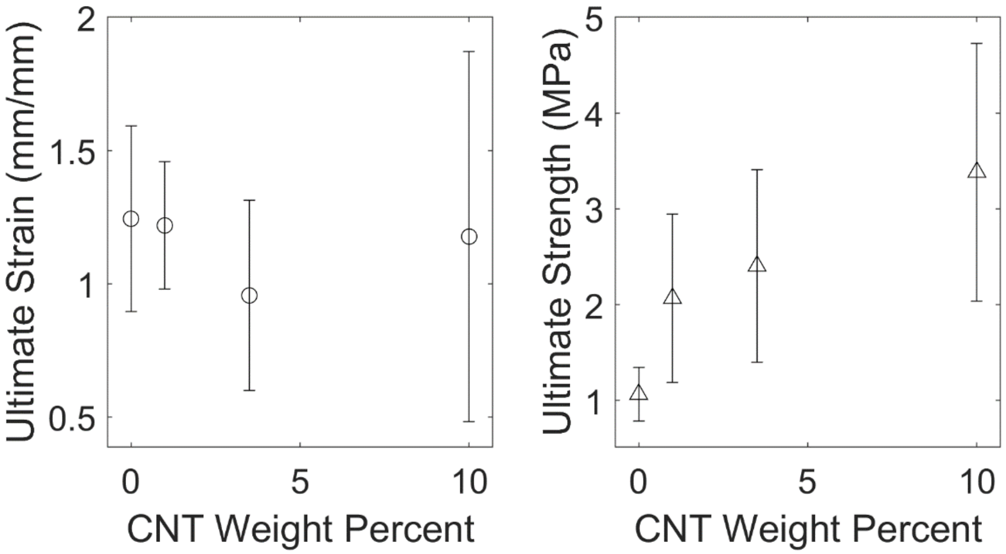

Figure 5.3. Ultimate engineering strain and ultimate engineering strength with respect to CNT weight percent in PDMS obtained from the average of five samples with error bars indicating two standard deviations.

From Figure 5.3, there is no statistically significant change in ultimate strain with respect to CNT loading. The ultimate strength, however, had a statistically significant increase with respect to increasing CNT loading. The high-strength and high-modulus elastic CNT fillers increased the overall strength of the material, and the PDMS matrix allowed for effective stress-transfer between neighboring CNTs. At 10 wt%, the standard deviation for the ultimate strain is one-third of the ultimate strain value, which suggests the difficulty with reliably incorporating the high weight fraction of CNTs in the PDMS matrix, and this is an indication of as the weight percentage increases, interactions between the CNTs and the PDMS increases, which can result in inconsistent load transfers [14].

The tensile strengths in Figure 5.3 are up to three times larger than those reported [45] for identical CNT-PDMS compositions, though the difference is likely attributed to different sample thicknesses which has been reported to affect the elongation modulus and ultimate strength of thin-films [75,76]. Since the characterization of these non-ribbed CNT-PDMS samples will inform the design of ribbed thin-film systems, the ultimate strain and strength in Figure 5.3 can be used to represent the material behavior.

5.3 Scanning Electron Microscopy Imaging of PDMS and CNT-PDMS Morphology

5.3.1 Scanning electron microscopy procedure for non-conductive materials

The CNT-PDMS morphology and the damage modes of the nanocomposite was characterized using SEM. A Hitachi SU8700 field emission SEM was used, which allows for ultra-high-resolution imaging at low electron emission energies on insulating samples with no conductive coating. Since the CNT-PDMS samples are non-conductive compared to typical SEM samples a low voltage of 100 V with a current of 91.5 mA and rapid image capturing was used to manage the sample charge and minimize damage to the samples.

SEM imaging was used to investigate the distribution, alignment, and agglomeration of CNTs within the PDMS at several length scales for three CNT loadings: 1 wt%, 3.5 wt%, and 10 wt%. Neat PDMS was also imaged to validate that the samples did not contain voids. The cross-section of the fracture surface produced by the experimental uniaxial testing in Chapter 5.2 was analyzed to understand the effect of CNTs on the mode of fracture. Magnification levels between 250 and 50,000 were used to view details ranging from the fracture surface texture to the orientation of individual CNTs. Images were also obtained using the electron backscatter detector of the Hitachi SU8700 instrument to better view the sample texture resulting from fracture.

5.3.2 Scanning electron microscopy results for PDMS and CNT-PDMS samples

SEM was used to further understand and characterize how the addition of CNTs in PDMS affects the deformation and damage modes during large-strain uniaxial loading. The fracture surface of each sample from Figure 5.2 was analyzed to understand the agglomeration, dispersion, and orientation of the CNTs for each material composition and to provide insight on the mode of fracture. Despite the ultra-high-resolution capabilities of the Hitachi SU8700 field emission SEM, the resolution is limited by the beam-material interaction. PDMS exhibits significant charging challenges and is susceptible to damage from the electron dose. This allows for high resolution images of the surface morphology at low beam energies, which manages charging and reduces damage.

The fracture surface of non-ribbed PDMS was observed under SEM (Figure 5.4). The surface appears featureless in part due to the non-conductive material properties that make SEM imaging difficult, but also due to the flat fractured topography and the absence of voids indicating the adequate molding of the PDMS thin-film due to degassing.

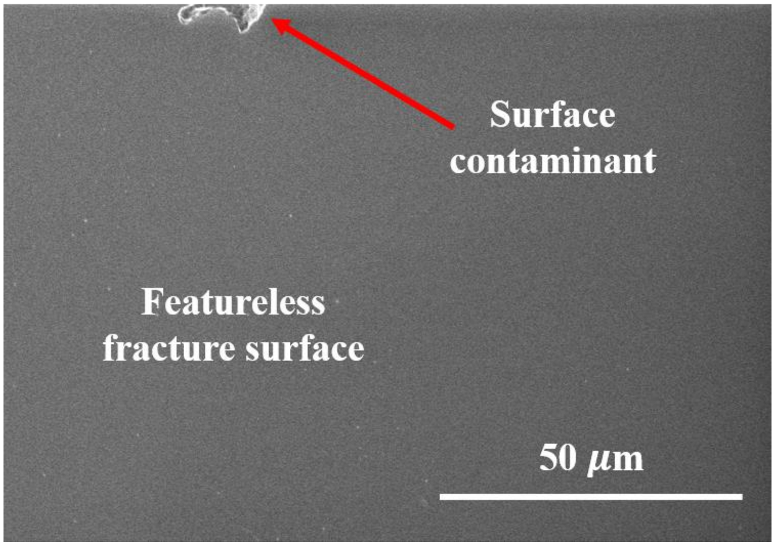

Figure 5.4. Scanning electron microscopy (SEM) micrograph of fracture surface at low magnification for neat PDMS obtained using electron beam of 100 V. The texture of the sample is featureless apart from a surface contaminant shown to demonstrate that the material is focused in the SEM.

The fracture surfaces of PDMS with 1 wt% and 3.5 wt% CNT were also observed at low and mid-powered magnification using SEM (Figure 5.5). The addition of CNTs provides sufficient texture on the fracture surface and increases the conductivity of the samples to makes SEM micrographs obtainable despite charging.

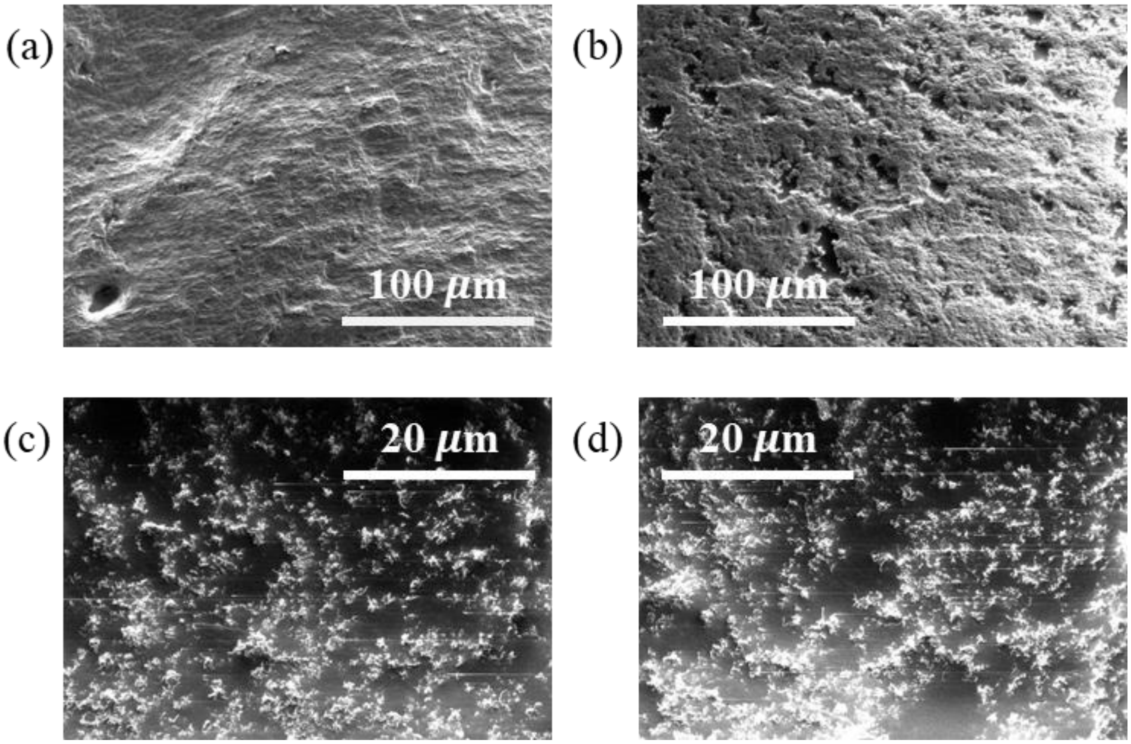

Figure 5.5. Scanning electron microscopy micrograph of fracture surface at low magnification for (a) 1 wt% and (b) 3.5 wt% CNT and at higher magnification for (c) 1 wt% and (d) 3.5 wt% CNT obtained using electron beam of 100 V. The texture of the two samples is rough but suggests a brittle-like fracture of the heterogenous material. The lighter regions in (c) and (d) indicate areas of high CNT concentration.

In Figures 5.5a-b, the fracture surface of both material compositions indicates brittle-like fracture, though the topography is more varied than in neat PDMS (Figure 5.4) due to the incorporation of CNT bundles. Unlike neat PDMS, the 1 wt% and 3.5 wt% CNT materials were not degassed during the specimen fabrication step in Chapter 5.2.1, however, there is no sign of voids in either material. The dark regions in Figure 5.5b are polymer-rich and likely locations for local damage to initiate given the lower relative strength of the polymer chains compared to the

CNT-polymer bundles. The fracture surface exhibits uniform deformation, similar to other materials such as high-strength metals undergoing low strain rates (10^{-3} s^{-1}) [103].

Figures 5.5c-d provide better insights into the heterogeneity of the CNT-PDMS system, namely the agglomeration and distribution of the CNTs. The lighter regions, in general, are bundles of CNTs [89]; the darker regions are PDMS. Bright horizontal streaks appear in Figures 5.5c-d because of the highly charged material, even at the low beam energy. The high surface energy of the CNTs cause them to agglomerate into pockets or bundles rather than disperse evenly and randomly in the PDMS. The presence of these bundles explains why the strengthening of the CNTs is not as high as homogenization techniques such as rule of mixtures or micromechanical models that neglect an interphase region would suggest since the bundle has a lower strength than the individual CNT [39,58,65,104–106]. Though individual CNTs agglomerate into bundles, these multi-phase CNT bundles can reasonably be assumed to be distributed uniformly within the PDMS. The 3.5 wt% CNT material in Figure 5.5d shows a similar distribution as the 1 wt% CNT material in Figure 5.5c, but with a higher density of CNT bundles. This uniform dispersion provides justification for homogenization techniques when the macroscale material behavior is considered.

PDMS with 10 wt% CNT had excessive charging. A micrograph was obtained with the backscatter electron middle detector of the Hitachi (Figure 5.6) at high magnification to better understand the topography of the fracture surface.

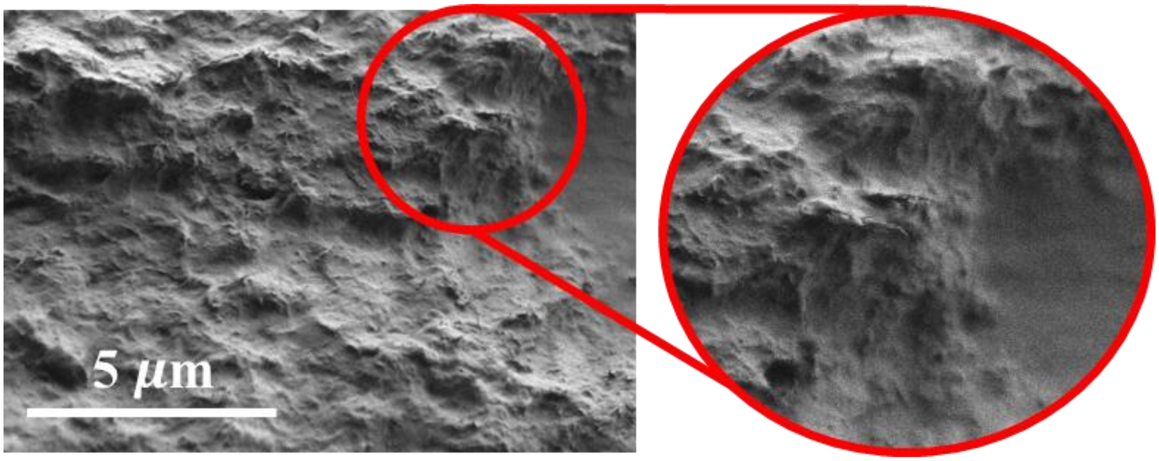

Figure 5.6. Scanning electron microscopy (SEM) backscatter micrograph of fracture surface for 10 wt% CNT at high magnification obtained using electron beam of 100 V showing CNT pullout.

The backscatter electron image (Figure 5.6) shows the highly irregular fracture surface of the 10 wt% CNT material, which is indicative of a more ductile failure mode than for CNT-PDMS compositions with lower CNT loadings. The expanded region in Figure 5.6 shows individual CNTs being pulled from the PDMS matrix at the peaks of the fracture surface. CNT pullout is a non-reversible mode of deformation in CNT-polymer systems that increases the toughness and occurs when the bonding or cohesion strength between the filler and the matrix is less than the shear stress subjected to the CNT-polymer interface. The likelihood of CNT pullout increases with increasing CNT content because the high concentration of CNT bundles, as observed in Figure 5.6, begin to act as defects rather than strengthening mechanisms [45,56]; the polymer chains are not capable of wetting the individual CNTs fully.

Low to high magnification SEM images of PDMS with CNT contents between 1 wt% and 10 wt% were obtained that show the CNTs are agglomerated into well-distributed CNT bundles throughout the PDMS (Figure 5.5 and 5.6). The orientation, waviness, and damage of individual

CNTs, however, requires ultra-high magnification to be observed (Figure 5.7). Knowledge of the CNT orientations and misorientations provides insight into the validity of isotropic material assumptions. Excessive CNT waviness or damage indicates a decrease in achievable strengthening of the composite resulting from the fabrication process [107].

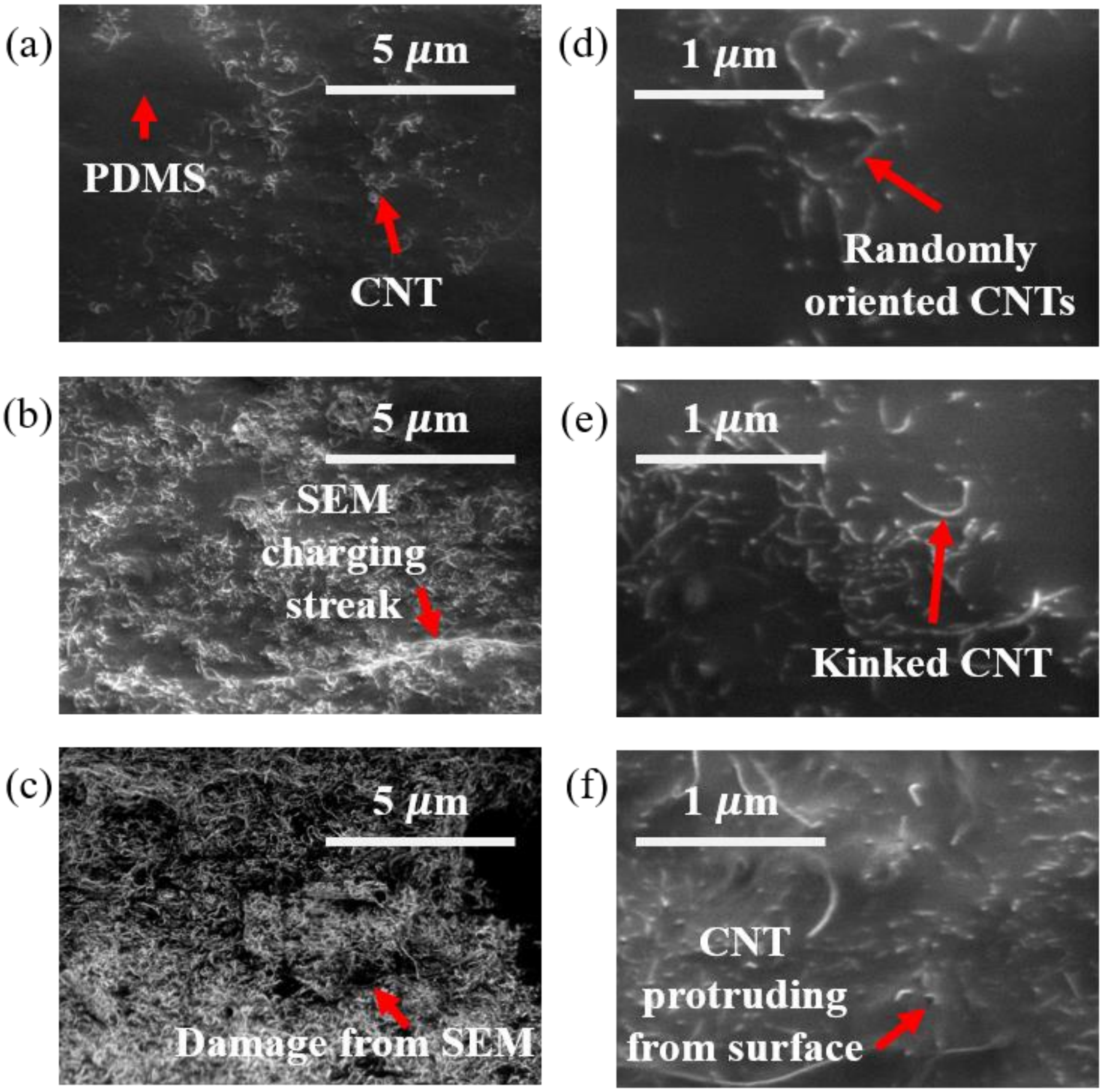
(a)
5 μm
PDMS
CNT
(d)
1 μm
Randomly oriented CNTs
(b)
5 μm
SEM charging streak
(e)
1 μm
Kinked CNT
(c)
5 μm
Damage from SEM
(f)
1 μm
CNT protruding from surface

Figure 5.7. Scanning electron microscopy (SEM) micrograph of fracture surface at high magnification for (a) 1 wt%, (b) 3.5 wt% and (c) 10 wt% CNT and at ultra-high magnification for (d) 1 wt%, (e) 3.5 wt% and (f) 10 wt% CNT obtained using electron beam of 100 V.

The SEM images in Figure 5.7 are consistent with the observations and measurements [12,108] for CNT-PDMS and similar CNT-polymer systems [39,54,69,107,109]. In Figures 5.7a-c, the effect of adding CNTs to PDMS is clear by the increase of fiber density. At low weight fractions (Figure 5.7a) there exists regions of PDMS that do not have a large presence of CNTs or CNT bundles, in which the stress is transferred through the lower strength matrix only. As the CNT content increases to 3.5 wt% (Figure 5.7b), there are fewer regions of pure PDMS and the heterogenous microstructure allows for stress to transfer shorter distances through the PDMS to adjacent CNT bundles. The SEM micrograph of CNT-PDMS with 10 wt% CNT (Figure 5.7c) demonstrates how little PDMS remains between CNT bundles, which suggests that the material has difficulty transferring the uniaxial tensile load from one bundle to another and that some regions may not be encapsulated by enough polymer. The dark lines in Figure 5.7c indicate damage from taking images; the damage pattern is consistent with the raster scan path—a left vertical line with rightward horizontal forks. The damage helps demonstrate the difficultly of imaging a polymer, despite the low electron dose enabled by using a low-voltage field emission SEM.

At higher magnification, individual CNTs can be clearly seen (Figures 5.7d-f), which provided information on the orientation and defect nature of the CNT-PDMS. There exists CNTs within the fracture surface for all three CNT loadings that exhibit kinks at an angle of at least 90°, consistent with SEM images from [107]. Within a given CNT bundle, the CNTs were randomly oriented. This randomness is due to the extensive mixing process used to fabricate the samples. The randomly oriented CNTs validate that each bundle can be treated as an isotropic effective fiber.

SEM images were obtained to understand how adding CNTs to PDMS affects the microstructure and strengthens the material. The multi-phase and heterogeneous material exhibit superhydrophobic behavior from the hierarchal topography. Though CNTs coalesce into multi-phase agglomerations, the random orientation of CNTs and dispersion of CNT bundles provide justification for treating non-ribbed and ribbed CNT-PDMS thin-film systems as isotropic, homogeneous materials.

5.4 Characterization of PDMS and CNT-PDMS as Viscoelastic and Hyper-viscoelastic Materials

The uniaxial tensile testing in Chapter 5.2 provides a description of the global mechanical behavior of CNT-PDMS for various compositions; SEM imaging in Chapter 5.3 improves our understanding of the heterogeneous microstructure and the fracture surface. However, it is still not understood how to best characterize the bulk material behavior for use in ribbed thin-film systems subjected to large strains and strain rates. Several constitutive and phenomenological materials models have been developed to understand the mechanical behavior of polymer and composite materials, such as hyperelasticity and hyper-viscoelasticity. Both material models can predict the material response to uniaxial tension. To understand how best to represent the large-strain mechanical behavior of various CNT-PDMS compositions, a hyperelastic and hyper-viscoelastic material model was obtained for each composition to determine the more physically-accurate material model.

First, a Yeoh hyperelastic material model was optimized to represent the material behavior of the experimental stress-strain measurements. For each material composition, the Yeoh material model was obtained from the initialized hyperelastic material model coefficients ($C_{10,init}$ = 0.1, $C_{20,init}$ = 0.01, $C_{30,init}$ = 0.001) for strains up to the ultimate strain. The residuals were obtained for the stress predicted by the model and measured in each of the five specimens. To force the material model to satisfy the ultimate strength, additional residuals between the maximum predicted stress and the average ultimate strength were added to the residual vector with a weight factor. This weight factor was manually adjusted to obtain an appropriate material model that adequately accounted for the ultimate strength without obscuring the global stress-strain behavior. The root-mean-square-error (RMSE) was obtained from the residual vector and a constrained interior-point optimization procedure was conducted to update the hyperelastic material model coefficients for each material composition.

Thus, the optimization problem statement was to find C_{10}, C_{20}, and C_{30} that minimize the root mean square error, $RMSE = \sqrt{\frac{1}{n}\left(\sigma_{experiments} - \sigma_{Yeoh}\right)^2}$, for each material composition where the uniaxial stress history of each sample was appended into a single column vector, $\sigma_{experiments}$, and the corresponding uniaxial stress predicted by the Yeoh material model was appended into a column vector, σ_{Yeoh}, both of length n. The Yeoh material model for the four CNT-PDMS compositions are summarized in Table 5.1.

Table 5.1. Hyperelastic Yeoh material model coefficients of four compositions of CNT-PDMS obtained by constrained optimization routine with root-mean-square-error.

CNT Weight Percent	Yeoh Hyperelastic Material Model Coefficients			Root-Mean-Square-Error
(wt% CNT)	C_{10} (MPa)	C_{20} (MPa)	C_{30} (MPa)	(MPa)
0	0.1303	0.0185	0.0013	0.0078
1	0.2713	0.0321	0.0027	0.0111
3.5	0.5330	0.0299	0.0062	0.0043
10	0.8715	0.0082	-0.0024	0.0811

Similarly, the Yeoh-Prony hyper-viscoelastic material model was optimized for each material composition. Neat PDMS has been characterized as viscoelastic [17,63,64,110] so the composite material is also expected to exhibit viscoelastic relaxation. The same optimization procedure was used, though the material was allowed to relax according to Equation (2.7) assuming a constant nominal strain-rate as specified in Chapter 5.2.1 to account for the time-dependency of the mechanical testing procedure. Thus, the three Yeoh coefficients (C_{10}, C_{20}, C_{30}) and three Prony relaxation coefficients (g_1, g_2, g_3) were obtained for each material that minimize the RMSE. The Prony time constants, τ_i, were 1, 10, and 100 seconds. The total time of each uniaxial tension test was between 220 and 520 seconds, so the choice of τ_i captures the fast and slow relaxation mechanisms that were observed during testing. The optimized hyper-viscoelastic material model coefficients are summarized in Table 5.2 with the corresponding RMSE for each CNT-PDMS composition.

Table 5.2. Hyper-viscoelastic Yeoh-Prony material model coefficients of four compositions of CNT-PDMS obtained by constrained optimization routine with root-mean-square-error.

CNT Weight Percent (wt% CNT)	Yeoh Hyperelastic Coefficients			Prony Viscoelastic Relaxation Coefficients			Root-Mean-Square-Error (MPa)
	C_{10} (MPa)	C_{20} (MPa)	C_{30} (MPa)	g_1	g_2	g_3	
0	0.2133	0.0634	0.0016	0.0654	0.1509	0.5679	0.0078
1	0.4010	0.0888	0.0016	0.1510	0.0582	0.3826	0.0111
3.5	0.6320	0.0372	0.0069	0.1487	0.0100	0.0033	0.0043
10	2.2985	0.1142	-0.0242	0.4144	0.2377	0.0004	0.0806

The first coefficient in the Yeoh material model, C_{10}, is interpreted as approximately half of the shear modulus of the material [68]. Based on Table 5.1, the instantaneous elongation modulus for the hyperelastic material models, assuming an incompressible material, ranges between 0.75 MPa and 5.25 MPa for the various compositions. These values are slightly lower than those that have been experimentally obtained; 1 MPa for 0 wt%, 5.7 MPa for 3.5 wt%, and 10 MPa for 10 wt% CNT [45]. The hyperelastic material model from Table 5.1 underestimates the stress in the small-strain regime, but by including the viscoelastic relaxation, the magnitude of the hyperelastic coefficient C_{10} increases (Table 5.2) to account for the rate-dependent behavior. The estimated elongation modulus from C_{10} for the hyper-viscoelastic material model is 1.28 MPa for 0 wt%, 2.41 MPa for 1 wt%, 3.79 MPa for 3.5 wt%, and 13.79 MPa for 10 wt% CNT, which are consistent with reported values [45]. Thus, the hyper-viscoelastic material models accurately capture the mechanical behavior in the small-strain regime because they account for the rate-dependent relaxation of the polymer, the interactions between CNTs and polymer chains, and the uniaxial testing quasi-static rates.

The second and third coefficients of the Yeoh hyperelastic model, C_{20} and C_{30}, describe the stress-strain response in the mid- and large-strain regimes. In both the hyperelastic and hyper-viscoelastic material model formulations (Tables 5.1 and 5.2), C_{30} increases with increasing CNT loading up to 3.5 wt%; after which, C_{30} is negative at 10 wt% CNT. The most likely cause for the stress increasing in the large-strain regime is the straightening of the curved CNTs observed in Figure 5.7, that provide additional stiffness to the thin samples [111]. The 10 wt% CNT material begins to plateau in the large-strain regime, which is consistent with [56] and is likely due to poor bonding between the PDMS and CNT bundles or the separation of large CNT agglomerations that are not properly adhered to the PDMS, as observed in SEM images (Figure 5.7).

The Yeoh hyperelastic material behavior is compared to the five specimens for each material in Figure 5.8. Here, the addition of CNTs in the PDMS increases the ultimate strength for all compositions. All four material models show good agreement with the experimental uniaxial tension data. Similarly, the Yeoh-Prony hyper-viscoelastic material model behavior is compared to the uniaxial testing results for each material in Figure 5.9. As with Figure 5.8, the addition of CNTs in the PDMS increases the initial stress-strain slope and increases the ultimate strength for CNT loadings up to 10 wt%. Both the hyperelastic and hyper-viscoelastic material models can predict the mechanical behavior of CNT-PDMS for various compositions.

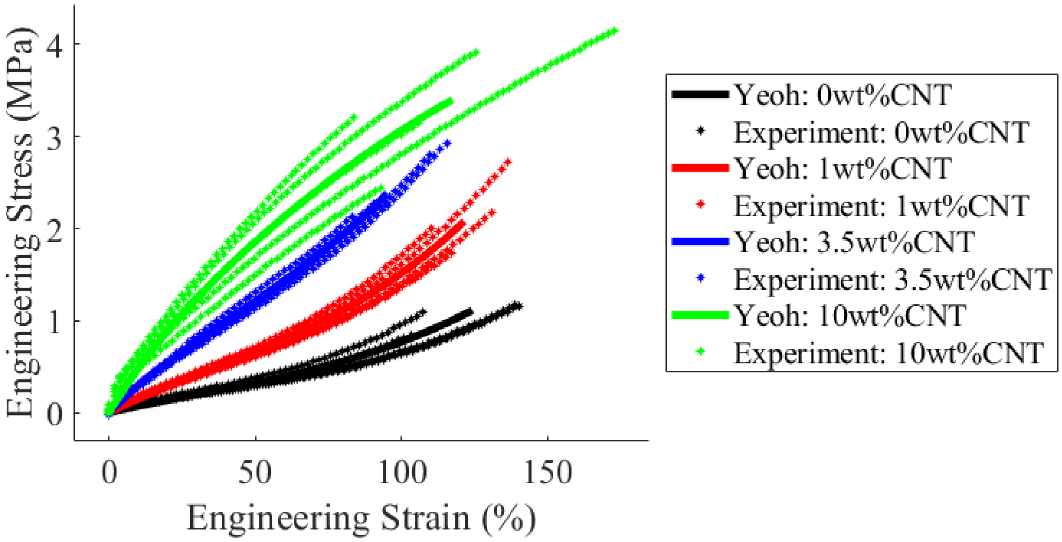

Figure 5.8. Yeoh hyperelastic material model for four material compositions of CNT-PDMS optimized from five uniaxial tension experiments of each composition.

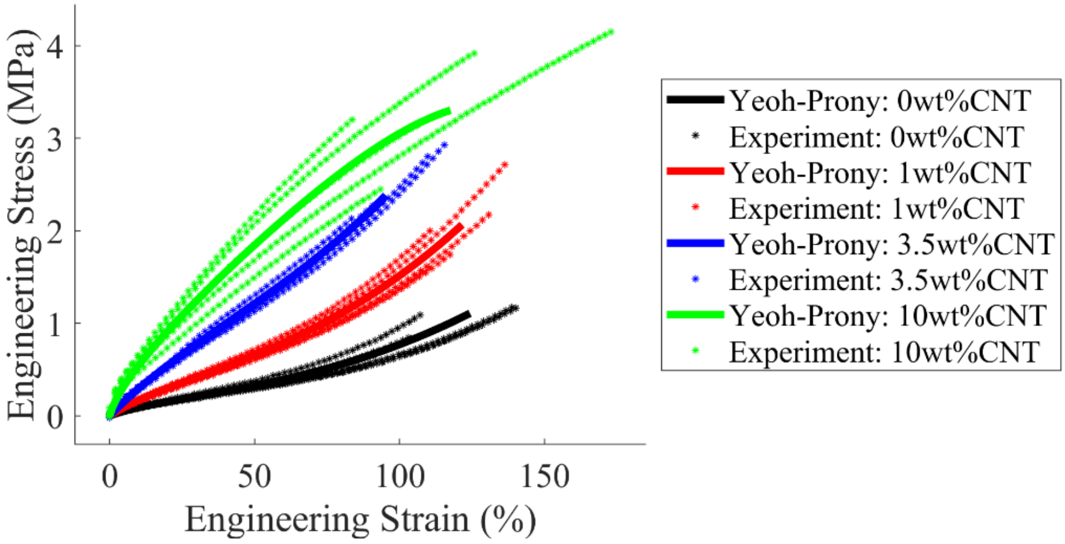

Figure 5.9. Yeoh-Prony hyper-viscoelastic material model for four material compositions of CNT-PDMS optimized from five uniaxial tension experiments of each composition.

The RMSE for the hyperelastic and hyper-viscoelastic material models are comparable for each material composition. Though, since the hyper-viscoelastic material model accounts for the loading rate of the uniaxial tests and the rate-dependent viscoelastic material relaxation, it is likely the more accurate prediction of the mechanical behavior and can be used reliably for low strain-rate responses on the order of 10^{-3} s^{-1}, similar to the uniaxial testing strain-rate given in Chapter 5.2.1. Thus, the hyper-viscoelastic material models better represent the global stress-strain behavior.

The ideal CNT-PDMS composition for multifunctional systems exhibiting large-strain and high-strength behaviors is between 3.5 wt% and 10 wt% CNT. Though the tensile strength increases with increasing CNT loading, as suggested in Figure 5.3, it does so with diminishing returns. SEM micrographs indicate that CNTs agglomerate into randomly oriented, well-dispersed bundles; the micrographs support observations of hydrophobic surface behaviors because of the hierarchal CNT-PDMS topography. The global stress-strain mechanical behavior (Figures 5.8 and 5.9) suggests that the CNTs no longer act as strengthening mechanisms, but as defects as the CNT loading increases to 10 wt%. Hyper-viscoelastic material models accurately predict the large-strain rate-dependent bulk mechanical behavior of thin CNT-PDMS systems, and can be used to predict the behavior of ribbed thin-film systems.

5.5 Conclusions

Large-strain hyperelastic and hyper-viscoelastic material behavior of PDMS and CNT-PDMS samples with various CNT weight percentages were obtained to understand and characterize the effects of CNT loading, agglomeration, dispersion, and alignment on the global and local mechanical behavior and how to physically represent the material behavior. Thin PDMS and CNT-PDMS samples were fabricated and subjected to quasi-static uniaxial testing until failure. The ultimate strain, ultimate strength, and global stress-strain behavior of each CNT-PDMS composition was obtained and related to the CNT content. Increasing the loading content of CNT did not affect the ultimate strain at which the thin samples fractured, though it increased the ultimate strength. The instantaneous elongation modulus of the CNT-PDMS compositions were consistent with experimentally observed measurements. High-strength elastic CNTs additions to the viscoelastic PDMS significantly increased the material stiffness. CNT-PDMS with CNT loadings between 0 wt% (neat PDMS) and 3.5 wt% exhibited a high rate-increase of stress in the large-strain regime; the stress in PDMS with 10 wt% CNT plateaued in this regime indicating that the material had reached its loading strength of the CNTs.

The fracture surface of each sample was analyzed by SEM to understand the surface morphology and the incorporation of CNTs in the PDMS from the three-roll shear mixing procedure. SEM images of neat PDMS indicated that the material contained no voids. CNT-PDMS with 1 wt% and 3.5 wt% CNT content showed a near-uniform fracture surface, indicating that the failure initiated with failure of the PDMS, whereas CNT-PDMS with 10 wt% CNT showed CNT pullout, which indicates that failure initiated within CNT bundles.

A Yeoh hyperelastic and a Yeoh-Prony hyper-viscoelastic material model were shown to physically represent each material composition to understand how best to model the large-strain bulk mechanical behavior of the multi-phase materials. Both material model formulations can describe the mechanical behavior in response to large-strain loading conditions. The hyper-viscoelastic model, however, also accounts for the rate-dependence, which would make it ideal for ribbed systems, which are subjected to high strain-rate loading conditions during loading.

By relating the hyper-viscoelastic global behavior to SEM micrographs of CNT-polymer systems can aid in establishing validated understanding of the distribution and agglomeration of CNT geometries and orientations within polymer matrix systems. This will enable manufacturers of heterogeneous, structured thin-film materials to predict and control the mechanical and surface behavior for multifunctional applications.

CHAPTER 6: Conclusions and Recommendations

A computational framework has been integrated with experimental observations and measurements to understand, predict, and design the manufacturing of ribbed thin-film systems and control the high strain-rate and large-strain behavior. The predictive approach was informed from experimental observations, including large-scale rolling to manufacture structured thin-films, dynamic mechanical analysis testing to characterize the rheological behavior, uniaxial tension testing to evaluate the global stress-strain behavior, and scanning electron microscopy imaging to determine the morphology of thin CNT-PDMS samples.

The computational framework of the large-scale rolling process accounted for material viscoelasticity, high contact pressure, large displacements, and the ribbing morphology. A ribbing instability model was formulated from finite-element predictions and experimental observations to relate the manufacturing conditions and material selection to the resulting ribbing microstructure. A critical aspect ratio was observed for which the film stress attained a maximum value.

The dynamic behavior of ribbed PDMS and CNT-PDMS thin-films in response to high strain-rate compressive loading was predicted using a representative volume element computational framework. The framework accounted for material thermo-viscoelasticity to predict the change in temperature and the ribbing morphology to understand how the microstructure mitigates the complex three-dimensional stress-wave propagation. Hypersurfaces of the maximum stress were obtained for each material; a surrogate model was trained from the hypersurfaces and optimized to predict the relation between the film microstructure and material selection and the minimax stress in response to a wide range of dynamic loadings. PDMS thin-films with a maximum ribbing aspect ratio were determined to minimize adverse dynamic behaviors in response to high strain-rate loadings, whereas the minimax stress of CNT-PDMS thin-films showed little sensitivity to the ribbing microstructure.

Lastly, the large-strain behavior and morphology of the fracture surface was characterized for PDMS and CNT-PDMS to understand how adding high-strength CNTs to PDMS enhances the strength and toughness of the thin-films. Characterizing the global stress-strain behavior of these thin-films as hyper-viscoelastic better accounts for the large-strain and time-dependent relaxation of the material that has been observed in experiments. The results showed that adding CNTs increased the effective stiffness and ultimate strength but did not have a significant effect on the ultimate strain of the material.

Based on this research, my recommendations for future research are to investigate the following:

- **Understanding film-splitting during large-scale rolling:** The large-scale rolling model included only a ribbed thin-film fixed to the bottom roller. In experimental rolling studies, the CNT-PDMS adheres to both rollers and the ribbing instabilities are generated in the meniscus of the separating CNT-PDMS surfaces. The separating thin-film material should be investigated by a dynamic fracture mechanics approach, where the crack-speed of the material can be related to the rotational speed of the two-roll process. Understanding the relation between the material toughness and the ribbing formation is crucial for the further design of ribbed damage-tolerant thin-systems.
- **Modeling the evolution of fiber alignment during large-scale rolling:** Just as cold-rolling metals aligns and elongates grains in the rolling direction, so does rolling continuous-fiber, short-fiber, and nano-fiber-polymer composites align the fiber reinforcements in the rolling direction. With each pass through the roller gap, the CNTs

gradually orient in the rolling direction due to shear forces as observed in the cross-section of the roller gap. Multiscale modeling techniques, such as hierarchal representative volume element modeling, can account for the effect that the micro-scale alignment, dispersion, and orientation, of the CNTs have on the effective bulk properties of the thin-film, that will vary as a function of processing time and speed and the shear force exerted on the CNT-PDMS material.

- **Understanding the microstructural characteristics of CNT-oxide-based ribbed systems:** Preliminary testing has shown improved ribbing linearity with decreased ribbing wavelengths by incorporating oxide inclusions up to 0.5 weight percent in CNT-PDMS. Although the maximum ribbing amplitude achieved using these materials was less than for CNT-PDMS, which may limit its superhydrophobic or drag-reducing capabilities, the resulting microstructure and mechanical and thermal behavior should be investigated because the addition of oxides can increase the film strength and toughness beyond what was achieved by adding only CNTs.
- **Predicting the fatigue life and toughness of ribbed CNT-PDMS thin-films:** The fracture toughness of thin PDMS and CNT-PDMS samples was investigated through the analysis of SEM images of the fracture surface. Adding CNTs to the PDMS increased the ability for the thin material to deform and increased its overall strength. It is also necessary to obtain quantitative measure of the toughness to better design the thin-films for use. Additionally, the fatigue life of these thin-film systems can be obtained by a combination of experimental, theoretical, and computational efforts, which would inform the projected lifetime of the material for a given application and aid in estimating the economic feasibility of such a thin-film system for reducing drag.

- **Quantifying how surface adhesion and asperities affect the ribbed thin-film dynamic behavior:** The ribbing profile of the structured thin-films has so far only considered a single ribbing wavelength in the transverse rolling direction with a single corresponding ribbing amplitude; this has been modeled as a fundamental sine wave. More complex characterizations of the ribbing morphology should be investigated that consider not only the superposition of sine waves with different ribbing amplitudes and wavelengths, but also features in the rolling direction, related to the capillary bridging effect. Mandelbrot fractal topologies can be used for representing the thin-film morphology, which will better inform computational models predicting the manufacturing and performance of these thin-films.
- **Implementing an integrated finite-element-artificial intelligence (FE-AI) neural network to design structured films for multifunctional applications:** Computational models informed from experimental observations generate large quantities of data, which can be leveraged using advancements in artificial intelligence to uncover relations between manufacturing conditions and material properties on the microstructure and performance of thin-film systems. Moreover, integrating the finite-element modeling results within an artificial intelligence framework provides the basis for high-throughput design of structured thin-film system for multifunctional applications. A combination of feed-forward neural networks (FFNNs) and deep convolution generative adversarial neural networks (DCGANs) can be trained and validated to predict the rolling manufacturing conditions and CNT weight percent necessary to obtain a thin-film with the desired ribbing morphology, film strength and toughness, and thermal properties; the framework can then predict the global stress-strain behavior and the corresponding scanning electron microscopy image of the designed material.

REFERENCES

[1] J. Ryu, K. Kim, J. Park, B.G. Hwang, Y. Ko, H. Kim, J. Han, E. Seo, Y. Park, S.J. Lee, Nearly Perfect Durable Superhydrophobic Surfaces Fabricated by a Simple One-Step Plasma Treatment, Sci. Rep. 7 (2017) 1981. https://doi.org/10.1038/s41598-017-02108-1.

[2] C. Yang, F. Wang, W. Li, J. Ou, C. Li, A. Amirfazli, Anti-icing properties of superhydrophobic ZnO/PDMS composite coating, Appl. Phys. A 122 (2016) 1. https://doi.org/10.1007/s00339-015-9525-1.

[3] Y. Sun, Z. Yang, L. Li, Z. Wang, Q. Sun, Facile preparation of isotactic polypropylene microporous membranes with bioinspired hierarchical morphology for nano-scale water-in-oil emulsion separation, J. Membr. Sci. 581 (2019) 224–235. https://doi.org/10.1016/j.memsci.2019.03.058.

[4] M.D. Islam, H. Perera, B. Black, M. Phillips, M. Chen, G. Hodges, A. Jackman, Y. Liu, C. Kim, M. Zikry, S. Khan, Y. Zhu, M. Pankow, J.E. Ryu, Template-Free Scalable Fabrication of Linearly Periodic Microstructures by Controlling Ribbing Defects Phenomenon in Forward Roll Coating for Multifunctional Applications, Adv. Mater. Interfaces 9 (2022) 2201237. https://doi.org/10.1002/admi.202201237.

[5] C. Guo, Q. Tian, H. Wang, J. Sun, L. Du, M. Wang, D. Zhao, Roller embossing process for the replication of shark-skin-inspired micro-riblets, Micro Nano Lett. 12 (2017) 439–444. https://doi.org/10.1049/mnl.2016.0759.

[6] S.-H. Park, S. Lee, D. Moreira, P.R. Bandaru, I. Han, D.-J. Yun, Bioinspired superhydrophobic surfaces, fabricated through simple and scalable roll-to-roll processing, Sci. Rep. 5 (2015) 15430. https://doi.org/10.1038/srep15430.

[7] L. Cao, A.K. Jones, V.K. Sikka, J. Wu, D. Gao, Anti-Icing Superhydrophobic Coatings, Langmuir 25 (2009) 12444–12448. https://doi.org/10.1021/la902882b.

[8] N. Liu, Q. Sun, Z. Yang, L. Shan, Z. Wang, H. Li, Wrinkled Interfaces: Taking Advantage of Anisotropic Wrinkling to Periodically Pattern Polymer Surfaces, Adv. Sci. 10 (2023) 2207210. https://doi.org/10.1002/advs.202207210.

[9] M.J. Imburgia, A.J. Crosby, Rolling wrinkles on elastic substrates, Extreme Mech. Lett. 6 (2016) 23–30. https://doi.org/10.1016/j.eml.2015.11.003.

[10] Q. Xu, W. Zhang, C. Dong, T.S. Sreeprasad, Z. Xia, Biomimetic self-cleaning surfaces: synthesis, mechanism and applications, J. R. Soc. Interface 13 (2016) 20160300. https://doi.org/10.1098/rsif.2016.0300.

[11] F. Xu, M. Potier-Ferry, Quantitative predictions of diverse wrinkling patterns in film/substrate systems, Sci. Rep. 7 (2017) 18081. https://doi.org/10.1038/s41598-017-18267-0.

[12] D. Kim, K.-S. Yun, Patterning of carbon nanotube films on PDMS using SU-8 microstructures, Microsyst. Technol. 19 (2013) 743–748. https://doi.org/10.1007/s00542-012-1677-8.

[13] H. Shang, X. Liang, F. Deng, S. Hu, S. Shen, Flexoelectricity in wrinkled thin films, Int. J. Mech. Sci. 234 (2022) 107685. https://doi.org/10.1016/j.ijmecsci.2022.107685.

[14] T. Sharma, Y. Vamsi Krishna, A. Kumar, Buckling of bi-layers under in-plane compression, Mater. Today Proc. 46 (2021) 5530–5534. https://doi.org/10.1016/j.matpr.2020.09.268.

[15] M. Didarul Islam, H. Perera, S. Chockalingam, M. Phillips, M.-J. Chen, Y. Liu, S. Khan, Y. Zhu, M. Zikry, J. Eun Ryu, Template-free scalable fabrication of linearly periodic microstructures by controlling ribbing defects phenomenon during forward roll coating, Manuf. Lett. 33 (2022) 153–160. https://doi.org/10.1016/j.mfglet.2022.08.001.

[16] H. Perera, B. Black, M.D. Islam, J.E. Ryu, R.D. Corder, S.A. Khan, Rheological Behavior and Roll Coating Properties of PDMS Enhanced with Multi-Walled Carbon Nanotubes and Fumed Silica, ACS Appl. Eng. Mater. 2 (2024) 618–627. https://doi.org/10.1021/acsaenm.3c00698.

[17] M. Phillips, M.-J. Chen, M.D. Islam, J. Ryu, M. Zikry, Predicting and Controlling Ribbing Instabilities of Carbon Nanotube–PDMS Thin-Film Systems for Multifunctional Applications, Adv. Eng. Mater. 25 (2023) 2300582. https://doi.org/10.1002/adem.202300582.

[18] M. Barahman, A.M. Lyons, Ratchetlike Slip Angle Anisotropy on Printed Superhydrophobic Surfaces, Langmuir 27 (2011) 9902–9909. https://doi.org/10.1021/la201222a.

[19] A.W. Lang, P. Motta, P. Hidalgo, M. Westcott, Bristled shark skin: a microgeometry for boundary layer control?, Bioinspir. Biomim. 3 (2008) 046005. https://doi.org/10.1088/1748-3182/3/4/046005.

[20] B. Bhushan, Lessons from nature for green science and technology: an overview and bioinspired superliquiphobic/philic surfaces, Philos. Trans. R. Soc. Math. Phys. Eng. Sci. 377 (2019) 20180274. https://doi.org/10.1098/rsta.2018.0274.

[21] R.J. Fields, M.F. Ashby, Finger-like crack growth in solids and liquids, Philos. Mag. 33 (1976) 33–48. https://doi.org/10.1080/14786437608221089.

[22] J.S. Biggins, L. Mahadevan, Meniscus instabilities in thin elastic layers, Soft Matter 14 (2018) 7680–7689. https://doi.org/10.1039/C8SM01033A.

[23] D.J. Coyle, C.W. Macosko, L.E. Scriven, Stability of symmetric film-splitting between counter-rotating cylinders, J. Fluid Mech. 216 (1990) 437–458.

[24] M. Decré, E. Gailly, J. -M. Buchlin, Meniscus shape experiments in forward roll coating, Phys. Fluids 7 (1995) 458–467. https://doi.org/10.1063/1.868644.

[25] M.D. Graham, Interfacial hoop stress and instability of viscoelastic free surface flows, Phys. Fluids 15 (2003) 1702. https://doi.org/10.1063/1.1568340.

[26] M.E.G. Castillo, A.T. Patera, Three-dimensional ribbing instability in symmetric forward-roll film-coating processes, J. Fluid Mech. 335 (1997) 323–359. https://doi.org/10.1017/S0022112096004600.

[27] M.D. Savage, Mathematical Model for the Onset of Ribbing, AICHe 30 (1984) 999–1002.

[28] J.P. Mmbaga, R.E. Hayes, F.H. Bertrand, P.A. Tanguy, Flow simulation in the nip of a rigid forward roll coater, Int. J. Numer. Methods Fluids 48 (2005) 1041–1066. https://doi.org/10.1002/fld.976.

[29] C.-H. Chien, J.-Y. Jang, Numerical and experimental studies of thin liquid film flow between two forward-rollers, J. Mech. Sci. Technol. 21 (2007) 1892–1900. https://doi.org/10.1007/BF03177446.

[30] T. Hasegawa, K. Sorimachi, Wavelength and depth of ribbing in roll coating and its elimination, AIChE J. 39 (1993) 935–945. https://doi.org/10.1002/aic.690390603.

[31] G.A. Zevallos, M.S. Carvalho, M. Pasquali, Forward roll coating flows of viscoelastic liquids, J. Non-Newton. Fluid Mech. 130 (2005) 96–109. https://doi.org/10.1016/j.jnnfm.2005.08.005.

[32] J. Nase, A. Lindner, C. Creton, Pattern Formation during Deformation of a Confined Viscoelastic Layer: From a Viscous Liquid to a Soft Elastic Solid, Phys. Rev. Lett. 101 (2008) 074503. https://doi.org/10.1103/PhysRevLett.101.074503.

[33] S. Xu, O. Rezvanian, M.A. Zikry, Electro-mechanical modeling of the piezoresistive response of carbon nanotube polymer composites, Smart Mater. Struct. 22 (2013) 055032. https://doi.org/10.1088/0964-1726/22/5/055032.

[34] S. Nikravesh, D. Ryu, Y.-L. Shen, Direct numerical simulations of three-dimensional surface instability patterns in thin film-compliant substrate structures, Sci. Rep. 11 (2021) 16449. https://doi.org/10.1038/s41598-021-95414-8.

[35] A. Schweikart, A. Fery, Controlled wrinkling as a novel method for the fabrication of patterned surfaces, Microchim. Acta 165 (2009) 249–263. https://doi.org/10.1007/s00604-009-0153-3.

[36] Y. Gao, X. Fang, J. Tan, T. Lu, L. Pan, F. Xuan, Highly sensitive strain sensors based on fragmentized carbon nanotube/polydimethylsiloxane composites, Nanotechnology 29 (2018) 235501. https://doi.org/10.1088/1361-6528/aab888.

[37] O. Kanoun, C. Müller, A. Benchirouf, A. Sanli, T. Dinh, A. Al-Hamry, L. Bu, C. Gerlach, A. Bouhamed, Flexible Carbon Nanotube Films for High Performance Strain Sensors, Sensors 14 (2014) 10042–10071. https://doi.org/10.3390/s140610042.

[38] A. Shar, P. Glass, S.H. Park, D. Joung, 3D Printable One-Part Carbon Nanotube-Elastomer Ink for Health Monitoring Applications, Adv. Funct. Mater. 33 (2023) 2211079. https://doi.org/10.1002/adfm.202211079.

[39] A.T. Sepúlveda, R. Guzman de Villoria, J.C. Viana, A.J. Pontes, B.L. Wardle, L.A. Rocha, Full elastic constitutive relation of non-isotropic aligned-CNT/PDMS flexible nanocomposites, Nanoscale 5 (2013) 4847. https://doi.org/10.1039/c3nr00753g.

[40] Y. Zhu, R. Cardinaels, J. Mewis, P. Moldenaers, Rheological properties of PDMS/clay nanocomposites and their sensitivity to microstructure, Rheol. Acta 48 (2009) 1049–1058. https://doi.org/10.1007/s00397-009-0387-3.

[41] A.R. Shajari, R. Ghajar, M.M. Shokrieh, Multiscale modeling of the viscoelastic properties of CNT/polymer nanocomposites, using complex and time-dependent homogenizations, Comput. Mater. Sci. 142 (2018) 395–409. https://doi.org/10.1016/j.commatsci.2017.10.006.

[42] H. Asadian, K. Shelesh-Nezhad, Simulation of dynamic mechanical and viscoelastic behavior in polymer/clay nanocomposites, Polym. Compos. 41 (2020) 817–823. https://doi.org/10.1002/pc.25412.

[43] M.M. Rahman, S. Zainuddin, M.V. Hosur, J.E. Malone, M.B.A. Salam, A. Kumar, S. Jeelani, Improvements in mechanical and thermo-mechanical properties of e-glass/epoxy composites using amino functionalized MWCNTs, Compos. Struct. 94 (2012) 2397–2406. https://doi.org/10.1016/j.compstruct.2012.03.014.

[44] F. Wang, L.T. Drzal, Y. Qin, Z. Huang, Size effect of graphene nanoplatelets on the morphology and mechanical behavior of glass fiber/epoxy composites, J. Mater. Sci. 51 (2016) 3337–3348. https://doi.org/10.1007/s10853-015-9649-x.

[45] J. Du, L. Wang, Y. Shi, F. Zhang, S. Hu, P. Liu, A. Li, J. Chen, Optimized CNT-PDMS Flexible Composite for Attachable Health-Care Device, Sensors 20 (2020) 4523. https://doi.org/10.3390/s20164523.

[46] J. Cai, M. Huang, X. Chen, M. Wang, Controllable construction of CROSS-LINKING network for regulating on the mechanical properties of polydimethylsiloxane and

polydimethylsiloxane/carbon nanotubes composites, J. Appl. Polym. Sci. 139 (2022) 52113. https://doi.org/10.1002/app.52113.

[47] H. Xu, L.-X. Gong, X. Wang, L. Zhao, Y.-B. Pei, G. Wang, Y.-J. Liu, L.-B. Wu, J.-X. Jiang, L.-C. Tang, Influence of processing conditions on dispersion, electrical and mechanical properties of graphene-filled-silicone rubber composites, Compos. Part Appl. Sci. Manuf. 91 (2016) 53–64. https://doi.org/10.1016/j.compositesa.2016.09.011.

[48] B. Zhou, W. Luo, J. Yang, X. Duan, Y. Wen, H. Zhou, R. Chen, B. Shan, Thermal conductivity of aligned CNT/polymer composites using mesoscopic simulation, Compos. Part Appl. Sci. Manuf. 90 (2016) 410–416. https://doi.org/10.1016/j.compositesa.2016.07.023.

[49] Y.-T. Li, W.-J. Liu, F.-X. Shen, G.-D. Zhang, L.-X. Gong, L. Zhao, P. Song, J.-F. Gao, L.-C. Tang, Processing, thermal conductivity and flame retardant properties of silicone rubber filled with different geometries of thermally conductive fillers: A comparative study, Compos. Part B Eng. 238 (2022) 109907. https://doi.org/10.1016/j.compositesb.2022.109907.

[50] A. Łapińska, N. Grochowska, J. Antonowicz, P. Michalski, K. Dydek, A. Dużyńska, A. Daniszewska, M. Ojrzyńska, K. Zeranska, M. Zdrojek, Influence of the filler distribution on PDMS-graphene based nanocomposites selected properties, Sci. Rep. 12 (2022) 19038. https://doi.org/10.1038/s41598-022-23735-3.

[51] Y.Y. Huang, S.V. Ahir, E.M. Terentjev, Dispersion rheology of carbon nanotubes in a polymer matrix, Phys. Rev. B 73 (2006) 125422. https://doi.org/10.1103/PhysRevB.73.125422.

[52] S.K. Han, D.M. Shin, H.Y. Park, H.W. Jung, J.C. Hyun, Effect of viscoelasticity on dynamics and stability in roll coatings, Eur. Phys. J. Spec. Top. 166 (2009) 107–110. https://doi.org/10.1140/epjst/e2009-00888-8.

[53] J.H. Lee, J.C. Hyun, Ribbing instability in rigid and deformable forward roll coating flows, (2010).

[54] M.A.L. Manchado, L. Valentini, J. Biagiotti, J.M. Kenny, Thermal and mechanical properties of single-walled carbon nanotubes–polypropylene composites prepared by melt processing, Carbon 43 (2005) 1499–1505. https://doi.org/10.1016/j.carbon.2005.01.031.

[55] C.R. Siviour, J.L. Jordan, High Strain Rate Mechanics of Polymers: A Review, J. Dyn. Behav. Mater. 2 (2016) 15–32. https://doi.org/10.1007/s40870-016-0052-8.

[56] P. Datta, C. Guha, G. Sarkhel, Mechanical, rheological, and electrical properties of multiwalled carbon nanotube reinforced ASA/Na-ionomer blend, J. Appl. Polym. Sci. 132 (2015) app.42516. https://doi.org/10.1002/app.42516.

[57] Y. Chen, Z. Zhao, D. Li, Z. Guo, L. Dong, Constitutive modeling for linear viscoelastic fiber-reinforced composites, Compos. Struct. 263 (2021) 113679. https://doi.org/10.1016/j.compstruct.2021.113679.

[58] A. Hu, X. Li, A. Ajdari, B. Jiang, C. Burkhart, W. Chen, L.C. Brinson, Computational analysis of particle reinforced viscoelastic polymer nanocomposites – statistical study of representative volume element, J. Mech. Phys. Solids 114 (2018) 55–74. https://doi.org/10.1016/j.jmps.2018.02.013.

[59] G. Pan, M. Chen, Y. Wang, J. Zhang, L. Liu, L. Zhang, F. Li, Hyper-Pseudo-Viscoelastic Model and Parameter Identification for Describing Tensile Recovery Stress–Strain

Responses of Rubber Components in TBR, Polymers 15 (2022) 76. https://doi.org/10.3390/polym15010076.

[60] L. Yu, A.L. Skov, Monolithic growth of partly cured polydimethylsiloxane thin film layers, Polym. J. 46 (2014) 123–129. https://doi.org/10.1038/pj.2013.72.

[61] Z. Wang, D.E. Smith, Numerical analysis on viscoelastic creep responses of aligned short fiber reinforced composites, Compos. Struct. 229 (2019) 111394. https://doi.org/10.1016/j.compstruct.2019.111394.

[62] Y. He, X. Lu, D. Wu, M. Zhou, G. He, J. Zhang, L. Zhang, H. Lui, C. Liu, CNT/PDMS conductive foam-based piezoresistive sensors with low detection limits, excellent durability, and multifunctional sensing capability, Sens. Actuators Phys. 358 (2023). https://doi.org/10.1016/j.sna.2023.114408.

[63] T. Payne, S. Mitchell, R. Bibb, M. Waters, Development of novel synthetic muscle tissues for sports impact surrogates, J. Mech. Behav. Biomed. Mater. 41 (2015) 357–374. https://doi.org/10.1016/j.jmbbm.2014.08.011.

[64] T. Payne, S. Mitchell, R. Bibb, M. Waters, The evaluation of new multi-material human soft tissue simulants for sports impact surrogates, J. Mech. Behav. Biomed. Mater. 41 (2015) 336–356. https://doi.org/10.1016/j.jmbbm.2014.09.018.

[65] R. Ansari, M.K. Hassanzadeh Aghdam, Micromechanics-based viscoelastic analysis of carbon nanotube-reinforced composites subjected to uniaxial and biaxial loading, Compos. Part B Eng. 90 (2016) 512–522. https://doi.org/10.1016/j.compositesb.2015.10.048.

[66] S.K. Melly, L. Liu, Y. Liu, J. Leng, A review on material models for isotropic hyperelasticity, Int. J. Mech. Syst. Dyn. 1 (2021) 71–88. https://doi.org/10.1002/msd2.12013.

[67] H. Dal, K. Açıkgöz, Y. Badienia, On the Performance of Isotropic Hyperelastic Constitutive Models for Rubber-Like Materials: A State of the Art Review, Appl. Mech. Rev. 73 (2021) 020802. https://doi.org/10.1115/1.4050978.

[68] H.-D. Nguyen, S.-C. Huang, The Uniaxial Stress–Strain Relationship of Hyperelastic Material Models of Rubber Cracks in the Platens of Papermaking Machines Based on Nonlinear Strain and Stress Measurements with the Finite Element Method, Materials 14 (2021) 7534. https://doi.org/10.3390/ma14247534.

[69] M.O. Tas, M.A. Baker, M.G. Masteghin, J. Bentz, K. Boxshall, V. Stolojan, Highly Stretchable, Directionally Oriented Carbon Nanotube/PDMS Conductive Films with Enhanced Sensitivity as Wearable Strain Sensors, ACS Appl. Mater. Interfaces 11 (2019) 39560–39573. https://doi.org/10.1021/acsami.9b13684.

[70] V.P.W. Shim, L.M. Yang, C.T. Lim, P.H. Law, A visco-hyperelastic constitutive model to characterize both tensile and compressive behavior of rubber, J. Appl. Polym. Sci. 92 (2004) 523–531. https://doi.org/10.1002/app.20029.

[71] J. Bergstrom, Mechanics of Solid Polymers: Theory and Computational Modeling, 1st ed., William Andrew, 2015.

[72] M. Shojaeifard, On finite bending of visco-hyperelastic materials: a novel analytical solution and FEM, Acta Mech. 231 (2020) 3435–3450. https://doi.org/10.1007/s00707-020-02733-4.

[73] M.H.R. Ghoreishy, Determination of the parameters of the Prony series in hyper-viscoelastic material models using the finite element method, Mater. Des. 35 (2012) 791–797. https://doi.org/10.1016/j.matdes.2011.05.057.

[74] M.H.R. Ghoreishy, M. Alimardani, R.Z. Mehrabian, S.T. Gangali, Modeling the hyperviscoelastic behavior of a tire tread compound reinforced by silica and carbon black, J. Appl. Polym. Sci. 128 (2013) 1725–1731. https://doi.org/10.1002/app.38242.

[75] K. Song, N.-K. Cho, K. Park, C.-S. Kim, Investigating Mechanical Behaviours of PDMS Films under Cyclic Loading, Polymers 14 (2022) 2373. https://doi.org/10.3390/polym14122373.

[76] M. Liu, J. Sun, Y. Sun, C. Bock, Q. Chen, Thickness-dependent mechanical properties of polydimethylsiloxane membranes, J. Micromechanics Microengineering 19 (2009) 035028. https://doi.org/10.1088/0960-1317/19/3/035028.

[77] R. Song, H. Schrickx, N. Balar, S. Siddika, N. Sheikh, B.T. O'Connor, Unveiling the Stress–Strain Behavior of Conjugated Polymer Thin Films for Stretchable Device Applications, Macromolecules 53 (2020) 1988–1997. https://doi.org/10.1021/acs.macromol.9b02573.

[78] H. He, J. Liu, Y. Zhang, X. Han, W.V. Mars, L. Zhang, F. Li, Heat Build-Up and Rolling Resistance Analysis of a Solid Tire: Experimental Observation and Numerical Simulation with Thermo-Mechanical Coupling Method, Polymers 14 (2022) 2210. https://doi.org/10.3390/polym14112210.

[79] J.S. Kim, H. Huh, Evaluation of the Material Properties of an OFHC Copper Film at High Strain Rates Using a Micro-Testing Machine, Exp. Mech. 51 (2011) 845–855. https://doi.org/10.1007/s11340-010-9395-6.

[80] E. Ben-David, T. Tepper-Faran, D. Rittel, D. Shilo, A New Methodology for Uniaxial Tensile Testing of Free-Standing Thin Films at High Strain-Rates, Exp. Mech. 54 (2014) 1687–1696. https://doi.org/10.1007/s11340-014-9911-1.

[81] E. Ben-David, T. Tepper-Faran, D. Rittel, D. Shilo, A large strain rate effect in thin free-standing Al films, Scr. Mater. 90–91 (2014) 6–9. https://doi.org/10.1016/j.scriptamat.2014.06.024.

[82] M. Phillips, M. Chen, J. Ryu, M. Zikry, Dynamic Behavior of Ribbed Viscoelastic CNT-PDMS Thin-Films for Multifunctional Applications, Macromol. Mater. Eng. (2024) 2400098. https://doi.org/10.1002/mame.202400098.

[83] M. Phillips, P. Zaghari, J. Eun Ryu, M. Zikry, Microstructural behavior of CNT-PDMS thin-films for multifunctional systems, Compos. Part Appl. Sci. Manuf. 187 (2024) 108473. https://doi.org/10.1016/j.compositesa.2024.108473.

[84] K. Long, J. Brown, A Linear Viscoelastic Model Calibration of Sylgard 184, Sandia Natl. Lab (2017). https://doi.org/10.2172/1365535.

[85] ABAQUS/Standard User's Manual, Version 6.9 Dassault Systemes Similia Corp., (n.d.). https://abaqus-docs.mit.edu/2017/English/SIMACAEEXCRefMap/simaexc-c-docproc.htm (accessed January 12, 2023).

[86] R.W. Mailen, Y. Liu, M.D. Dickey, M. Zikry, J. Genzer, Modelling of shape memory polymer sheets that self-fold in response to localized heating, Soft Matter 11 (2015) 7827–7834. https://doi.org/10.1039/C5SM01681A.

[87] D.B. Adolf, R.S. Chambers, M.A. Neidigk, A simplified potential energy clock model for glassy polymers, Polymer 50 (2009) 4257–4269. https://doi.org/10.1016/j.polymer.2009.06.068.

[88] M.L. Williams, R.F. Landel, J.D. Ferry, The Temperature Dependence of Relaxation Mechanisms in Amorphous Polymers and Other Glass-forming Liquids, J. Am. Chem. Soc. 77 (1955) 3701–3707. https://doi.org/10.1021/ja01619a008.

[89] M.F. Arif, S. Kumar, T.K. Gupta, K.M. Varadarajan, Strong linear-piezoresistive-response of carbon nanostructures reinforced hyperelastic polymer nanocomposites, Compos. Part Appl. Sci. Manuf. 113 (2018) 141–149. https://doi.org/10.1016/j.compositesa.2018.07.021.

[90] O.H. Yeoh, Characterization of Elastic Properties of Carbon-Black-Filled Rubber Vulcanizates, Rubber Chem. Technol. 63 (1990) 792–805.

[91] N.M. Newmark, A Method of Computation for Structural Dynamics, J. Eng. Mech. Div. EM3 (1959) 67–94.

[92] H.M. Hilber, T.J.R. Hughes, R.L. Taylor, Improved numerical dissipation for time integration algorithms in structural dynamics, Earthq. Eng. Struct. Dyn. 5 (1977) 283–292. https://doi.org/10.1002/eqe.4290050306.

[93] Y. Ebata, A.B. Croll, A.J. Crosby, Wrinkling and strain localizations in polymer thin films, Soft Matter 8 (2012) 9086. https://doi.org/10.1039/c2sm25859e.

[94] M.D. Morris, Factorial Sampling Plans for Preliminary Computational Experiments, 33 (2023).

[95] M.A. Bhuiyan, R.V. Pucha, J. Worthy, M. Karevan, K. Kalaitzidou, Understanding the effect of CNT characteristics on the tensile modulus of CNT reinforced polypropylene using finite element analysis, Comput. Mater. Sci. 79 (2013) 368–376. https://doi.org/10.1016/j.commatsci.2013.06.046.

[96] S. Marceau, P. Dubois, R. Fulchiron, P. Cassagnau, Viscoelasticity of Brownian Carbon Nanotubes in PDMS Semidilute Regime, Macromolecules 42 (2009) 1433–1438. https://doi.org/10.1021/ma802628q.

[97] S. Yang, S. Yu, W. Kyoung, D.-S. Han, M. Cho, Multiscale modeling of size-dependent elastic properties of carbon nanotube/polymer nanocomposites with interfacial imperfections, Polymer 53 (2012) 623–633. https://doi.org/10.1016/j.polymer.2011.11.052.

[98] S. Yang, S. Yu, J. Ryu, J.-M. Cho, W. Kyoung, D.-S. Han, M. Cho, Nonlinear multiscale modeling approach to characterize elastoplastic behavior of CNT/polymer nanocomposites considering the interphase and interfacial imperfection, Int. J. Plast. 41 (2013) 124–146. https://doi.org/10.1016/j.ijplas.2012.09.010.

[99] Z. Liu, J.A. Moore, S.M. Aldousari, H.S. Hedia, S.A. Asiri, W.K. Liu, A statistical descriptor based volume-integral micromechanics model of heterogeneous material with arbitrary inclusion shape, Comput. Mech. 55 (2015) 963–981. https://doi.org/10.1007/s00466-015-1145-2.

[100] U.D. Çakmak, F. Hiptmair, Z. Major, Applicability of elastomer time-dependent behavior in dynamic mechanical damping systems, Mech. Time-Depend. Mater. 18 (2014) 139–151. https://doi.org/10.1007/s11043-013-9219-z.

[101] T. Miyata, K. Tokumaru, F. Tsumori, Combining multi-step imprinting with the in-plane compression method, Jpn. J. Appl. Phys. 59 (2020) SIIJ07. https://doi.org/10.35848/1347-4065/ab79ef.

[102] M.F. Oskouie, R. Ansari, H. Rouhi, Studying nonlinear thermomechanical wave propagation in a viscoelastic layer based upon the Lord-Shulman theory, Mech. Adv. Mater. Struct. 27 (2020) 800–806. https://doi.org/10.1080/15376494.2018.1495793.

[103] H.G. Salem, W.M. Lee, L. Bodelot, G. Ravichandran, M.A. Zikry, Quasi-Static and High-Strain-Rate Experimental Microstructural Investigation of a High-Strength Aluminum

Alloy, Metall. Mater. Trans. A 43 (2012) 1895–1901. https://doi.org/10.1007/s11661-011-1064-6.

[104] M.H. Gahruei, H. Golestanian, Evaluation of effective mechanical properties of nanocomposites reinforced with multiwalled carbon nanotube, Mater. Sci. Technol. 29 (2013) 1484–1491. https://doi.org/10.1179/1743284713Y.0000000312.

[105] R. Razavi, Y. Zare, K.Y. Rhee, A model for tensile strength of polymer/carbon nanotubes nanocomposites assuming the percolation of interphase regions, Colloids Surf. Physicochem. Eng. Asp. 538 (2018) 148–154. https://doi.org/10.1016/j.colsurfa.2017.10.063.

[106] Ł. Figiel, Effect of the interphase on large deformation behaviour of polymer–clay nanocomposites near the glass transition: 2D RVE computational modelling, Comput. Mater. Sci. 84 (2014) 244–254. https://doi.org/10.1016/j.commatsci.2013.12.012.

[107] M. Motamedi, M. Eskandari, M. Yeganeh, Effect of straight and wavy carbon nanotube on the reinforcement modulus in nonlinear elastic matrix nanocomposites, Mater. Des. 34 (2012) 603–608. https://doi.org/10.1016/j.matdes.2011.05.013.

[108] Y. He, D. Wu, M. Zhou, Y. Zheng, T. Wang, C. Lu, L. Zhang, H. Liu, C. Liu, Wearable Strain Sensors Based on a Porous Polydimethylsiloxane Hybrid with Carbon Nanotubes and Graphene, ACS Appl. Mater. Interfaces 13 (2021) 15572–15583. https://doi.org/10.1021/acsami.0c22823.

[109] H.-D. Nguyen-Tran, V.-T. Hoang, V.-T. Do, D.-M. Chun, Y.-J. Yum, Effect of Multiwalled Carbon Nanotubes on the Mechanical Properties of Carbon Fiber-Reinforced Polyamide-6/Polypropylene Composites for Lightweight Automotive Parts, Materials 11 (2018) 429. https://doi.org/10.3390/ma11030429.

[110] K. Long, J. Brown, A Linear Viscoelastic Model Calibration of Sylgard 184., 2017. https://doi.org/10.2172/1365535.

[111] J. Paul, S. Sindhu, M.H. Nurmawati, S. Valiyaveettil, Mechanics of prestressed polydimethylsiloxane-carbon nanotube composite, Appl. Phys. Lett. 89 (2006) 184101. https://doi.org/10.1063/1.2372447.